NASA/TP—2018–219692

Curvilinear Displacement Transfer Functions for Deformed Shape Predictions of Curved Structures Using Distributed Surface Strains

William L. Ko, and Van Tran Fleischer
Armstrong Flight Research Center, Edwards, California

Shun-Fat Lung
Jacob's Technology, Inc., Edwards, California

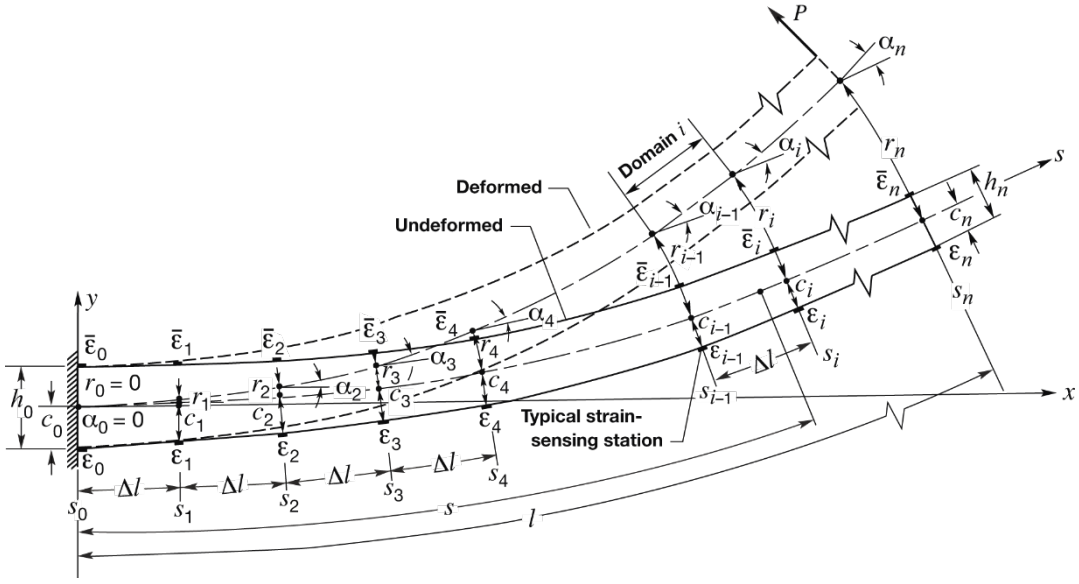

TECHNOLOGY PROTECTION NOTICE

NASA is currently seeking patent protection on the methods described in this NASA technical publication. Therefore, those interested in using the methods should contact the NASA Technology Transfer Office, NASA Armstrong Flight Research Center, Edwards, California for more information.

September 2018

NASA STI Program ... in Profile

Since its founding, NASA has been dedicated to the advancement of aeronautics and space science. The NASA scientific and technical information (STI) program plays a key part in helping NASA maintain this important role.

The NASA STI program operates under the auspices of the Agency Chief Information Officer. It collects, organizes, provides for archiving, and disseminates NASA's STI. The NASA STI program provides access to the NTRS Registered and its public interface, the NASA Technical Reports Server, thus providing one of the largest collections of aeronautical and space science STI in the world. Results are published in both non-NASA channels and by NASA in the NASA STI Report Series, which includes the following report types:

- TECHNICAL PUBLICATION. Reports of completed research or a major significant phase of research that present the results of NASA Programs and include extensive data or theoretical analysis. Includes compilations of significant scientific and technical data and information deemed to be of continuing reference value. NASA counter-part of peer-reviewed formal professional papers but has less stringent limitations on manuscript length and extent of graphic presentations.

- TECHNICAL MEMORANDUM. Scientific and technical findings that are preliminary or of specialized interest, e.g., quick release reports, working papers, and bibliographies that contain minimal annotation. Does not contain extensive analysis.

- CONTRACTOR REPORT. Scientific and technical findings by NASA-sponsored contractors and grantees.

- CONFERENCE PUBLICATION. Collected papers from scientific and technical conferences, symposia, seminars, or other meetings sponsored or co-sponsored by NASA.

- SPECIAL PUBLICATION. Scientific, technical, or historical information from NASA programs, projects, and missions, often concerned with subjects having substantial public interest.

- TECHNICAL TRANSLATION. English-language translations of foreign scientific and technical material pertinent to NASA's mission.

Specialized services also include organizing and publishing research results, distributing specialized research announcements and feeds, providing information desk and personal search support, and enabling data exchange services.

For more information about the NASA STI program, see the following:

- Access the NASA STI program home page at http://www.sti.nasa.gov

- E-mail your question to help@sti.nasa.gov

- Phone the NASA STI Information Desk at 757-864-9658

- Write to:
  NASA STI Information Desk
  Mail Stop 148
  NASA Langley Research Center
  Hampton, VA 23681-2199

NASA/TP—2018–219692

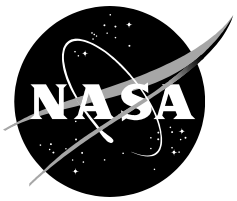

Curvilinear Displacement Transfer Functions for Deformed Shape Predictions of Curved Structures Using Distributed Surface Strains

William L. Ko, and Van Tran Fleischer
Armstrong Flight Research Center, Edwards, California

Shun-Fat Lung
Jacob's Technology, Inc., Edwards, California

National Aeronautics and
Space Administration

Armstrong Flight Research Center
Edwards, California 93523-0273

September 2018

Table of Contents

Abstract

Curvilinear Displacement Transfer Functions were formulated for deformed shape predictions of different curved structures using surface strains. The embedded curved beam (depth-wise cross section of a curved structure along a surface strain-sensing line) was discretized into multiple small domains, with domain junctures matching the strain-sensing stations. Thus, the surface strain distribution can be described with a piecewise linear or a piecewise nonlinear function. The discrete approach enabled piecewise integrations of a curvature-strain differential equation for the embedded curved beam to yield closed-form Curvilinear Displacement Transfer Functions, which are written in terms of embedded curved-beam geometrical parameters and surface strains. By inputting the surface strain data, the Curvilinear Displacement Transfer Functions can transform surface strains into deflections along each embedded curved beam for mapping out the overall structural deformed shapes. The finite-element method was used to analytically generate the surface strains of the curved beams. The deformed shape prediction accuracies were then determined by comparing the theoretical deflections with the finite-element-generated deflections, which were used as yardsticks. By introducing the correction factors in simple mathematical forms, the Curvilinear Displacement Transfer Functions can be quite accurate for shape predictions of different curved-beam structures ranging from limit case of straight beam up to semicircular curved beam.

Nomenclature

$a(s)$	curvilinear displacement (measured from the x-axis) of a bent cantilever straight beam in forming an undeformed cantilever curved beam, in.
AB	incremental arc length
$A'B'$	deformed arc length of AB
$c(s)$	depth factor at axial location s (distance from neutral axis to the outer surface of the embedded curved beam), in.
c_i	$\equiv c(s_i)$, depth factor at $s = s_i$ [associated with outer surface bending strain $\varepsilon(s_i)$], in.
c_0	value of c_i at embedded curved-beam root $(s = s_0 = 0)$, in.
c_n	value of c_i at embedded curved-beam tip $(s = s_n = l)$, in.
c	$\equiv (c_{i-1} + c_i)/2$, averaged depth factor for a small domain $s_{i-1} \le s \le s_i$, in.
c_c	centroid-axis depth factor (distance from centroid axis to the outer surface), in.
d_i	$\equiv \sqrt{u_i^2 + v_i^2}$, linear distance between undeformed and deformed positions of a point at $s = s_i$, in.
dr	differential of r, in.
ds	differential of s, in.
$d\theta$	differential of θ, rad
E	Young's modulus, lb/in^2
h	$= (h_{i-1} + h_i)/2$, averaged depth of embedded curved beam within domain $s_{i-1} \le s \le s_i$, in.
h_i	depth of an embedded curved beam at $s = s_i$, in.
h_{i-1}	depth of an embedded curved beam at $s = s_{i-1}$, in.
h_0	depth of an embedded curved beam at fixed end $(s = s_0 = 0)$, in.
h_n	depth of an embedded curved beam at free end $(s = s_n = l)$, in.
i	$= 0,1,2,3,...,n,$ strain-sensing station identification number
j	dummy index

k_{in} $\equiv \sigma_{in}/\sigma$, magnitude of normalized bending stress on concave side of curved beam, no dimension

k_{out} $\equiv \sigma_{out}/\sigma$, magnitude of normalized bending stress on the convex side of a curved beam, no dimension

l curvilinear length of an embedded curved beam, in.

L_i $= 2R_0 \sin\left[(i/n)(\phi_n/2)\right]$, distance from origin to point $s = s_i$, the chord length subtended by angle $(i/n)\phi_n$ with radius R_0, in.

n identification number for the last span-wise strain-sensing station, or domain density (number of domains between two adjacent strain-sensing stations)

P applied load, lb

$r(s)$ local curved deflection (curvilinear distance traced by a material point from its initial undeformed position to its final deformed position), in.

r_i $\equiv r(s_i)$, curved deflection at $s = s_i$, in.

$\widehat{r}_i$ corrected deflection

r_i^B deflection of the two-end supported curved beam at $s = s_i$, in.

$r_i^{(N)}$ Nastran-generated curved (or radial) deflection at $s = s_i$, in.

R $= R(s)$, local radius of curvature of a deformed embedded curved beam, in.

R_0 radius of curvature of undeformed embedded curved beam, in.

s curvilinear axial coordinate along the neutral axis of an embedded curved beam, in.

s_i curvilinear axial coordinate of *i*-th strain-sensing station at $s = s_i$, in.

u_i *x*-displacement at $s = s_i$, in.

v_i y-displacement at $s = s_i$, in.

w width, in.

x, y Cartesian coordinates, in.

$\widehat{y}(s)$ curved deflection measured from *x*-axis, in.

$\widehat{y}_i$ $\equiv \widehat{y}(s_i)$, curved deflection at $s = s_i$, in.

α deformed slope angle, rad

$\alpha(s)$ $\equiv \theta - \theta_0$, deformed slope angle relative to the undeformed slope angle θ_0, rad

α_i $\equiv \alpha(s_i)$, deformed slope angle at $s = s_i$, rad

β_i angle subtended by d_i (considered as chord length), rad

δ neutral axis offset, in.

$\delta\phi_i$ angular displacement of the *i*-th strain-sensing station at $s = s_i$, rad

Δl $\equiv (s_i - s_{i-1}) = l/n$, domain length (strain-sensing stations separation curvilinear distance), in

$\varepsilon(s)$ outer surface bending strain at the curvilinear axial location *s*, in/in

ε_i $\equiv \varepsilon(s_i)$, outer surface bending strain at $s = s_i$, in/in

$\overline{\varepsilon}_i$ $\equiv \overline{\varepsilon}(s_i)$, inner surface bending strain at $s = s_i$, in/in

η_i $\equiv \sqrt{\dfrac{2\sin(\phi_i/2)}{\phi_i}}$, correction factor at $s = s_i$ for cantilever curved beams, no dimension

η_n beam tip correction factor

$\hat{\eta}_{n/2}$ $\equiv \sqrt{\frac{\phi_{n/2}}{\sin\phi_{n/2}}}$, correction factor at beam center $(i = n/2)$ for two-end supported curved beams, no dimension

θ slope angle of a deformed embedded curved beam in reference to the *x*-axis, rad

θ_0 slope angle of an undeformed embedded curved beam in reference to the *x*-axis, rad

$(\theta_0)_i$ value of θ_0 at $s = s_i$, rad

ν Poisson's Ratio

σ magnitude of surface bending stress of an equivalent straight beam, lb/in^2

σ_{in} magnitude of bending stress on the concave side of a curved beam, lb/in^2

σ_{out} magnitude of bending stress on the convex side of a curved beam, lb/in^2

ϕ_n curved-beam angle, rad or deg

ϕ_i $= (i/n)\phi_n$, angular location of *i*-th strain-sensing station at $s = s_i$, rad or deg

Introduction

Deflections of a structure under load can be experimentally measured using position transducers or photogrammetry. However, these methods can be impractical for airborne structures. Traditionally, deflections of the loaded structure can be analytically calculated by using the finite-element method. However, depending on the structures, finite-element modeling can be quite complex and very time consuming. To eliminate the need for tedious finite-element modeling, the Displacement Transfer Functions (refs. 1–9) were invented to transform measured surface strains into out-of-plane deflections so that one can map out the overall structural deformed shapes for visual displays. Keep in mind that without using the Displacement Transfer Functions, strain sensors of any type cannot sense the overall structural deformed shapes. This innovative patented technology for structure deformed shape predictions is called, "Method for Real-Time Structure Shape-Sensing," U.S. Patent Number 7,520,176, (ref. 2), which is very attractive for application to in-flight deformed shape monitoring of flexible wings and tails, such as those often employed on flight vehicles for maintaining safe flights. In addition, the real-time wing shape monitored could then be input to the aircraft control system for aero-elastic wing shape control.

In the formulation of the past Displacement Transfer Functions (refs. 1–9), strain-sensing stations (strain measurement points) are to be discretely distributed along a strain-sensing line on the surface of the structure (for example, an aircraft wing). The depth-wise cross section of the structure along the strain-sensing line is called an embedded beam (not to be confused with the classical isolated Euler-Bernoulli beam). Each embedded beam was then evenly discretized into multiple domains with domain junctures matching the strain-sensing stations. By discretization, variation of the surface strain can be described with either a piecewise linear or a piecewise nonlinear function. The piecewise approach enabled piecewise integrations of the curvature-strain differential equation for the deformed embedded beam to yield slope and deflection equations in recursive forms. Those recursive slope and deflection equations can then be combined into a single deflection equation in summation form. Those three equations are then called Displacement Transfer Functions, which are expressed in terms of the embedded beam geometrical parameters and surface strains, containing no material properties. By entering the surface strain data into the Displacement Transfer Functions, one can then calculate slopes and deflections along the deformed embedded beam. By using multiple strain-sensing lines, overall deformed shapes of a structure subjected to bending and torsion loadings can then be graphically mapped out for visual display. A total of seven sets of Displacement Transfer Functions were formulated in the past for applications to different types of structural geometries (refs. 1–9).

All the earlier Displacement Transfer Functions (refs. 1–9) were analytically validated for the prediction accuracies using finite-element analysis of various slender structures under combined bending and torsion. Those structures include: tapered cantilever tubular beams, tapered two-end supported tubular

beams, depth-tapered wing boxes (unswept and swept), a width-tapered wing box, a doubly-tapered wing box, plates, doubly tapered Ikhana wings (66-ft wingspan) (fig. 1a) (ref. 10), and GIII swept wings (77.83-ft wingspan) (fig. 1b) (ref. 11). Also, the accuracy of a typical Displacement Transfer Function was experimentally validated by large-scale ground tests of highly flexible Global Observer wings (175-ft wingspan, wingtip deflections could reach up to 32 ft during flights) (ref. 12).

The rectilinearly distributed surface strains can also be entered into the Stiffness, Load Transfer Functions, and the Displacement Transfer Functions, to calculate structural stiffness (bending and torsion) and inflight loads (bending moments, shear loads, and torques) for monitoring the inflight loads of the flight vehicle. This patented method is called, "Process for Using Surface Strain Measurements to Obtain Operational Loads for Complex Structures," U.S. Patent No. 7,715,994, (ref. 13). The accuracy of this patented method for estimating operational loads on structures was analytically validated by using finite-element analysis of different aerospace structures (tapered cantilever tubular beams, depth tapered un-swept wing boxes, depth tapered swept wing boxes, and doubly-tapered Ikhana wing) (ref. 14).

The earlier Displacement Transfer Functions (refs. 1–9) were formulated exclusively for straight embedded beams, and when applied to the shape predictions of curved structures, one had to introduce empirically determined curvature correction factors (refs. 5, 9). Thus, there is a need to mathematically formulate Curvilinear Displacement Transfer Functions for the deformed shape predictions of curved structures (for example, rocket motor and aircraft fuselage cross sections).

In the present paper, Curvilinear Displacement Transfer Functions are formulated for shape predictions of curved structures with different initial curvatures. A family of long curved beams (cantilever and two-end supported) were chosen to study the shape-prediction accuracies of the Curvilinear Displacement Transfer Functions. Instead of using actually measured surface strains, finite-element analyses of the curved beams were carried out to analytically generate the surface strains. The associated finite-element-generated deflections were used as yardsticks in the shape prediction accuracy analysis. The Curvilinear Displacement Transfer Functions were then used to calculate the theoretical deflections using the finite-element-generated surface strains as inputs. The shape prediction accuracies were then determined by comparing the theoretical deflections with the finite-element-generated deflections (yardsticks). The results show that, with the use of correction factors of simple mathematical forms, the Curvilinear Displacement Transfer Functions are very accurate for shape predictions of different curved structures, ranging from the limit case of a straight beam up to a semicircular (180-deg arc) curved beam.

Curvature-Strain Relationship

Figure 2 shows the embedded curved beam with an initial constant radius of curvature R_0 and depth factor c. The embedded beam is defined as the depth-wise cross section of a structure along a strain-sensing line. After inward bending, a small curved segment $AB = (R_0 + c)d\theta_0$ on the outer surface of the undeformed curve beam subtended by a small angle $d\theta_0$ will deform into a new arc length $A'B' = (R + c)d\theta$, where $R[\equiv R(s)]$ is the local radius of curvature of the deformed arc length $A'B'$ subtended by a deformed small angle $d\theta$ (fig. 2). Then, the outer surface strain $\varepsilon(s)$ in reference to the curved s-system (fig. 1), can be expressed with equation (1) as:

$$\varepsilon(s) = \frac{A'B' - AB}{AB} = \frac{(R + c)d\theta - (R_0 + c)d\theta_0}{(R_0 + c)d\theta_0} \tag{1}$$

For an in-extensional (no length changed in neutral axis) embedded curved beam, the small curved segments ds along the neutral axis remains unchanged after deformation and, therefore, in view of figure 2, one can write equation (2):

$$ds = R_0 d\theta_0 = R d\theta \tag{2}$$

From equation (2), the deformed small angle $d\theta$ can be related to the undeformed small angle $d\theta_0$ through equation (3) as:

$$d\theta = \frac{R_0}{R} d\theta_0 \tag{3}$$

Substitution of equation (3) into equation (1) yields equation (4):

$$\begin{aligned} \varepsilon(s) &= \frac{(R+c)(R_0/R)d\theta_0 - (R_0+c)d\theta_0}{(R_0+c)d\theta_0} = \frac{(R+c)R_0 - R(R_0+c)}{R(R_0+c)} \\ &= \frac{c(R_0-R)}{R(R_0+c)} = \frac{c}{R_0+c}\left(\frac{R_0}{R}-1\right) = \frac{c}{1+c/R_0}\left(\frac{1}{R}-\frac{1}{R_0}\right) \end{aligned} \tag{4}$$

Equation (4) can be rewritten in the alternative form as equation (5), which relates the curvature differential $(1/R - 1/R_0)$ to surface strain $\varepsilon(s)$:

$$\frac{1}{R} - \frac{1}{R_0} = \left[1 + \frac{c(s)}{R_0}\right]\frac{\varepsilon(s)}{c(s)} \tag{5}$$

In view of equation (2), the left-hand side of equation (5) can be written in terms of small angles $\{d\theta_0, d\theta\}$ as equation (6):

$$\frac{1}{R} - \frac{1}{R_0} = \frac{d\theta}{ds} - \frac{d\theta_0}{ds} = \frac{d\theta - d\theta_0}{ds} = \frac{d(\theta - \theta_0)}{ds} = \frac{d\alpha}{ds} \tag{6}$$

In equation (6), $\alpha(\equiv \theta - \theta_0)$ is the deformed slope angle in reference to the undeformed slope angle θ_0. Substitution of equations (6) into equation (5) yields the following equation (7), relating the slope-angle gradient $d\alpha/ds$ to surface strain $\varepsilon(s)$ for the embedded curved beam:

$$\frac{d\alpha}{ds} = \left[1 + \frac{c(s)}{R_0}\right]\frac{\varepsilon(s)}{c(s)} \tag{7}$$

The Curvilinear Displacement Transfer Functions are to be formulated through integrations of equation (7) (called α-formulation) as described in the subsequent sections.

Theoretical Formulations

The Curvilinear Displacement Transfer Functions can be formulated by integrating curvature-strain differential equation (7). For the given embedded curved beam, the initial radius of curvature R_0 is

known. However, for the curved beams, the neutral axis and centroid axis may not coincide, and the neutral-axis depth factor $c(s)$ can be calculated by using outer and inner surface strains (described in the Neutral-Axis Shifting Method section). Also, the functional form of surface strain $\varepsilon(s)$ must be established before equation (7) can be integrated. By introducing a discretization method described in the following section, variation of $\varepsilon(s)$ can be represented with a piecewise linear or a piecewise nonlinear function so that piecewise integration of equation (7) can be carried out.

Discretization

Figure 3 shows a typical cantilever embedded curved beam with curved length *l* and depth factor $c(s)$, installed with outer and inner surface strain-sensing lines. The embedded curved beam is then evenly discretized into *n* small domains (domain length $\Delta l = l/n$), with domain junctures matching the strain-sensing stations. Thus, there are $(n+1)$ equally spaced strain-sensing stations at $s = s_i$ $(i = 0,1,2,3,...,n)$ along the strain-sensing lines for obtaining the outer and inner surface bending strains, $\{\varepsilon_i, \bar{\varepsilon}_i\}$. Note that the first and the last strain-sensing stations $\{s_0, s_n\}$ are located respectively at the fixed end $(s_0 = 0)$ and free end $(s_n = l)$.

Using the discretization approach (fig. 3), surface strain distributions can be represented with a piecewise linear or a nonlinear function. Then, equation (7) can be piecewise integrated to yield slope and deflection equations derived in the following sections.

Piecewise Strain Representations

If the surface strain $\varepsilon(s)$ varies slowly in the s-direction within a small domain $(s_{i-1} \le s \le s_i)$ between two-adjacent strain-sensing stations $\{s_{i-1}, s_i\}$, then the value of $\varepsilon(s)$ can be represented with a linear function [eq. (8)] or nonlinear (quadratic) function [eqs. (9)]:

Linear Representation

$$\varepsilon(s) = \varepsilon_{i-1} - (\varepsilon_{i-1} - \varepsilon_i)\frac{s - s_{i-1}}{\Delta l} \quad ; \quad (s_{i-1} \le s \le s_i)\ (i = 1,2,3,...,n) \tag{8}$$

In equation (8), $\{\varepsilon_{i-1}, \varepsilon_i\}$ are respectively the values of $\varepsilon(s)$ at the strain-sensing stations $\{s_{i-1}, s_i\}$.

Nonlinear Representation

$$\varepsilon(s) = \varepsilon_{i-1} - \frac{3\varepsilon_{i-1} - 4\varepsilon_i + \varepsilon_{i+1}}{2\Delta l}(s - s_{i-1}) + \frac{\varepsilon_{i-1} - 2\varepsilon_i + \varepsilon_{i+1}}{2(\Delta l)^2}(s - s_{i-1})^2 \tag{9a}$$

$$(s_{i-1} \le s \le s_i)\ (i = 1,2,3,...,n)$$

$$\varepsilon_{n+1} = \varepsilon_{n-2} - 3\varepsilon_{n-1} + 3\varepsilon_n \quad ; \quad (i = n) \tag{9b}$$

In equation (9a), when $i = n$, the non-existing strain ε_{n+1} will appear. Therefore, the three point extrapolation equation (9b) is provided for estimating the non-existing strain ε_{n+1}. Keep in mind that equations (8) and (9) are also applicable to the inner surface strain $\overline{\varepsilon}(s)$ case.

Stepwise Depth Factor Representation

If the depth factor $c(s)$ varies very slowly with s within a small domain $s_{i-1} \le s \le s_i$, between two adjacent strain-sensing stations $\{s_{i-1}, s_i\}$, then the variation of $c(s)$ is very small and can be approximated with the averaged depth factor c defined as equation (10):

$$c(s) \approx c \equiv \frac{1}{2}(c_{i-1} + c_i) \quad ; \quad (i = 1,2,3,...,n) \tag{10}$$

In equation (10), $\{c_{i-1}, c_i\}$ are respectively the depth factors at the strain-sensing stations $\{s_{i-1}, s_i\}$ (fig. 2). Using equation (10) will greatly simplify mathematical processes in the piecewise integrations of equation (7) to obtain both slope and deflection equations.

Basic Slope-Angle Equation

The slope-angle equation can be obtained by piecewise integration of equation (7) within each small domain $s_{i-1} \le s \le s_i$ as equation (11):

$$\int_{s_{i-1}}^{s} \frac{d\alpha}{ds} ds = \int_{s_{i-1}}^{s} \left[1 + \frac{c(s)}{R_0}\right] \frac{\varepsilon(s)}{c(s)} ds \quad ; \quad (s_{i-1} \le s \le s_i) \tag{11}$$

In equation (11), if the depth factor $c(s)$ is represented with the averaged value c according to equation (10), then the factor $[1 + c(s)]/R_0)[1/c(s)]$ can be replaced with $(1 + c/R_0)(1/c)$ and can be moved outside the integral sign, and thereby simplifying the integration process. After integration of the left-hand side, equation (11) can be written as equation (12):

$$\alpha(s) = \underbrace{\left(1 + \frac{c}{R_0}\right)\frac{1}{c}\int_{s_{i-1}}^{s} \varepsilon(s) ds}_{\text{Slope-angle increment due to } \varepsilon(s)} + \underbrace{\alpha_{i-1}}_{\substack{\text{Slope angle} \\ \text{at } s_{i-1}}} \quad ; \quad (s_{i-1} \le s \le s_i) \tag{12}$$

In equation (12), $\alpha_{i-1}[\equiv \alpha(s_{i-1})]$ is the slope angle at strain-sensing station s_{i-1}.

Basic Deflection Equation

If $r(s)$ denotes the curved deflection at point s (fig. 4), measured from the undeformed curved embedded beam (that is, curvilinear distance traced by a material point at point s from its initial undeformed position to its final deformed position), then the curved deflection increment dr due to incremental ds can be related to the slope angle $\alpha(s)$ as $\alpha(s) = dr/ds$ (fig. 4). Thus, one can integrate the slope-angle equation (12) within the small domain $s_{i-1} \le s \le s_i$ as equation (13):

$$\int_{s_{i-1}}^{s}\alpha(s)ds=\int_{s_{i-1}}^{s}\underbrace{\frac{dr}{ds}}_{\alpha(s)}ds=\int_{s_{i-1}}^{s}\underbrace{\left[\left(1+\frac{c}{R_0}\right)\frac{1}{c}\int_{s_{i-1}}^{s}\varepsilon(s)ds+\alpha_{i-1}\right]}_{\text{Right-hand side of eq. (12)}}ds \quad ; \quad (s_{i-1}\le s\le s_i) \tag{13}$$

After partial integration of equation (13) and rearranging, one obtains the curved deflection equation (14) of the following form:

$$r(s)=\underbrace{\left(1+\frac{c}{R_0}\right)\frac{1}{c}\int_{s_{i-1}}^{s}\int_{s_{i-1}}^{s}\varepsilon(s)ds\,ds}_{\text{Deflection increment due to }\varepsilon(s)}+\underbrace{r_{i-1}}_{\substack{\text{Deflection}\\ \text{at } s_{i-1}}}+\underbrace{(s-s_{i-1})\alpha_{i-1}}_{\substack{\text{Deflection}\\ \text{due to } \alpha_{i-1}}} \quad ; \quad (s_{i-1}\le s\le s_i) \tag{14}$$

In equation (14), the term $r_{i-1}[\equiv r(s_{i-1})]$ is the curved deflection at strain-sensing station s_{i-1}.

List of Curvilinear Displacement Transfer Functions

By using piecewise representations of the surface strains given by equations (8) or (9), the slope-angle equation (12) and the deflection equation (14) can be piecewise integrated (ref. 15) to yield the following final forms given by equations (15) and (16) (see derivations in Appendices A–D).

Piecewise Linear Strain Case

Slope-angle equation in recursive form (Appendix A) is shown as equation (15a):

$$\alpha_i=\left(1+\frac{c}{R_0}\right)\frac{\Delta l}{2c}\left(\varepsilon_{i-1}+\varepsilon_i\right)+\alpha_{i-1} \quad ; \quad (i=1,2,3,...,n) \tag{15a}$$

Deflection equation in recursive form (Appendix A) is shown in equation (15b):

$$r_i=\left(1+\frac{c}{R_0}\right)\frac{(\Delta l)^2}{6c}\left(2\varepsilon_{i-1}+\varepsilon_i\right)+r_{i-1}+(\Delta l)\alpha_{i-1} \quad ; \quad (i=1,2,3,...,n) \tag{15b}$$

Deflection equation in summation form (Appendix B) is shown in equation (15c):

$$r_i=\underbrace{\left(1+\frac{c}{R_0}\right)\frac{(\Delta l)^2}{6c}\sum_{j=1}^{i}(2\varepsilon_{j-1}+\varepsilon_j)}_{\text{Contributions from deflection terms}}+\underbrace{\left(1+\frac{c}{R_0}\right)\frac{(\Delta l)^2}{2c}\sum_{j=1}^{i-1}(i-j)(\varepsilon_{j-1}+\varepsilon_j)}_{\text{Contributions from slope terms}}+\underbrace{r_0+(i)(\Delta l)\alpha_0}_{=0 \text{ for cantilever beams}} \tag{15c}$$

$$(i=1,2,3,...,n)$$

Equations (15a–15c) are called the Curvilinear Displacement Transfer Functions for embedded curved beams.

Piecewise Nonlinear Strain Case

Slope-angle equation in recursive form (Appendix C) is shown in equation (16a):

$$\alpha_i = \left(1 + \frac{c}{R_0}\right)\frac{\Delta l}{12c}(5\varepsilon_{i-1} + 8\varepsilon_i - \varepsilon_{i+1}) + \alpha_{i-1} \quad ; \quad (i = 1,2,3,...,n) \tag{16a}$$

Deflection equation in recursive form (Appendix C) is shown in equation (16b):

$$r_i = \left(1 + \frac{c}{R_0}\right)\frac{(\Delta l)^2}{24c}(7\varepsilon_{i-1} + 6\varepsilon_i - \varepsilon_{i+1}) + r_{i-1} + (\Delta l)\alpha_{i-1} \quad ; \quad (i = 1,2,3,...,n) \tag{16b}$$

Deflection equation in dual summation form (Appendix D) is shown in equation (16c):

$$r_i = \underbrace{\left(1 + \frac{c}{R_0}\right)\frac{(\Delta l)^2}{24c}\sum_{j=1}^{i}(7\varepsilon_{j-1} + 6\varepsilon_j - \varepsilon_{j+1})}_{\text{Contributions from deflection terms}} + \underbrace{\left(1 + \frac{c}{R_0}\right)\frac{(\Delta l)^2}{12c}\sum_{j=1}^{i-1}(i-j)(5\varepsilon_{j-1} + 8\varepsilon_j - \varepsilon_{j+1})}_{\text{Contributions from slope terms}} + \underbrace{r_0 + (i)(\Delta l)\alpha_0}_{=0 \text{ for cantilever beams}} \tag{16c}$$

Equations (16a–16c) are called the Improved Curvilinear Displacement Transfer Functions for embedded curved beams.

Two-End Supported Embedded Curved Beams

The Curvilinear Displacement Transfer Functions (15) and (16) formulated for cantilever embedded curved beams $(\alpha_0 = r_0 = 0)$ can be used to calculate deflections $r_i^B (i = 0,1,2,3,...,n)$ of the two-end supported (fixed or simply supported) embedded curved beams (fig. 5). By enforcing zero deflection $(r_n^B = 0)$ at the right support point ($i = n$), the deflection r_i^B of the two-end supported embedded curved beams can be expressed as equation (17) (refs. 1, 2):

$$r_i^B \approx r_i - \frac{s_i}{l}r_n = r_i - \frac{i(\Delta l)}{n(\Delta l)}r_n = r_i - \frac{i}{n}r_n \quad ; \quad (i = 0,1,2,3,...,n) \tag{17}$$

In equation (17), r_i is the curved deflection of the cantilever embedded curved beam at s_i, and can be calculated from equations (15) [or equation (16)] by setting $\alpha_0 = r_0 = 0$. Equation (17) is called Curvilinear Displacement Transfer Function for two-end supported embedded curved beams.

Figure 5 graphically illustrates that, under a given strain condition, the deflection curve of r_i^B for the two-end supported curved beam can be graphically generated by rotating the deflection curve of r_i for the cantilever curved beam about the left-hand support point in a clockwise direction until the free end falls on the right-hand support point. In figure 5 the relative geometrical locations of $[r_i^B, r_i, (i/n)r_n]$ appearing in equation (17) are also shown.

Characteristics of the Displacement Transfer Functions

In the Displacement Transfer Functions, equations (15) and (16), the slope angle and deflection (α_i, r_i) at the strain-sensing station s_i are expressed in terms of the inboard beam depth factors $(c_0, c_1, c_2, ..., c_i)$ and the associated inboard surface strains $(\varepsilon_0, \varepsilon_1, \varepsilon_2, ..., \varepsilon_i)$ [for eqs. (15)] or $(\varepsilon_0, \varepsilon_1, \varepsilon_2, ..., \varepsilon_{i+1})$ [for eqs. (16)] including the values of (c_i, ε_i) at the strain-sensing station s_i where (α_i, r_i) are calculated. It is important to mention that equations (15) and (16) are purely geometrical relationships, containing no material properties. However, the values of the surface strains ε_i can be affected by material properties and internal structural configurations. Thus, in using equations (15) and (16) for shape predictions of complex structures such as aircraft wings, there is no need to know the material properties or the internal structural details, and there is no need to construct finite-element models. The shape prediction accuracies of Curvilinear Displacement Transfer Functions, equations (15) through (17) are discussed in detail in the subsequent sections.

Neutral-Axis Offset in Curved Beams

When a curved beam is under bending deformation, the neutral axis may not coincide with the centroid axis (fig. 6). The distance between the neutral axis and the centroid axis is called the neutral-axis offset δ. For example, for a solid uniform curved beam with a rectangular cross section under pure bending, the neutral-axis offset δ can be calculated from equation (18) (ref. 16, p. 148 and ref. 17, p. 183):

$$\delta = R - \frac{h}{\log_e\left(\frac{R + c_c}{R - c_c}\right)} \qquad ; \qquad h = 2c_c \tag{18}$$

In equation (18), h is the beam depth, $c_c (= h/2)$ is the centroid-axis depth factor, and R is the radius of curvature of the deformed curved beam. Table 1 lists the surface stresses and neutral-axis offsets δ [eq. (18)] associated with different curvatures of solid uniform curved beams with rectangular cross sections (data from ref. 16, p. 148).

Table 1. List of surface stresses (k_{in},k_{out}) and neutral-axis offsets $(\delta,\delta/R)$ associated with different curvature R/c_c of solid curved beams with rectangular cross sections (ref. 16, p. 148).

R/c_c	k_{in}	k_{out}	δ	δ/R
1.2	2.89	0.57	0.3660	0.3050
1.4	2.13	0.63	0.2856	0.2040
1.6	1.79	0.67	0.2384	0.1490
1.8	1.63	0.70	0.2016	0.1120
2.0	1.52	0.73	0.1800	0.0900
3.0	1.30	0.81	0.1230	0.0410
4.0	1.20	0.85	0.0840	0.0210
6.0	1.12	0.90	0.0558	0.0093
8.0	1.09	0.92	0.0416	0.0052
10.0	1.07	0.94	0.0330	0.0033
17.0	1.00^{+}	1.00^{-}	0.0170	0.0010

+Slightly greater than 1.00; -Slightly less than 1.00.

In table 1, (k_{in},k_{out}) are respectively the magnitudes of the normalized surface bending stresses on the concave and convex sides of the curved beam defined by equation (19) as:

$$k_{in}=\frac{\sigma_{in}}{\sigma} \quad ; \quad k_{out}=\frac{\sigma_{out}}{\sigma} \tag{19}$$

In equation (19), $\{\sigma_{in},\sigma_{out}\}$ are respectively the magnitudes of the bending stresses on the concave and convex sides of the curved beam, and σ is the magnitude of the surface bending stress for the equivalent straight beam.

In figure 6, the data of (k_{in},k_{out}) and δ/R listed in table 1 are plotted as functions of R/c_c. Note from figure 6 that k_{in} is larger than k_{out}, and both (k_{in},k_{out}) rapidly approach unity $[(k_{in},k_{out})\rightarrow 1]$ with increasing R/c_c. Also, the value of δ/R decreases sharply toward zero as R/c_c increases. At $R/c_c = 17$, both (k_{in},k_{out}) are nearly unity $(k_{in}\approx k_{out}\approx 1)$ and δ/R is decreased to a negligible value of $\delta/R \approx 0.001$. When R/c_c is greater than 17 ($R/c_c > 17$), δ/R is very small $(\delta/R\rightarrow 0)$, and the curved beam behaves like a straight beam because the neutral-axis offset effect diminishes.

Elimination of Axial Strain Components

Unlike straight beams, in the bending of curved beams, the curvature effect will cause the magnitude of outer and inner surface strains at the same cross section to be slightly different because the surface strains contain both bending and axial strain components. To input the correct surface bending strains into the Displacement Transfer Functions, axial strain components must be removed from the total surface strains to obtain the true bending strains. To eliminate the axial strain effect of the embedded curved beams (with unit width), the Neutral-Axis Shifting Method or the Differential-Strain Method can be used. The two methods are described below.

Neutral-Axis Shifting Method

The neutral-axis shifting method is to calculate actual depth factors c_i $(i = 0,1,2,3,...,n)$ using the outer and inner surface strains $(\varepsilon_i, \bar{\varepsilon}_i)$ $(i = 0,1,2,3,...,n)$. Figure 7a shows a typical bending case, in which the two surface strains have opposite signs (for example, $\varepsilon_i > 0$, $\bar{\varepsilon}_i < 0$). The slightly curved strain distribution across the beam depth is represented with bilinear strain distribution (fig. 7a). By setting the total sum of bilinear strains across the beam depth to zero, one obtains equation (20):

$$c_i \varepsilon_i + (h_i - c_i)\bar{\varepsilon}_i = 0 \quad ; \quad (\varepsilon_i > 0,\ \bar{\varepsilon}_i < 0) \tag{20}$$

In equation (20), h_i $(i = 0,1,2,3,...,n)$ is the depth of the embedded curved beam at $s = s_i$. Rewriting equation (20), the depth factor c_i can be expressed by equation (21):

$$c_i = \frac{-\bar{\varepsilon}_i}{\varepsilon_i - \bar{\varepsilon}_i} h_i \quad ; \quad (i = 0,1,2,3,...,n) \tag{21}$$

The depth factors c_i calculated from equation (21) must be used with the associated outer surface strains ε_i for entering the Displacement Transfer Functions for deflection calculations. It must be mentioned that equation (21) may not be very accurate for a highly curved solid embedded beam with $R/c_c < 17$, because of the larger neutral-axis offset δ, and a highly nonlinear strain distribution across the beam depth. The neutral-axis shifting method [eq. (21)] can automatically nullify the axial strain contaminations.

Differential-Strain Method

The differential-strain method presented here is applicable only to a special case for which the neutral axis is located at the half depth of the embedded beam (that is, $c_i = h_i/2$). In view of figure 7b, by using the differential of the outer and inner surface strains, axial strain components can be eliminated to yield the true bending strains given by equation (22):

$$\text{True bending strains on outer-surface} = \frac{\varepsilon_i - \bar{\varepsilon}_i}{2} \quad ; \quad (i = 0,1,2,3,...,n) \tag{22}$$

For inputting the true outer-surface bending strains given by equation (22) into the Curvilinear Displacement Transfer Functions, the given depth factor $c_i (= h_i/2)$ must be used. Note that, if both lower and upper strains $\{\varepsilon_i, \bar{\varepsilon}_i\}$, have the same signs and same magnitudes (that is, $\varepsilon_i = \bar{\varepsilon}_i$) like in axial loading, then equation (22) will give zero bending strain.

Analytical Shape Predictions

The present study of curved-beam structural shape prediction is called the analytical shape prediction study. Because no experimentally measured surface strains are available, MSC/Nastran (MSC Software Corporation, Newport Beach, California) linear analysis (ref. 18, Solution 101) was performed to analytically generate surface strains. The associated Nastran-generated deflections were used as reference yardsticks in the analytical shape prediction accuracy analysis. It is important to mention that when the

surface strains are generated from Nastran nonlinear analysis, the Curvilinear Displacement Transfer Functions will calculate nonlinear deflections for comparisons with Nastran-generated nonlinear deflections.

The analytical method is much cheaper and faster than the experimental method, for which one has to install strain sensors and position transducers (or photogrammetry) for measuring surface strains and deflections. Keep in mind that if the measured surface strain data are available, the analytical method is not needed. The Nastran-generated surface strains were then input to the Curvilinear Displacement Transfer Functions [eqs. (15), (16), or (17)] to calculate the theoretical deflections. By comparing the theoretical deflections with the corresponding Nastran-generated deflections (yardsticks), one can then determine the theoretical shape prediction accuracies.

Shape Prediction Accuracies

To study the shape prediction accuracies of the Curvilinear Displacement Transfer Functions [eqs. (15), (16), or (17)], Nastran-generated deflections $r_i^{(N)}$ were used as reference yardsticks. If r_i (or r_i^B) denotes the theoretically predicted deflections, then the prediction error of deflection r_i (or r_i^B) at the strain-sensing station s_i is defined by the following prediction error equation (23):

$$\text{Prediction error} \equiv \begin{cases} \underbrace{\left(\frac{r_i}{r_i^{(N)}} - 1\right) \times 100\%}_{\text{Cantilever curved beams}} \\ \text{or} \\ \underbrace{\left(\frac{r_i^B}{r_i^{(N)}} - 1\right) \times 100\%}_{\text{Two-end supported curved beams}} \end{cases} ; \quad (i = 0,1,2,3,\ldots,n) \tag{23}$$

Equation (23) is to be used to determine the prediction errors of the Curvilinear Displacement Transfer Functions.

Structures Used in Shape Prediction Analyses

For the shape prediction accuracy analyses of the Curvilinear Displacement Transfer Functions, the structures chosen are a family of curved beams with different initial radius of curvatures, having the dimensions listed in table 2.

Table 2. Dimensions of curved beams analyzed.

l, in. (length)	ϕ_n, deg (curved-beam angle)	R_0, in. (initial radius of curvature)	h, in. (depth)	w, in. (width)	$c_c\ (=h/2)$ in. (centroid-axis depth factor)	R_0/c_c (normalized radius of curvature)
100	0 (Straight)	∞	2.00	2.00	1.00	∞
100	45 (1/8 circle)	127.32	2.00	2.00	1.00	127.32
100	90 (1/4 circle)	63.66	2.00	2.00	1.00	63.66
100	135 (3/8 circle)	42.44	2.00	2.00	1.00	42.44
100	180 (1/2 circle)	31.83	2.00	2.00	1.00	31.83

All the curved beams listed in table 2 are made of an aluminum material ($E = 10 \times 10^6$ lb/in^2, $\nu = 0.3$), and have an identical curved length of $\ell = 100$ in., the same depth of $h = 2$ in., the same width of $w = 2$ in., and the same centroid-axis depth factor of $c_c = h/2 = 1$ in. To maintain the same curved-beam length $\ell = 100$ in., the initial radius of curvature R_0 was changed with the change of the curved-beam angle ϕ_n.

In view of figure 6, the range of $31.83 \le (R_0/c_c) \le \infty$ listed in table 2 lies in the region of $R/c_c > 17$, for which the neutral-axis offset is nearly zero and could be neglected. However, the neutral-axis depth factors c_i $(i = 0,1,2,3,...,n)$ can be calculated from equation (21) for examining the proximity of the neutral-axis depth factor c_i and the centroid-axis depth factor $c_c = h/2$.

Figure 8 shows sketches of a typical cantilever curved beam (fig. 8a), and a two-point supported (fixed or simply supported) curved beam (fig. 8b) analyzed. All the curved beams have constant depth of $(h_0 = h_n)$. Both outer and inner surfaces of each curved beam has $(n+1)$ number of strain-sensing stations; indicated with $(\varepsilon_0, \varepsilon_1, \varepsilon_3, ..., \varepsilon_n)$ for the outer surface, and $(\overline{\varepsilon}_0, \overline{\varepsilon}_1, \overline{\varepsilon}_3, ..., \overline{\varepsilon}_n)$ for the inner surface. The curved beams are subjected to the following loading conditions:

Case a: Each cantilever curved beam is subjected to an inward radial load of $P = 100$ lb at the curved-beam tip, pointing toward the center of curvature (fig. 8a).

Case b: Each two-end supported (fixed or simply supported) curved beam is subjected to an inward radial load of $P = 100$ lb at the curved-beam center, pointing toward the center of curvature (fig. 8b). Note from figure 7b that the radial and tangential motions of the support points are constrained.

The Nastran-generated deformed shapes of all the curved beams based on the dimension listed in table 2 were shown in the following sections.

Shape Predictions of Cantilever Curved Beams

Figure 9 shows Nastran (linear analysis)-generated undeformed and deformed shapes of the different cantilever curved beams (dimensions listed in table 2). Note from figure 9 that the deformed beam-tips moved in both *x*- and *y*-directions.

Nastran-Generated Curved Deflections

The theoretically predicted deflections are curved deflections. However, the Nastran-generated deflections for the cantilever curved beams do not give the curved deflections, but only *x*- and *y*-component deflections (u_i, v_i) $(i = 0,1,2,3,...,n)$ at point s_i (fig. 10). For the purpose of comparison with the theoretically predicted curved deflections r_i, the Nastran version of curved deflections $r_i^{(N)}$ is needed for yardsticks.

By using the Nastran component deflection data of (u_i, v_i), one can then geometrically generate the Nastran curved deflections $r_i^{(N)}$ (yardsticks) with the aid of figure 10. As shown in figure 10, d_i is the straight distance between the undeformed and deformed positions of point s_i and is given by equation (24):

$$d_i \equiv \sqrt{u_i^2 + v_i^2} \quad ; \quad (i = 0,1,2,3,...,n) \tag{24}$$

The distance L_i between the origin and point s_i is the chord length associated with radius R_0 and arc angle $(i/n)\phi_n$, and can be expressed with equation (25):

$$L_i = 2R_0 \sin\left(\frac{i\phi_n}{2n}\right) \quad ; \quad (i = 0,1,2,3,...,n) \tag{25}$$

Now considering L_i as a radius, and d_i as the chord subtending an angle β_i, then d_i can be related to β_i through equation (26):

$$d_i \approx 2L_i \sin\frac{\beta_i}{2} \quad ; \quad (i = 0,1,2,3,...,n) \tag{26}$$

from which β_i can be expressed explicitly with equation (27):

$$\beta_i \approx 2\sin^{-1}\left(\frac{d_i}{2L_i}\right) \quad ; \quad (i = 0,1,2,3,...,n) \tag{27}$$

The Nastran-generated curved deflection $r_i^{(N)}$ can then be considered as an arc length subtended by angle β_i with radius L_i, and can be expressed as equation (28):

$$r_i^{(N)} \approx L_i\beta_i \approx 2L_i \sin^{-1}\left(\frac{d_i}{2L_i}\right) \quad ; \quad (i = 0,1,2,3,...,n) \tag{28}$$

in which equation (27) was used. In view of equations (24)–(26), equation (28) can be written in the following final form as equation (29):

$$r_i^{(N)} \approx 4R_0 \sin\left(\frac{i\phi_n}{2n}\right) \times \sin^{-1}\left[\frac{\sqrt{u_i^2 + v_i^2}}{4R_0 \sin\left(\frac{i\phi_n}{2n}\right)}\right] \quad ; \quad (i = 0,1,2,3,...,n) \tag{29}$$

The Nastran-generated curved deflections $r_i^{(N)}$ calculated from equation (29) can then be used as yardsticks in the shape prediction accuracy analysis of cantilever curved beams.

Data in Table Forms

The Nastran-generated strain and deflection data for different cantilever curved beams are listed in Appendix E (for $n = 20$). The data (for $n = 10$) was added to Appendix E for studying the effect of domain density n on the prediction accuracies. The Nastran-generated curved deflection data of $r_i^{(N)}$ listed in Appendix E were calculated from equation (29), and the depth factors c_i listed were calculated from equation (21). The Nastran-generated outer surface strains ε_i and the depth factor c_i [calculated

from eq. (21)] listed in Appendix E were then input to equations (15) and (16) for the calculations of theoretical curved deflections r_i, which are also listed in Appendix E.

By comparing the theoretical curved deflections r_i with the corresponding Nastran-generated curved deflections $r_i^{(N)}$ (yardsticks), one can then estimate the theoretical shape prediction accuracies based on equation (23).

Strain Curves

Figure 11 shows the Nastran-generated surface strain curves of $\{\varepsilon_i, \bar{\varepsilon}_i\}$ for different cantilever curved beams $(0° \le \phi_n \le 180°)$ including the limit case of the straight beam $(\phi_n = 0°)$. For the straight beam $(\phi_n = 0°)$, the strain curve is a tilted (slanted) straight line, with maximum strain at the fixed end and tapering down linearly to zero at the free end. For the curved beams $(\phi_n > 0°)$, the strain curves are nonlinear, and the degree of downward bend in the inboard region increases with increasing curved-beam angle ϕ_n. At $\phi_n = 180°$ (semicircular beam), the strain curve became a symmetrical mountain shape with a peak at half span and zeros at both fixed and free ends. In figure 11, the magnitudes of the inner surface strains $\bar{\varepsilon}_i$ (negative) were also plotted (dashed curves) for comparisons with the associated strain curves of outward surface strains ε_i (solid curves). Note from figure 11 that for the straight beam $(\phi_n = 0°)$ the magnitudes of inner and outer surface strains $\{\varepsilon_i, \bar{\varepsilon}_i\}$ are identical. For the curved beams $(\phi_n \ne 0°)$, the inner strain curves lie slightly above the corresponding outer strain curves, and the difference between inner and outer strain curves increases with increasing ϕ_n due to increasing curvature effect. The differentials between the inner and outer strain magnitudes indicate curvature-induced slight neutral-axis shifting from the centroid axis (fig. 6).

Deflection Curves

The Nastran-generated surface strain data $\{\varepsilon_i, \bar{\varepsilon}_i\}$ $(i = 0,1,2,3,...,n)$ listed in Appendix E (see also fig. 11) were inputs to equations (15) and (16) for the calculations of the theoretical deflections for the cantilever curved beams. The neutral-axis depth factors c_i $(i = 0,1,2,3,...,n)$ needed for inputs to equations (15) and (16) were calculated from the depth-factor equation (21) using the Nastran-generated surface strain data listed in Appendix E.

Figure 12 shows the deflection curves calculated from the deflection equations (15) and (16) for the cantilever curved beams compared with the associated Nastran-generated deflection curves for the whole range of the curved-beam angles $(0° \le \phi_n \le 180°)$ considered. The deflection curves calculated from equations (15) and (16) are practically coincidental based on the strain curves shown in figure 11. The prediction differences between equations (15) and (16) can show up only when the strain curves are highly bent (ref. 7). For the straight beam $(\phi_n = 0°)$(fig. 12), equations (15) and (16) provide practically perfect shape prediction. At $\phi_n = 45°$ curved-beam case, equations (15) and (16) still give nice shape predictions with only about 2-percent error at the beam-tip. As the curved-beam angle ϕ_n reached $\phi_n = 90°$ and beyond, the beam-tip prediction errors gradually increased due to increasing curvature effect, and finally reached a maximum error of nearly 25 percent at $\phi_n = 180°$. Details of prediction error analysis are presented in the subsequent section; Beam-Tip Prediction Error Reductions.

Curvature-Effect Correction Factors

Because the prediction errors increase with the curved-beam angle ϕ_n, correction factors are needed to bring down the over-prediction errors due to the curvature effect. In view of figure 10, the chord length to arc length ratio can be used to establish simple mathematical functions for the correction factors. The curvature-effect correction factors η_i $(i = 0,1,2,3,...,n)$ to modify the original predicted deflection r_i [eqs. (15) or (16)] at strain-sensing station s_i, at an angular location $\phi_i = (i/n)\phi_n$, can be established as follows in equation (30) (fig. 10):

$$\eta_i \equiv \sqrt{\frac{\text{Chord length } L_i \text{ asociated with radius } R_0 \text{ and angle } \phi_i}{\text{Arc length } Os_i \text{ asociated with radius } R_0 \text{ and angle } \phi}} = \sqrt{\frac{2R_0 \sin(\phi_i/2)}{R_0\phi_i}}$$

$$= \sqrt{\frac{2\sin(\phi_i/2)}{\phi_i}} \xrightarrow[\phi_i \to 0]{\text{Straight beams}} \sqrt{\frac{2(\phi_i/2)}{\phi_i}} = 1 \quad ; \quad (i = 0,1,2,3,...,n) \tag{30}$$

Equation (30) is the square root of the chord length to arc length ratio, and for the straight beams, $\eta_i = 1$ because the chord length and arc length are coincidental straight lines, and no correction is required. The correction factors η_i given by equation (30) were found to provide excellent deflection corrections.

Beam-Tip Prediction Error Reductions

The correction factors η_i given by equation (30) were first applied to modify the original beam-tip deflections r_n $(i = n)$ calculated from equations (15) [or eqs. (16)] for studying the beam-tip prediction error reductions. Note that r_n calculated from equations (15), and (16) are extremely close (see figure 12 and Appendix E). The prediction errors of the original deflections r_n [eqs. (15)] and the corrected beam-tip deflections $\eta_n \cdot r_n$ are compared in table 3.

Table 3. Beam-tip deflection prediction errors for different cantilever curved beams.

ϕ_n, deg (curved-beam angle)	$r_n^{(N)}$, in. (Nastran deflections)	r_n, in. [Theory, eq. (15)]	Percent error (No corrections)	η_n (Correction factor)	$(\eta_n \cdot r_n)$ (Corrected deflections)	Percent error (With corrections)
0 (Straight)	2.50077	2.50125	0.0192	1.00000	2.50125	0.0192
45	2.30685	2.35569	2.1172	0.98717	2.32547	0.8072
90	1.80041	1.94475	8.0171	0.94885	1.84528	2.4922
135	1.16759	1.36976	17.3152	0.88556	1.21301	3.8901*
180	0.61306	0.76542	24.8524*	0.79789	0.61072	0.3817

*Maximum error for each type of error

Figure 13 shows original and corrected prediction errors of the beam-tip deflections and the beam-tip correction factor η_n listed in table 4 plotted as functions of curve beam angle ϕ_n. Note that the original prediction error curve is a shallow *s*-shaped curve with peak prediction error of 24.8524 percent at $\phi_n = 180°$. The corrected prediction error curve is a projectile-trajectory shaped with the peak error of

3.8901 percent occurring at $\phi_n = 135°$. Note also from figure 13 that the value of η_n is unity $(\eta_n = 1)$ at $\phi_n = 0°$ (straight beams) and decreases slowly down to $\eta_n = 0.79789$ at $\phi_n = 180°$.

Correction Factor Table

The complete set of the curvature-effect correction factors $\eta_i \ (i = 0,1,2,3,...,n)$ calculated from equation (30) for a different strain-sensing station $s_i \ (i = 0,1,2,3,...,n)$ and for the whole range of curved-beam angles $0° \le \phi_n \le 180°$ are listed in table 4.

Table 4. Curvature-effect correction factors η_i for different cantilever curved beams.

	η_i				
i	$\phi_n = 0°$	45°	90°	135°	180°
0	1.0000	1.0000	1.0000	1.0000	1.0000
1	1.0000	1.0000	0.9999	0.9997	0.9995
2	1.0000	0.9999	0.9995	0.9988	0.9979
3	1.0000	0.9997	0.9988	0.9974	0.9954
4	1.0000	0.9995	0.9979	0.9954	0.9918
5	1.0000	0.9992	0.9968	0.9928	0.9872
6	1.0000	0.9988	0.9954	0.9896	0.9815
7	1.0000	0.9984	0.9937	0.9859	0.9749
8	1.0000	0.9979	0.9918	0.9815	0.9672
9	1.0000	0.9974	0.9896	0.9766	0.9585
10	1.0000	0.9968	0.9872	0.9712	0.9489
11	1.0000	0.9961	0.9845	0.9651	0.9382
12	1.0000	0.9954	0.9815	0.9585	0.9265
13	1.0000	0.9946	0.9783	0.9514	0.9138
14	1.0000	0.9937	0.9749	0.9436	0.9002
15	1.0000	0.9928	0.9712	0.9353	0.8856
16	1.0000	0.9918	0.9672	0.9265	0.8700
17	1.0000	0.9907	0.9630	0.9171	0.8534
18	1.0000	0.9896	0.9585	0.9071	0.8359
19	1.0000	0.9884	0.9538	0.8966	0.8174
20	1.0000	0.9872	0.9489	0.8856	0.7979

The data of curvature-effect correction factors $\eta_i \ (i = 0,1,2,3,...,n)$ listed in table 4 are plotted in figure 14 to show the functional behavior of η_i with the changing curved-beam angle ϕ_n. For each curved-beam angle, the correction factor is unity at the beam fixed end and gradually decreases in the span-wise direction and reach a minimum value at the beam tip. In figure 14, the values of the beam-tip correction factors $\eta_n (i = n)$ for different curved-beam angles are indicated.

Corrected Deflection Curves

The deflection correction factors $\eta_i \ (i = 0,1,2,3,...,n)$ listed in table 4 were then used to multiply the original deflection $r_i \ (i = 0,1,2,3,...,n)$ calculated from equations (15) and (16). The resulting new set of

corrected deflections $(\eta_i \cdot r_i)$ are plotted in figure 15. It is very encouraging to observe the graphical proximity of the corrected theoretical deflection curves and the associated Nastran-generated deflection curves for the whole range of curved-beam angles $0° \le \phi_n \le 180°$, and thus validating the empirically established correction factor η_i in simple mathematical functions.

Figure 16 shows the Nastran (linear analysis)-generated undeformed and deformed shapes of different two-end fixed curved beams (fig. 8b), each of which is subjected to an inward load of $P = 100$ lb at the beam center.

Data in Table Forms

The Nastran-generated strains $\{\varepsilon_i, \bar{\varepsilon}_i\}$ $(i = 0,1,2,3,...,n)$ and Nastran-generated deflections $r_i^{(N)}$ for the two-end fixed curved beams (for $n = 20$) are listed in Appendix F. The data (for $n = 10$) was added to Appendix F for studying the effect of domain density n on the calculated deflections. For the two-end supported curved beams, $r_i^{(N)}$ listed are the Nastran radial displacements and are not calculated from equation (29). The Nastran-generated strain data of $\{\varepsilon_i, \bar{\varepsilon}_i\}$ listed in Appendix F were then used to calculate the theoretical deflections $(r_i^B, \hat{r}_i)$ respectively from deflection equation (17) and corrected deflection to be discussed in the Deflection Corrections section). The resulting theoretical data of $(r_i^B, \hat{r}_i)$ are also listed in Appendix F. Deflection equation (17) was used in conjunction with the cantilever-beam deflection equation (15). The cantilever-beam deflection equation (16) was not used because both equations (15) and (16) gave practically identical theoretical deflections for the present curved-beam geometries (see Appendix E).

In the theoretical deflection calculations, two data input cases were considered:

- Case 1: using calculated depth factors $c_i = (\varepsilon_i h_i)/(\varepsilon_i - \bar{\varepsilon}_i)$ [eq. (21)] and associated outer surface strains ε_i (see fig. 6a).
- Case 2: using given depth factors $c_i = h_i/2$ and true bending strain $(\varepsilon_i - \bar{\varepsilon}_i)/2$ [eq. (22)] (see fig. 6b).

For certain curved-beam angles ϕ_n, Case 1 data inputs could provide more accurate theoretical deflections than Case 2 data inputs, however, for other curved-beam angles ϕ_n the opposite is true. The depth factors c_i (given or calculated) are also listed in Appendix F. The detailed discussions of the theoretical deflections $(r_i^B, \hat{r}_i)$ are presented in the subsequent sections.

Strain Curves

Figure 17 shows the strain curves for two-end fixed curved beams with different curved-beam angles $(0° \le \phi_n \le 180°)$ including the limit case of straight beam $(\phi_n = 0°)$ based on Nastran-generated surface strains $\{\varepsilon_i, \bar{\varepsilon}_i\}$ listed in Appendix F. The strain curves for the outer surface strains ε_i are shown with solid curves with solid circular symbols, and the strain curves for the inner surface strains $\bar{\varepsilon}_i$ with dashed curves with open circular symbols. The strain curves of $\bar{\varepsilon}_i$ are almost the mirror images of the corresponding strain curves of ε_i, indicating very little axial-strain contaminations. For the straight beam $(\phi_n = 0°)$, the strain curves of $\{\varepsilon_i, \bar{\varepsilon}_i\}$ are linear and are V-shaped and inverted-V-shaped respectively.

For the curved beams $(\phi_n > 0°)$, the strain curves of $\{\varepsilon_i, \overline{\varepsilon}_i\}$ become nonlinear and change very little with curve beam angle ϕ_n, and are respectively M-shaped and W-shaped (inverted-M-shaped).

Deflection Curves

The Nastran-generated strain data $\{\varepsilon_i, \overline{\varepsilon}_i\}$ $(i = 0,1,2,3,...,n)$ listed in Appendix F (see also fig. 17) were used to calculate theoretical deflections from equation (17) [in conjunction with the cantilever deflection equation (15)].

Figures 18 show the theoretical deflection curves, calculated from deflection equations (17) for two-end fixed curved beams with different curved-beam angles $(0° \le \phi_n \le 180°)$, compared with associated Nastran-generated deflection curves. For the curved-beam angles of $\phi_n = 0°, 45°$ (figs. 18a, and 18b), the theoretical deflection curves were calculated by using Case 1 input. For the curved-beam angles of $\phi_n = 90°, 135°, 180°$ (figs. 18c–18e), the theoretical deflection curves were calculated by using Case 2 input.

For the straight beam $(\phi_n = 0°)$ (fig. 18a), equation (17) gives practically perfect shape prediction with a beam-center prediction error of only 0.4 percent. At the $\phi_n = 45°$ curved-beam case, equation (17) still gives nice shape predictions with beam-center prediction errors of only 1 percent. As the curved-beam angle ϕ_n continues to increase, the curvature-effect caused the prediction errors to increase and finally reached a maximum beam-center prediction error of nearly 20 percent at $\phi_n = 180°$.

Deflection Corrections

As shown in figures 18a–e, the theoretical deflection curves start to lie slightly below the associated Nastran-generated deflection curves as the curved-beam angle ϕ_n increases. Note that the theoretical and Nastran deflection curves contain negative and positive deflection regions. In the negative deflection regions (for example, figs. 18d and 18e), less-than-unity correction factors (that is, reducing deflection magnitudes) are needed to bring up the theoretical deflection curve toward the Nastran deflection curve. However, in the central positive deflection region, greater-than-unity correction factors (that is, increasing deflection magnitudes) are needed to bring the theoretical deflection curve toward the Nastran deflection curve. Thus, two sets of correction factors must be developed for those regions. A simpler approach is to develop a single set of shifting correction factors for shifting both positive and negative deflection regions of each theoretical deflection curve upward toward the associated Nastran deflection curve. The following section describes the formulations of the shifting factors needed to shift the theoretical curves upward toward the associated Nastran deflection curves.

Beam-Center Correction Factors

The correction factor $\widehat{\eta}_{n/2}$ at the beam-center of the two-end fixed curved beam is the basis for formulating the shifting factors. Because of loading symmetry (figs. 18a–18e), half of each two-end fixed curved beam can be considered as a cantilever curved beam. For the cantilever-curved beams, the Displacement Theory over-predicts the deflections (fig. 12), and therefore, less-than-unity beam-tip correction factors $\eta_n < 1$ are needed. However, for the two-end fixed curved beams (figs. 18a–18e) greater-than-unity beam center correction factors $\widehat{\eta}_{n/2} > 1$ are needed because of under predictions. Therefore, the correction factor $\widehat{\eta}_{n/2}$ at the beam center of each two-end fixed curved beam can be

assumed as the reciprocal of the beam-tip correction factor η_n of the cantilever curved beam (that is, $\hat{\eta}_{n/2} = 1/\eta_n$) and can be expressed in the following functional form [eq. (31)]:

$$\hat{\eta}_{n/2} \equiv \frac{1}{\eta_n} = \sqrt{\frac{R_0\phi_n}{2R_0\sin(\phi_n/2)}} = \sqrt{\frac{R_0(2\phi_{n/2})}{2R_0\sin(2\phi_{n/2}/2)}} = \sqrt{\frac{\phi_{n/2}}{\sin\phi_{n/2}}} \xrightarrow[\phi_{n/2}\to 0]{\text{Straight beams}} \sqrt{\frac{\phi_{n/2}}{\phi_{n/2}}} = 1 \qquad (31)$$

The values of beam-center correction factors $\hat{\eta}_{n/2}$ calculated from equation (31), and the original and corrected beam-center deflection prediction errors for different two-end fixed curved beams are listed in table 5.

Table 5. Beam-center deflection prediction errors for different two-end fixed curved beams.

ϕ_n, deg (Curved-beam angle)	$r_{n/2}^{(N)}$, $\times 10^{-3}$ in. (Nastran deflections)	$r_{n/2}^{B}$, $\times 10^{-3}$ in. [Predicted, eq. (17)]	Percent error (No corrections)	$\hat{\eta}_{n/2}$ (Correction factor)	$(\hat{\eta}_{n/2} \cdot r_{n/2}^{B})$, $\times 10^{-3}$ in. (Corrected deflection)	Percent error (With corrections)
0 (straight)	39.22598	39.06338	0.4145	1.00000	39.06338	0.4145
45	3.88487	3.83972	1.1622	1.01300	3.88964	0.1228
90	2.93245	2.86044	2.4555	1.05391	3.01464	2.8028*^
135	2.85180	2.58618	9.3142	1.12923	2.92039	2.4051
180	2.95484	2.34952	20.4857*	1.25331	2.94469	0.3437

*Maximum errors ^No improvement

Figure 19 shows the original and corrected beam-center prediction errors and the beam-center correction factor $\hat{\eta}_{n/2}$ of table 5 plotted as functions of curve beam angle ϕ_n. Note that the original beam-center prediction error curve is concave upward with a peak prediction error of 20.4857 percent at $\phi_n = 180°$. Note that the corrected prediction error decreases from 0.4145 percent error at $\phi_n = 0°$ to a minimum error of 0.1228 percent at $\phi_n = 45°$, and then reaches the peak error of 2.8028 percent at $\phi_n = 90°$ (practically no improvement), and finally decreased to 0.3437 percent at $\phi_n = 180°$ (great error reduction). Note also from figure 19 that the $\hat{\eta}_{n/2}$-curve is very similar to the original error curve, giving unity $(\eta_{n/2} = 1)$ at $\phi_n = 0°$ (straight beams), and bend upwardly giving a peak value of $\hat{\eta}_{n/2} = 1.25331$ at $\phi_n = 180°$.

Shifting Factors

In view of the beam center correction factor $\hat{\eta}_{n/2}$, one can now define $(\hat{\eta}_{n/2} - 1)$ as the beam-center shifting factor to shift each original deflection curve at the beam center toward the corresponding Nastran deflection curve at the beam center (figs. 18a–18e). For shifting other points, the magnitude of shift factor $(\hat{\eta}_{n/2} - 1)$ must be adjusted. Note that the amount of upward shifting of each original deflection curve toward the associated Nastran deflection curve is zero at the left support point (i = 0), and increases nonlinearly with i and reaching a maximum shifting factor of $(\hat{\eta}_{n/2} - 1)$ at the beam center $(i = n/2)$ because of symmetrical loading. Then, the upward shifting factor at strain-sensing station s_i

$(i = 0,1,2,3,...,n/2)$ on the left half of the two-end fixed curved beam can be expressed with a simple function given by equation (32):

$$(\text{Shifting factor at } s_i) = (\hat{\eta}_{n/2} - 1)\left(\frac{2i}{n}\right)^2 \quad ; \quad (i = 0,1,2,3,...,n/2) \tag{32}$$

Using equation (32), the corrected deflection $\hat{r}_i$ at strain-sensing station s_i on the left half of the two-end fixed curved beam can be expressed with equation (33) as:

$$\hat{r}_i = \underbrace{r_i^B}_{\text{Eq. (17)}} + \underbrace{(\hat{\eta}_{n/2} - 1)\left(\frac{2i}{n}\right)^2}_{\text{Shifting factor st } s_i} \underbrace{r_{n/2}^B}_{\text{Eq. (17)}} = r_i^B + \left(\sqrt{\frac{\phi_{n/2}}{\sin\phi_{n/2}}} - 1\right)\left(\frac{2i}{n}\right)^2 r_{n/2}^B \tag{33}$$

$$(i = 0,1,2,3,....,n/2)$$

Equation (33) is for the left half of the two-end fixed curved beam under symmetrical loading. Therefore, the corrected deflection curve for the right-hand side will be the mirror image of the left-hand side deflection curve calculated from equation (33). It must be mentioned that if the loading point is not at the exact center of the two-end fixed curved beam, two different shifting factors [similar to eq. (33)] must be formulated for left and right sides of the loading point. The data from equation (33) is listed in the last column of Appendix F.

The corrected-prediction errors at $s = s_i$ can then be calculated from equation (34):

$$\text{Corrected-prediction error} \equiv \underbrace{\left(\frac{\hat{r}_i}{r_i^{(N)}} - 1\right) \times 100\%}_{\substack{\text{Two-end supported} \\ \text{curved beams}}} \quad ; \quad (i = 0,1,2,3,....,n/2) \tag{34}$$

Corrected Deflection Curves

Figures 20a–20e show the corrected deflection curves calculated from equation (33) compared with the corresponding Nastran-generated deflection curves for the two-end fixed curved beams. Note that excellent agreement can be achieved between the theory and Nastran by using the shifting factor of a simple mathematical functional form [eq. (32)].

Shape Predictions of Two-End Simply Supported Curved Beams

Figure 21 shows the Nastran (linear analysis)-generated undeformed and deformed shapes of different two-end simply supported curved beams (fig. 8b), each of which is subjected to an inward load of $P = 100$ lb at the beam center.

Data in Table Forms

The Nastran-generated strains $\{\varepsilon_i, \bar{\varepsilon}_i\}$ $(i = 0,1,2,3,...,n)$ and Nastran-generated deflections $r_i^{(N)}$ for the two-end simply supported curved beams are listed in Appendix G. For the two-end simply supported curved beams, $r_i^{(N)}$ listed in Appendix G are the Nastran-generated radial displacements and are not

calculated from equation (29). The Nastran-generated strain data of $\{\varepsilon_i, \overline{\varepsilon}_i\}$ listed in Appendix G were then used to calculate the theoretical deflections $(r_i^B, \widehat{r}_i)$ respectively from deflection equation (17) and the corrected deflection equation (33). The resulting theoretical data of $(r_i^B, \widehat{r}_i)$ are also listed in Appendix G. Both deflection equations (17) and (33) were used in conjunction with the cantilever-beam deflection equation (15). The cantilever-beam deflection equation (16) was not used because both equations (15) and (16) gave very close theoretical deflections for the present curved-beam geometries (see Appendix E).

Similar to the two-end fixed cases, in the calculations of the theoretical deflections for the two-end simply supported cases, two input cases were considered:

- Case 1 input: using calculated depth factors $c_i = (-\overline{\varepsilon}_i h_i)/(\varepsilon_i - \overline{\varepsilon}_i)$ [eq. (21)] and outer surface strains ε_i (Appendix G) (see fig. 7a).
- Case 2 input: using given depth factor $c_i = h_i/2$ and true bending strain $(\varepsilon_i - \overline{\varepsilon}_i)/2$ [eq. (22)] (see fig. 7b).

Similar to the two-end fixed cases, for certain curved-beam angles ϕ_n, Case 1 data inputs could give more accurate theoretical deflections than Case 2 data inputs, however, for other curved-beam angles ϕ_n the reverse is true. The depth factors c_i (given or calculated) are also listed in Appendix G. The detailed discussions of the theoretical deflections $(r_i^B, \widehat{r}_i)$ are presented in the subsequent sections.

Strain Curves

Figure 22 shows the plots of Nastran-generated surface strains $(\varepsilon_i, \overline{\varepsilon}_i)$ (data listed in Appendix G) for two-end simply supported curved beams with different curved-beam angles $(0° \le \phi_n \le 180°)$ including the limit case of the straight beam $(\phi_n = 0°)$. The strain curves for the outer surface strains ε_i are shown with solid curves with solid circular symbols, and the strain curves for the inner surface strains $\overline{\varepsilon}_i$ are shown with dashed curves with open circular symbols. The strain curves of $\overline{\varepsilon}_i$ are practically the mirror images of the corresponding strain curves of ε_i. For the straight beam $(\phi_n = 0°)$, the strain curves of $(\varepsilon_i, \overline{\varepsilon}_i)$ are linear, V-shaped, and inverted V-shaped respectively. For the curved beams $(\phi_n > 0°)$, the strain curves of $(\varepsilon_i, \overline{\varepsilon}_i)$ become M- and W-shaped respectively, and the shapes of the strain curves change very little with the curve-beam angle ϕ_n.

Deflection Curves

The Nastran-generated surface strain data $\{\varepsilon_i, \overline{\varepsilon}_i\}$ $(i = 0,1,2,3,...,n)$ listed in Appendix G (see also fig. 22) were inputs to deflection equation (17) [in conjunction with the cantilever deflection equation (15)] for the calculation of theoretical deflections.

Figures 23a–23e show the theoretical deflection curves calculated from deflection equations (17) for two-end simply supported curved beams with different curved-beam angles $(0° \le \phi_n \le 180°)$ compared with the associated Nastran-generated deflection curves. For the curved-beam angles of $\phi_n = 0°, 45°, 90°$ (figs. 23a–23c), the theoretical deflection curves were calculated by using Case 1 input. For the curved-beam angles $\phi_n = 135°, 180°$ (fig. 23d and 23e), the theoretical deflection curves were calculated by using Case 2 input.

For the straight beam $(\phi_n = 0°)$ (fig. 23a), equations (17) give practically perfect shape prediction with a beam-center prediction error of the minuscule amount of 0.1 percent. As the curved-beam angle ϕ_n continues to increase, the curvature-effect caused the prediction errors to increase and finally reached a maximum beam-center prediction error of nearly 24 percent at $\phi_n = 180°$ (see following sections).

Deflection Corrections

As shown in figures 23a–23e, as the curved-beam angle ϕ_n increases, the theoretical deflection curves start to lie slightly below the associated Nastran-generated deflection curves. Therefore, the process of deflection corrections for the two-end simply supported curved beams is similar to that developed for the two-end fixed curved beams presented earlier.

Beam-Center Correction Factors

The beam-center correction factor $\hat{\eta}_{n/2}$ [eq. (31)] used for the two-end fixed cases can also be used for the two-end simply-supported cases. The values of beam-center correction factor $\hat{\eta}_{n/2}$ from table 5 and the original and corrected beam-center deflection prediction errors for different two-end simply supported curved beams are listed in table 6.

Table 6. Beam-center prediction errors of different two-end simply supported curved beams.

ϕ_n, deg (Curved-beam angle)	$r_{n/2}^{(N)}$, $\times 10^{-3}$ in. (Nastran deflections)	$r_{n/2}^{B}$, $\times 10^{-3}$ in. [Predicted, eq. (17)]	Percent error (No corrections)	$\hat{\eta}_{n/2}$ (Correction factor)	$(\hat{\eta}_{n/2} \cdot r_{n/2}^{B})$, $\times 10^{-3}$ in. (Corrected deflections)	Percent error (With corrections)
0 (Straight)	156.41640	156.25385	0.1039	1.00000	156.25385	0.1039
45	4.71772	4.63543	1.7444	1.01300	4.69569	0.4670
90	4.12791	3.85040	6.7228	1.05391	4.05798	1.6941
135	4.26094	3.86657	9.2554	1.12923	4.36625	2.4715
180	4.64366	3.51465	24.3129*	1.25331	4.40495	5.1406*

*Maximum errors

Figure 24 shows the original and corrected beam-center prediction errors (table 6) and the beam-center correction factor $\hat{\eta}_{n/2}$ (table 6) plotted as functions of the curve beam angle ϕ_n. Note that the original beam-center prediction error is 0.1039 percent at $\phi_n = 0°$ (straight beam) and increases wavy-upward to a maximum prediction error of 24.3129 percent at $\phi_n = 180°$. Note also that the corrected prediction error curve is also slightly wavy-upward with peak error of 5.1406 percent at $\phi_n = 180°$ (great error reduction). Keep in mind that the $\hat{\eta}_{n/2}$-curve (dashed curve) of figure 24 for the two-end simply supported cases is identical to the $\hat{\eta}_{n/2}$-curve (dashed curve) of figure 19 for the two-end fixed cases.

Shifting Factors

There is no need to develop different shifting factors for the two-end simply supported curved beams. The shifting factors [eq. (22)] and the corrected deflection equation (33) developed for the two-end fixed supported curved beams can also be used for the upward shifting of the original deflection curves (figs. 23a–23e) of the two-end simply supported cases.

Corrected Deflection Curves

The corrected deflection equation (33) can also be used for upward shifting of the original deflection curves (figs. 23a–23e) of the two-end simply supported cases. The corrected deflection curves calculated from equation (33) for the two-end simply supported curved beams are plotted in figures 25a–25e for comparisons with the associated Nastran-generated deflection curves (yardstick). Note that by using the shifting factor of simple mathematical functional form [eq. (32)], excellent correlations between the theory and Nastran could be achieved except for $\phi_n = 180°$ case, for which the correlation is slightly off (fig. 25e).

Effect of Domain Density on Prediction Accuracies

This section examines the effect of domain density n on the shape prediction accuracies. Two domain densities: $n = 20$ $(\Delta l = l/n = 100/20 = 5$ in.) and $n = 10$ $(\Delta l = l/n = 100/10 = 10$ in.) were considered in the accuracy analysis. For studying the effect of domain density n on the prediction accuracies, two cases of cantilever-curved beams $(\phi_n = 45° - 180°)$ were considered because of marked different shapes of the two associated strain curves (fig. 11). Also, because the strain curves of different two-end supported curved beams $(\phi_n = 45°, 180°)$ have very similar shapes (figs. 17 and 22), only one case of the two-end fixed curved beam $(\phi_n = 45°)$ was considered.

Cantilever Curved Beams

The Nastran-generated strain and deflection data, and the theoretical deflection data for the two cantilever curved beams $(\phi_n = 45°, 180°)$ based on two domain densities $(n = 20,\ n = 10)$ are listed in Appendix E. Tables 7a and 7b compare the theoretical deflections r_i calculated from equation (15) for the two domain densities $(n = 20,\ n = 10)$ (see Appendix E), and the corrected deflections $(\eta_i \cdot r_i)$ using correction factors η_i for $(\phi_n = 45°, 180°)$ listed in table 4. Equation (16) was not used because the values of deflections r_i calculated from equations (15) and (16) are extremely close (see Appendix E).

Table 7a. Comparisons of theoretical deflections r_i calculated from equation (15) and corrected deflections $(\eta_i \cdot r_i)$ for $\phi_n = 45°$ cantilever curved beam based on two domain densities $(n = 20,$ $n = 10)$ and a beam-tip load of $P = 100$ lb.

	r_i, in. [Predicted deflections, eq. (15)]				$(\eta_i \cdot r_i)$ in. (Corrected deflections)		
i	$n = 20$	$n = 10$	i	i	$n = 20$	$n = 10$	
0	0.00000	0.00000	0	0	0.00000	0.00000	0
1	0.00836			1	0.00836		
2	0.03298	0.03297	1	2	0.03298	0.03297	1
3	0.07315			3	0.07314		
4	0.12815	0.12810	2	4	0.12809	0.12804	2
5	0.19722			5	0.19706		
6	0.27958	0.27949	3	6	0.27925	0.27916	3
7	0.37445			7	0.37385		
8	0.48100	0.48087	4	8	0.47999	0.47986	4
9	0.59841			9	0.59065		
10	0.72583	0.72564	5	10	0.72351	0.72332	5
11	0.86240			11	0.85904		
12	1.00726	1.00695	6	12	1.00263	1.00232	6
13	1.15952			13	1.15326		
14	1.31827	1.31775	7	14	1.30997	1.30945	7
15	1.48260			15	1.47193		
16	1.65160	1.65082	8	16	1.63806	1.63728	8
17	1.82434			17	1.80737		
18	1.99990	1.99885	9	18	1.97910	1.97806	9
19	2.17733			19	2.15298		
20	2.35569	2.35442	10	20	2.32547	2.32428	10

Nastran = 2.30685 in. Nastran = 2.30514 in.

Table 7b. Comparisons of theoretical deflections r_i calculated from equation (15) and corrected deflections $(\eta_i \cdot r_i)$ for $\phi_n = 180^\circ$ cantilever curved beam based on two domain densities $(n = 20,\ n = 10)$ and a beam-tip load of $P = 100$ lb.

	r_i, in. [Predicted deflections, eq. (15)]				$(\eta_i \cdot r_i)$, in. (Corrected deflections)		
i	$n = 20$	$n = 10$	i	i	$n = 20$	$n = 10$	i
0	0.00000	0.00000	0	0	0.00000	0.00000	0
1	0.00016			1	0.00016		
2	0.00126	0.00125	1	2	0.00125	0.00124	1
3	0.00420			3	0.00418		
4	0.00987	0.00983	2	4	0.00979	0.00975	2
5	0.01906			5	0.01881		
6	0.03249	0.03236	3	6	0.03189	0.03176	3
7	0.05078			7	0.04950		
8	0.07440	0.07409	4	8	0.07196	0.07166	4
9	0.10375			9	0.09944		
10	0.13902	0.13842	5	10	0.13191	0.13134	5
11	0.18029			11	0.16914		
12	0.22749	0.22649	6	12	0.21077	0.20985	6
13	0.28040			13	0.25624		
14	0.33866	0.33717	7	14	0.30486	0.30351	7
15	0.40177			15	0.35579		
16	0.46912	0.46705	8	16	0.40811	0.40631	8
17	0.54000			17	0.46083		
18	0.61359	0.61087	9	18	0.51287	0.51060	9
19	0.68904			19	0.56319		
20	0.76542	0.76203	10	20	0.61072	0.60801	10
					Nastran: 0.61306 in.	Nastran: 0.60598 in.	

Note from tables 7a and 7b that the two sets of deflection data based on $n = 20$ and $n = 10$ are quite close, indicating that using less domain density of $n = 10$ (less strain sensors), one can still obtain comparable theoretical deflections. The footnotes of tables 7a and 7b show Nastran-generated beam tip deflections $r_n^{(N)}$ (see Appendix E) based on the two domain densities $(n = 20,\ n = 10)$. Note that for $\phi_n = 45^\circ$ (table 7a), the two Nastran-generated beam-tip deflections for $(n = 20,\ n = 10)$ are extremely close [$r_n^{(N)} = (2.30685,\ 2.30514)$ in.] with negligible difference of only 0.0741 percent. For $\phi_n = 180^\circ$ (table 7b), the two Nastran-generated beam-tip deflections are also very close [$r_n^{(N)} = (0.60136,\ 0.60598)$ in.] with a small difference of only 0.8226 percent.

Deflection Curves Comparisons

Figures 26 and 27 show the theoretical deflection curves of r_i (figs. 26a and 27a) and the corrected deflection curves of $(\eta_i \cdot r_i)$ (figs. 26b and 27b) for the cantilever-curved beams $(\phi_n = 45^\circ, 180^\circ)$ based on the data listed in tables 7a and b. The associated Nastran-generated deflection curve shown in figures 26 and 27 are for the domain density $n = 20$ (data in Appendix E). Note from figures 26a and 27a that the theoretical deflection curves based on the two domain densities $(n = 20,\ n = 10)$ are

graphically indistinguishable. For the $\phi_n = 45°$ case (fig. 26a), the two theoretical deflection curves are slightly off from the Nastran-generated deflection curve. For the $\phi_n = 180°$ case (fig. 27a), the two theoretical deflection curves diverged from the Nastran-generated deflection curve in the outboard region.

With the corrections (figs. 26b and 27b), the two theoretical curves and the associated Nastran deflection curves practically collapsed into a single deflection curve. The good agreement indicates that using the domain density $n = 10$ (instead of $n = 20$) can be adequate for sufficiently accurate shape predictions.

Beam-Tip Prediction Error Comparisons

The beam-tip deflection data listed in tables 7a and b were used to compare the beam-tip prediction errors based on the two domain densities $(n = 20, n = 10)$. Table 8 lists the beam-tip deflection prediction errors for the cantilever curved beams $(\phi_n = 45°, 180°)$ based on the two domain densities $(n = 20, n = 10)$.

Table 8. Beam-tip deflection prediction errors for cantilever curved beams $(\phi_n = 45°, 180°)$ based on two domain densities $(n = 20, n = 10)$ and a beam-tip load of $P = 100$ lb.

n (Domain density)	$r_n^{(N)}$, in. [Nastran eq. (28)]	r_n, in. [Predicted eq. (15)]	Percent error (No corrections)	η_n (Correction factor)	$(\eta_n \cdot r_n)$ in. (Corrected deflection)	Percent error (With corrections)
			$(\phi_n = 45°)$			
20	2.30685	2.35569	2.1172	0.9872	2.32554	0.8102
10	2.30514	2.35442	2.1378	0.9872	2.32428	0.8303
			$(\phi_n = 180°)$			
20	0.61036	0.76542	25.4047	0.7979	0.61072	0.0590
10	0.60598	0.76203	25.7517	0.7979	0.60801	0.3350

Note from table 8 that the beam-tip deflections r_n calculated from equation (15) and the corrected deflections $(\eta_n \cdot r_n)$ based on the two domain densities $(n = 20, n = 10)$ are extremely close. Without correction factors, the beam-tip prediction errors are (2.1172, 2.1378) percent $(\phi_n = 45°)$, and (25.4047, 25.7517) percent $(\phi_n = 180°)$ respectively for $(n = 20, n = 10)$. With the corrections, the beam tip prediction errors can be greatly reduced to a negligible range of (0.8102, 0.8303) percent $(\phi_n = 45°)$, and {0.0590, 0.3350) percent $(\phi_n = 180°)$ respectively for $(n = 20, n = 10)$. This finding indicates that using less domain density, $n = 10$ (less number of strain sensors), can be considered adequate for the shape predictions of current curved-beam geometry. The insensibility of the domain density *n* on the shape prediction accuracies was also investigated earlier for the straight beam cases $(\phi_n = 0°)$ (ref. 1).

Two-End Fixed Curved Beam

A typical two-end fixed curved beam $(\phi_n = 45°)$ was chosen to study the effect of the domain density n. The Nastran-generated strain and deflection data, and the theoretical deflections of the $\phi_n = 45°$ two-end fixed curved beam based on two domain densities $(n = 20, n = 10)$ are listed in

Appendix F. From Appendix F, the theoretical deflections $(r_i^B, \hat{r}_i)$ calculated respectively from equations (17) and (33) for the two-end fixed curved beam $(\phi_n = 45°)$ for the two domain densities $(n = 20, n = 10)$ are compared in table 9.

Table 9. Comparison of theoretical deflections of the two-end fixed curved beam $(\phi_n = 45°)$ calculated from equations (17) and (33) based on two domain densities $(n = 20, n = 10)$ and a central load of $P = 100$ lb. $n = 20$

	r_i^B, $\times 10^{-3}$ in. [Predicted deflections, eq. (17)]				$\hat{r}_i$, $\times 10^{-3}$ in. [Corrected deflections, eq. (33)]		
i	$n = 20$	$n = 10$	i	i	$n = 20$	$n = 10$	i
0	0.00000	0.00000	0	0	0.00000	0.00000	0
1	-0.18173			1	-0.18123		
2	-0.51496	-0.51540	1	2	-0.51296	-0.51341	1
3	-0.74583			3	-0.74134		
4	-0.70590	-0.70716	2	4	-0.69792	-0.69918	2
5	-0.31252			5	-0.30004		
6	0.43107	0.42889	3	6	0.44905	0.44685	3
7	1.43581			7	1.46027		
8	2.52679	2.52338	4	8	2.55874	2.55530	4
9	3.44331			9	3.48375		
10*	3.83972	3.83572	5*	10*	3.88964	3.88559	5*
11	3.44325			11	3.48375		
12	2.52663	2.52338	6	12	2.55874	2.55530	6
13	1.43549			13	1.46027		
14	0.43056	0.42889	7	14	0.44905	0.44685	7
15	-0.31310			15	-0.30004		
16	-0.70644	-0.70716	8	16	-0.69792	-0.69918	8
17	-0.74627			17	-0.74134		
18	-0.51524	-0.51540	9	18	-0.51296	-0.51341	9
19	-0.18180			19	-0.18123		
20	0.00000	0.00000	10	20	0.00000	0.00000	10

*Beam center Beam center: Nastran = 3.88487×10^{-3} in. Nastran = 3.87851×10^{-3} in.

Note from table 9 that the two sets of deflection data based on $(n = 20, n = 10)$ are quite close, indicating that by using less domain density of $n = 10$ (less strain sensors), one can still obtain comparable theoretical deflections. In the footnote of table 9, the Nastran-generated beam-center deflection $r_n^{(N)} = (3.88473 \times 10^{-3},\ 3.87851 \times 10^{-3})$ in. (Appendix F) based on the two domain densities $(n = 20, n = 10)$ are shown for comparisons. Note that the two Nastran-generated beam-center deflections are extremely close with an infinitesimal difference of only 0.1637 percent.

Deflection Curves Comparisons

Figures 28a and 28b show the theoretical deflection curves of the two-end fixed curved beam $(\phi_n = 45°)$ calculated respectively from equations (17) and (33) compared with the associated Nastran-generated deflection curves (Appendix F) based on the domain density $n = 10$ (table 9). The good

agreement indicates that by using the domain density $n = 10$, the shape predictions can still be sufficiently accurate.

Figures 29a and 29b compare the theoretical deflection curves of the two-end fixed curved beam $(\phi_n = 45°)$ calculated respectively from equations (17) and (33) based on the two domain densities $(n = 20,\ n = 10)$ (table 9). The Nastran-generated deflection curves shown in figures 29a and 29b are for domain density $n = 20$ (Appendix F). Note from figures 29a and 29b that the theoretical deflection curves based on $n = 10$ are practically coincidental with the theoretical deflection curves based on $n = 20$, and the Nastran-generated deflection curve. However, near the two support regions, the difference between the two theoretical deflection curves of $(n = 20,\ n = 10)$ is slightly visible.

Beam-Center Prediction Error Comparisons

The beam center deflection data listed in table 9 were used to compare the beam-center prediction errors based on the two domain densities $(n = 20,\ n = 10)$. Table 10 shows the beam-center deflection prediction errors for the two-end fixed curved beam $(\phi_n = 45°)$ based on the two domain densities $(n = 20,\ n = 10)$.

Table 10. Beam-center deflection prediction errors for the two-end fixed curved beam $(\phi_n = 45°)$ based on two domain densities $(n = 20,\ n = 10)$ and a central load of $P = 100$ lb.

n (Domain density)	$r_{n/2}^{(N)}, \times 10^{-3}$ in. (Nastran deflections)	$r_{n/2}^{B}, \times 10^{-3}$ in. [Predicted, eq. (17)]	Percent error (No corrections)	$\hat{\eta}_{n/2}$ (Correction factor)	$(\hat{\eta}_{n/2} \cdot r_{n/2}^{B})$, $\times 10^{-3}$ in. (Corrected deflection)	Percent error (With corrections)
20	3.88487	3.83972	1.1622	1.01300	3.88964	0.1228
10	3.87851	3.83572	1.1033	1.01300	3.88559	0.1825

Note from table 10 that the beam-center deflections $r_{n/2}^{B}$ calculated from equations (17) and the corrected deflections $(\hat{\eta}_{n/2} \cdot r_{n/2}^{B})$ based on the two domain densities $(n = 20,\ n = 10)$ are extremely close. The beam-center prediction errors are in the negligible ranges of (1.1622–0.1228) percent and (1.1033–0.1825) percent respectively for $n = 20$ and $n = 10$ cases. The current finding indicates that using less domain density $n = 10$ (less number of strain sensors) is adequate for the shape predictions of current curved-beam geometry. The insensibility of the shape prediction accuracies on the domain density n was also found earlier for the straight beam cases $(\phi_n = 0°)$ (ref. 1).

It is important to mention that if the domain density n is further decreased from $n = 10$, one can expect that the theoretical deflections will be different, and thereby, the prediction errors can increase in view of figure 30, the prediction error curve established by Lung and Ko (fig. 13 of ref. 11) for GIII swept wings (fig. 1b).

Alternative Formulation

The formulations of the Curvilinear Displacement Transfer Functions presented above are based on the relative slope angle $\alpha(\equiv \theta - \theta_0)$ (called α-formulation), which is in reference to the curved *s*-axis of the undeformed curved beam. Alternatively, one can also formulate the Curvilinear Displacement Transfer Functions using the absolute slope angle θ (called θ-formulation), which is in reference to the

x-axis (fig. 31). The θ-formulation is presented in Appendix H for reference. It is important to mention that for a given set of surface strains, both formulations give identical strain-induced deflections (measured from an undeformed configuration) of the cantilever curved beams.

Concluding Remarks

The Curvilinear Displacement Transfer Functions for embedded curved beams were formulated by piecewise integrations of the curvature-strain differential equation. The formulation is based on a true displacement (curvilinear distance traced by a material point from its initial undeformed position to its final deformed position).

The shape prediction analysis was performed on curved beams (cantilever and two-end supported) with different curvatures up to a semicircle. Nastran analysis was performed on the curved beams to analytically generate surface strains for inputs to the Curvilinear Displacement Transfer Functions for deflection calculations. The Nastran-generated deflections were then used as reference yardsticks for studying the shape prediction accuracies of the Curvilinear Displacement Transfer Functions. Some key highlights of the results are included in the following list.

1. Using the Displacement Transfer Functions for transforming surface strains into deflections for structure deformed shape predictions, there is no need to know material properties, nor the complex geometries of the internal structures, and the traditional complex finite-element modeling for deflection calculations is eliminated.
2. The Curvilinear Displacement Transfer Functions can be formulated in reference to the curved *s*-axis of the undeformed curved beam (α-formulation), or in reference to horizontal *x*-axis (θ-formulation).
3. Shape prediction accuracy is insensitive to the change of domain density *n* (strain-sensor separation distance). For the current curved-beam geometries, the differences in shape prediction accuracy based on domain densities $(n = 20,\ n = 10)$ are in the negligible range of (0.02010–0.2760) percent.
4. For the cantilever curved beams, both α-formulation and θ-formulation give identical theoretical strain-induced deflections for a given set of surface strains.
5. The Curvilinear Displacement Transfer Functions are extremely accurate for the shape predictions of straight cantilever beams (limit case, $\phi_n = 0°$) with infinitesimal error of merely 0.0192 percent. However, the prediction error increased with increasing curved-beam angle ϕ_n, and reached a maximum error of 24.8524 percent at $\phi_n = 180°$.
6. With the introduction of curvature-effect correction factor expressed in simple mathematical functional forms, the prediction errors for the cantilever-curved beams $(\phi_n = 45° - 180°)$ can be reduced greatly from (2.1172–24.8524) percent error range down to (0.8072–3.8901) percent error range.
7. The Curvilinear Displacement Transfer Functions are also quite accurate for the shape predictions of the limit case of the two-end supported straight beams $(\phi_n = 0°)$ with a negligible error of 0.4145 percent and 0.1039 percent, respectively for the two-end fixed and two-end simply supported cases.
8. For the two-end supported curved beams $(\phi_n = 45° - 180°)$, the prediction error increased with increasing the curved-beam angle ϕ_n, and reached maximum errors of 20.4857 percent and 24.3129 percent at $\phi_n = 180°$, respectively for the two-end fixed and two-end simply supported cases.

9. With the introduction of the correction factor expressed in simple mathematical functional form, the prediction errors for the two-end supported curved beams $(\phi_n = 45° - 180°)$ could be reduced greatly from (1.1622–20.4857) percent error range down to (0.1228–2.8028) percent for the two-end fixed cases; and from (1.7444–24.3129) percent error range down to (0.4670–5.1406) percent error range for the two-end simply supported cases.
10. Using domain densities of $n = 10$ or $n = 20$, the Curvilinear Displacement Transfer Functions can calculate quite accurate deformed shapes of the curved beams, and there is no need to use an excessively large number of strain-sensing stations. However, if the domain density n is further decreased from $n = 10$, the prediction errors can increase.

Figures

ED07-0186-01

Figure 1a. Ikhana unmanned aircraft (66-ft wingspan) (ref. 10).

ED12-0191-47

Figure 1b. GIII swept-wing aircraft (77.83-ft wingspan) (ref. 11).

Figure 1. Shape prediction accuracies of earlier Displacement Transfer Functions (refs. 1–9) were validated by using Ikhana and GIII aircraft wings subjected to combined bending and torsion (ref. 11).

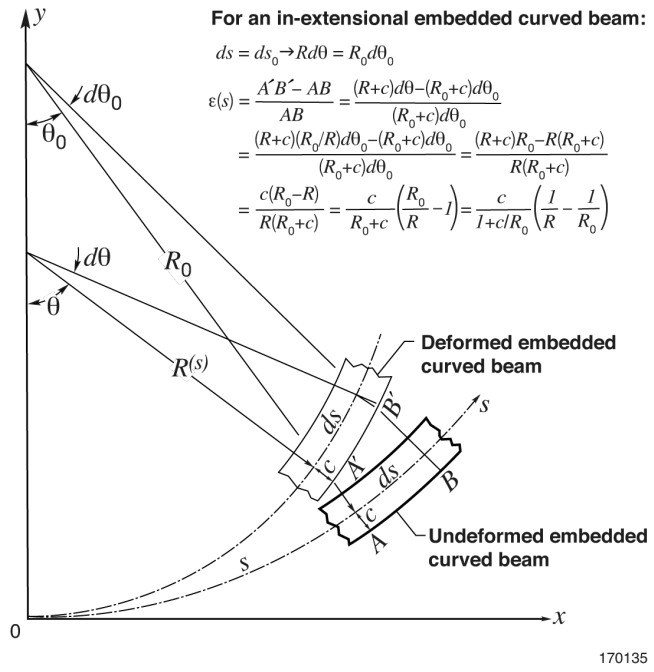

Figure 2. Small segment of a deformed in-extensional embedded curved beam for geometrically relating deformed and undeformed radii of curvature $\{R(s), R_0\}$ to the outer surface bending strain $\varepsilon(s)$.

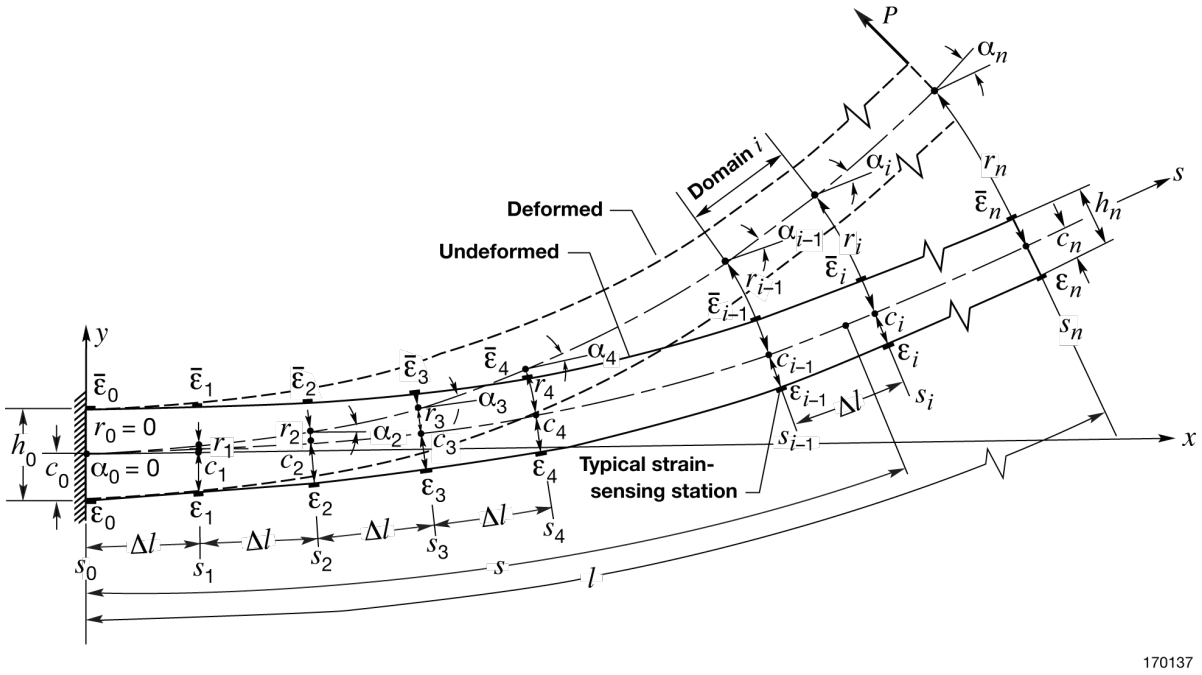

Figure 3. A discretized embedded cantilever curved beam (depthwise cross section along strain-sensing lines) with strain-sensing stations evenly distributed along outer (lower) and inner (upper) strain-sensing lines.

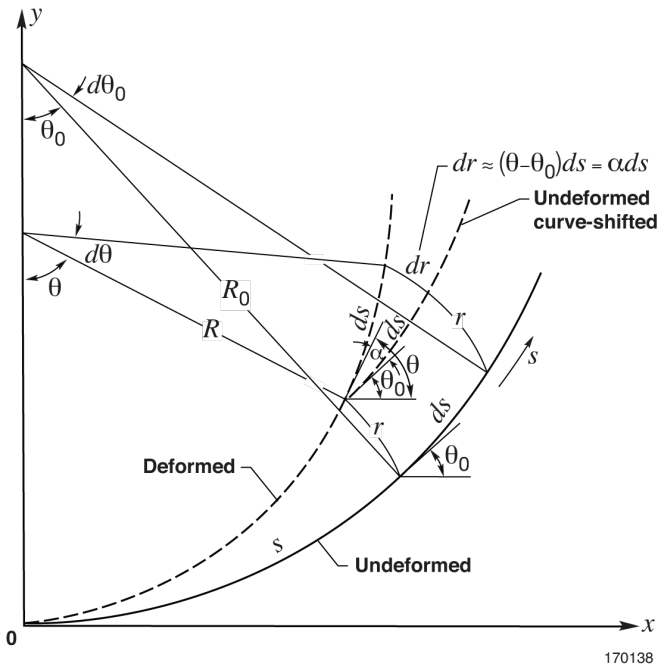

Figure 4. Small segment ds of undeformed and deformed embedded curved beam for geometrically relating curved deflection increment dr to slope angle α through $dr \approx (\theta - \theta_0)ds = \alpha ds$.

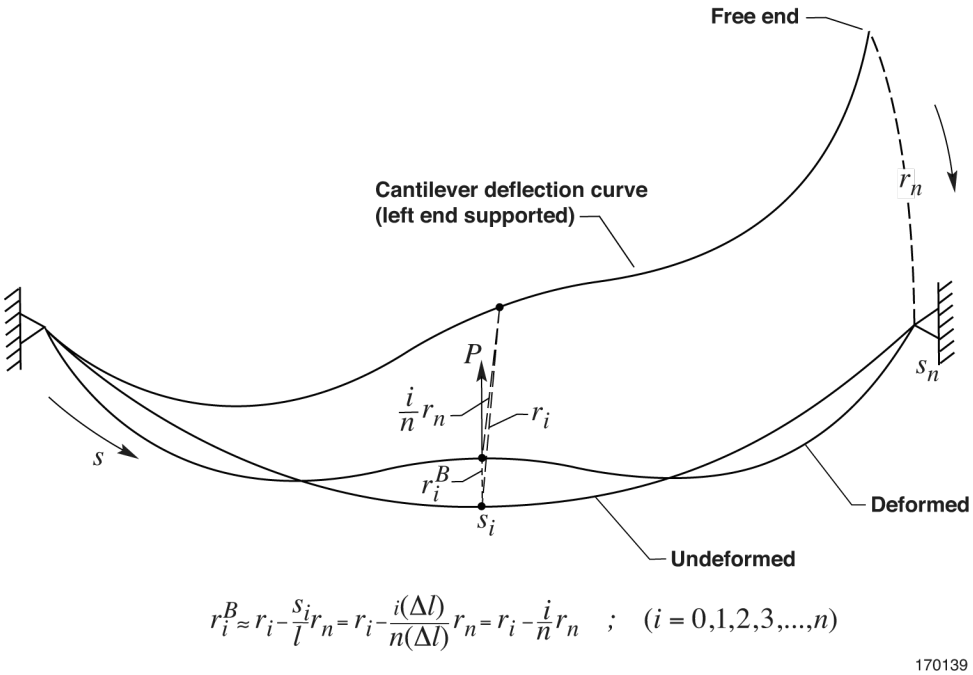

Figure 5. Deflection curve of the two-end supported curved beam generated by graphically rotating the cantilever deflection curve by nullifying the free-end deflection.

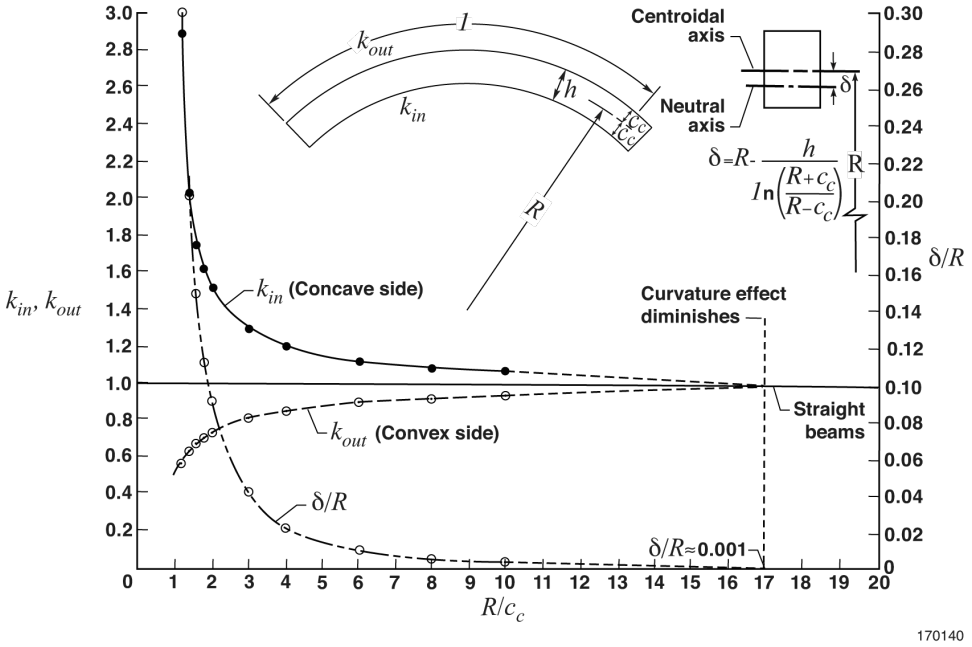

Figure 6. Plots of normalized bending stresses $\{k_{in}, k_{out}\}$ and normalized neutral-axis offset δ/R as functions of normalized radius of curvature R/c_c of curved beams.

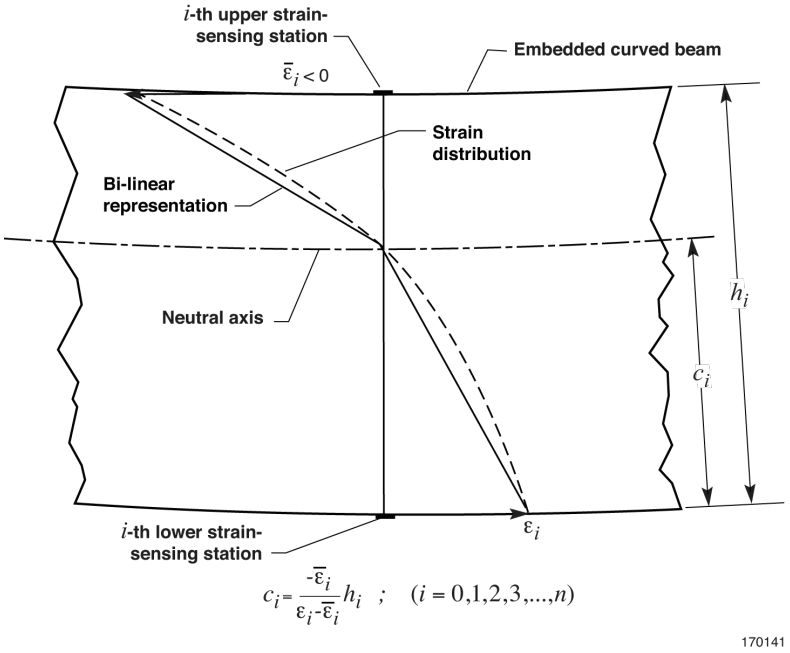

Figure 7a. Using outer and inner surface strains $\{\varepsilon_i, \bar{\varepsilon}_i\}$ to obtain depth factors c_i for a shallow curved beam.

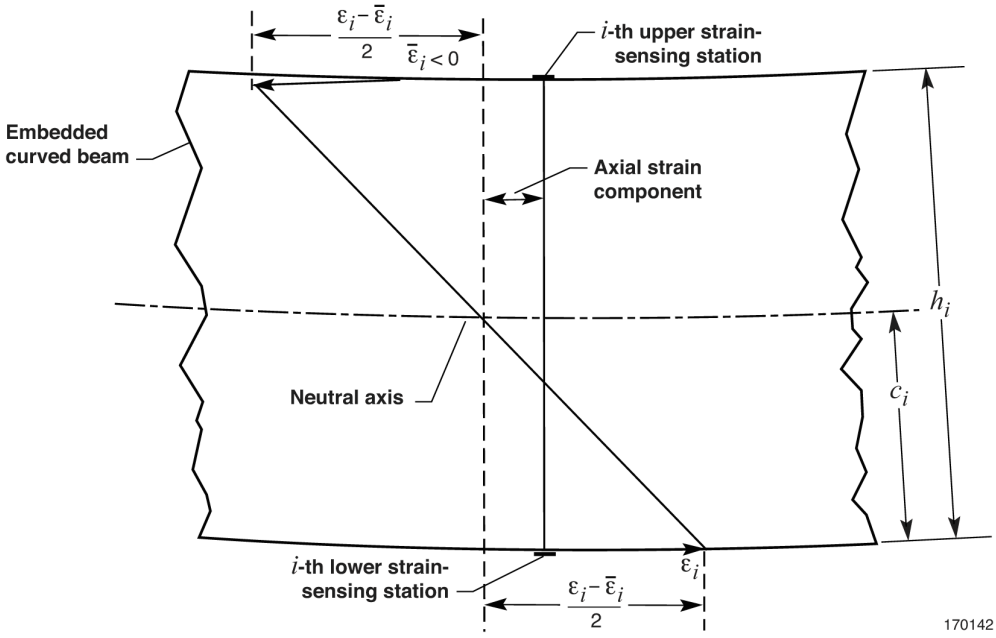

Figure 7b. Using outer and inner surface strains $\{\varepsilon_i, \bar{\varepsilon}_i\}$ to obtain true bending strains, $(\varepsilon_i - \bar{\varepsilon}_i)/2$ for a shallow curved beam using given depth factors $c_i = h_i/2$.

Figure 7. Using outer and inner surface strains to obtain depth factors or true bending strains for a shallow curved beam.

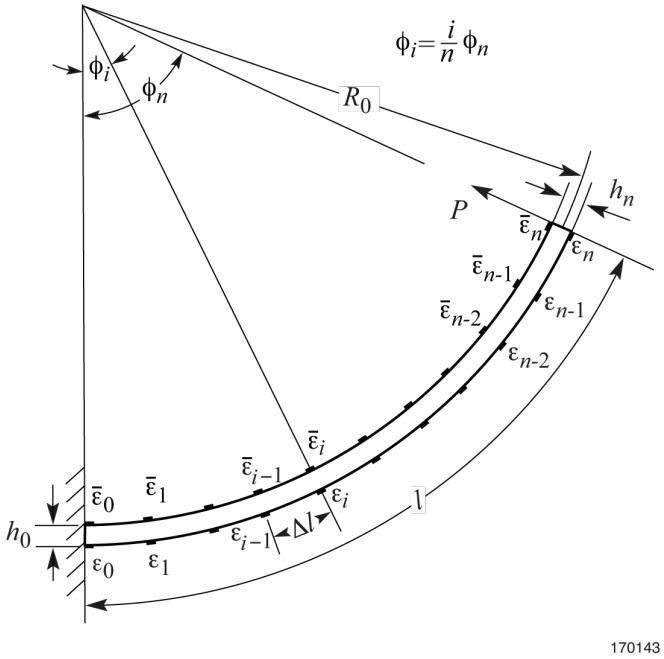

Figure 8a. Cantilever curved beam; uniform depth $(h_0 = h_n)$.

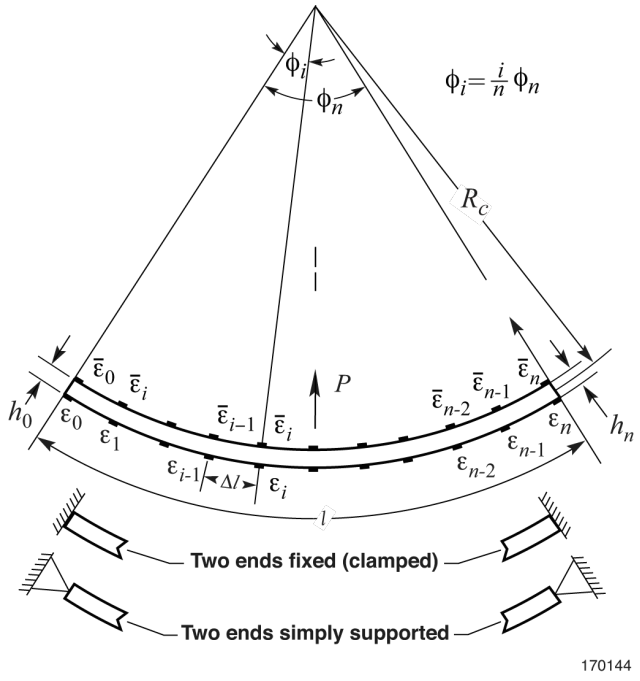

Figure 8b. Two-end supported curved beam; uniform depth $(h_0 = h_n)$.

Figure 8. Geometries of typical curved beams with different end-support conditions.

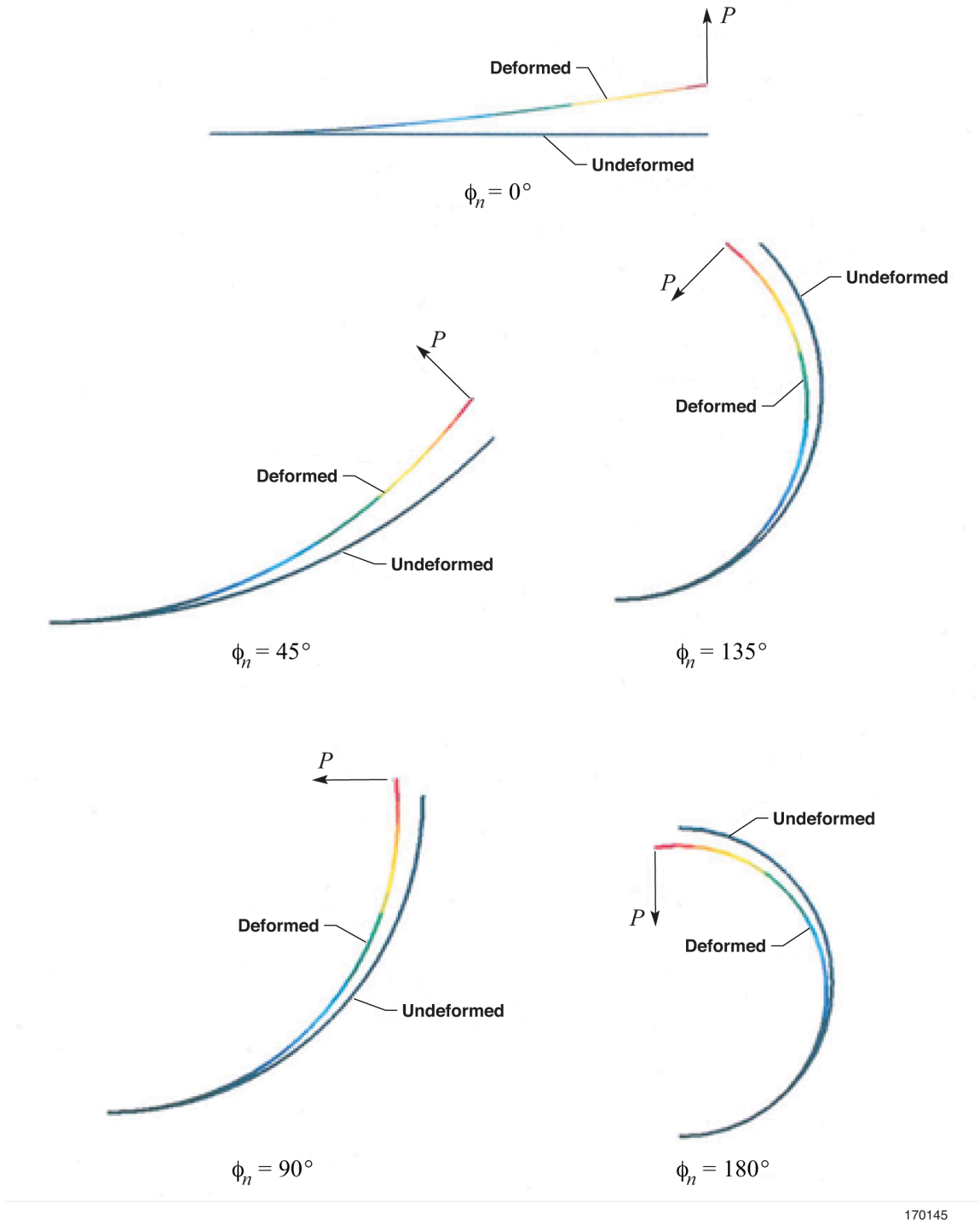

Figure 9. Nastran-generated undeformed and deformed shapes of cantilever curved beams with a different curved-beam angle ϕ_n subjected to a beam-tip radial load $P = 100$ lb, $l = 100$ in., and $h = w = 2$ in.

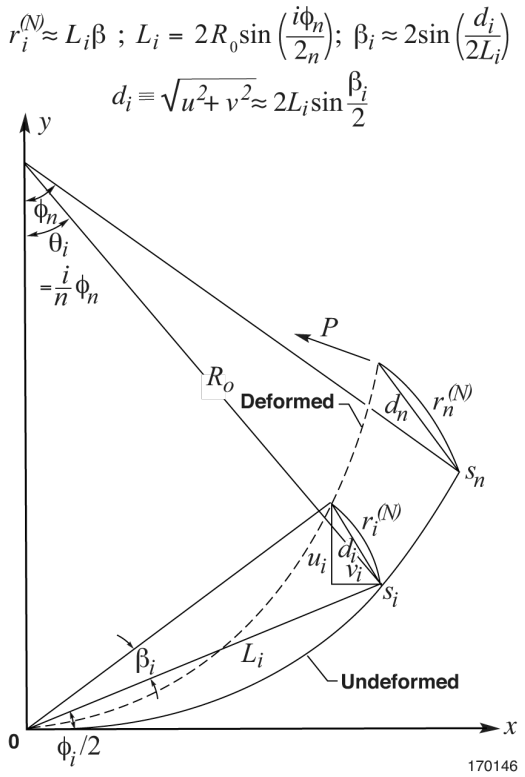

Figure 10. Graphical generation of Nastran curved deflection $r_i^{(N)}$ of point s_i using geometry of deformed and undeformed embedded cantilever curved beam.

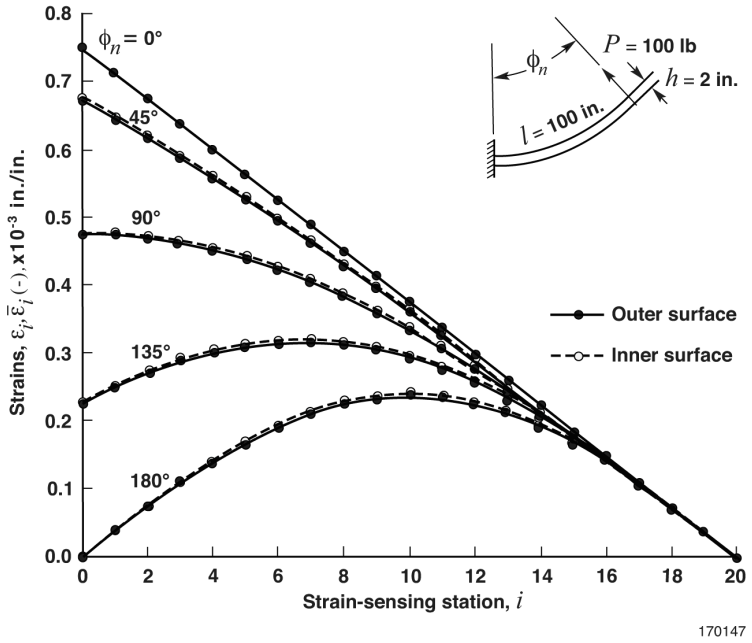

Figure 11. Nastran-generated surface strain curves for different cantilever curved beams; $P = 100$ lb and $n = 20$.

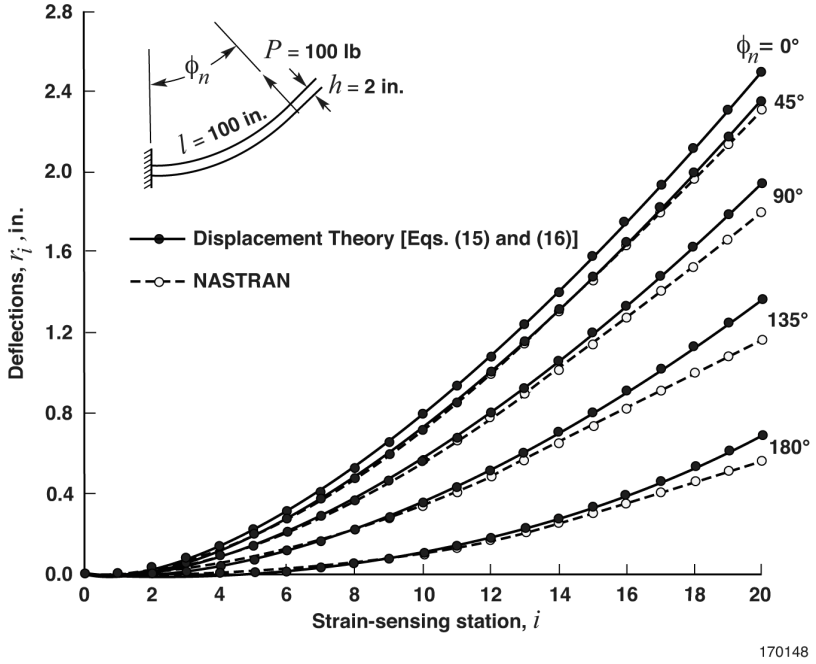

Figure 12. Deflection curves calculated from equations (15) and (16) compared with Nastran-generated deflection curves for different cantilever curved beams; $P = 100$ lb and $n = 20$.

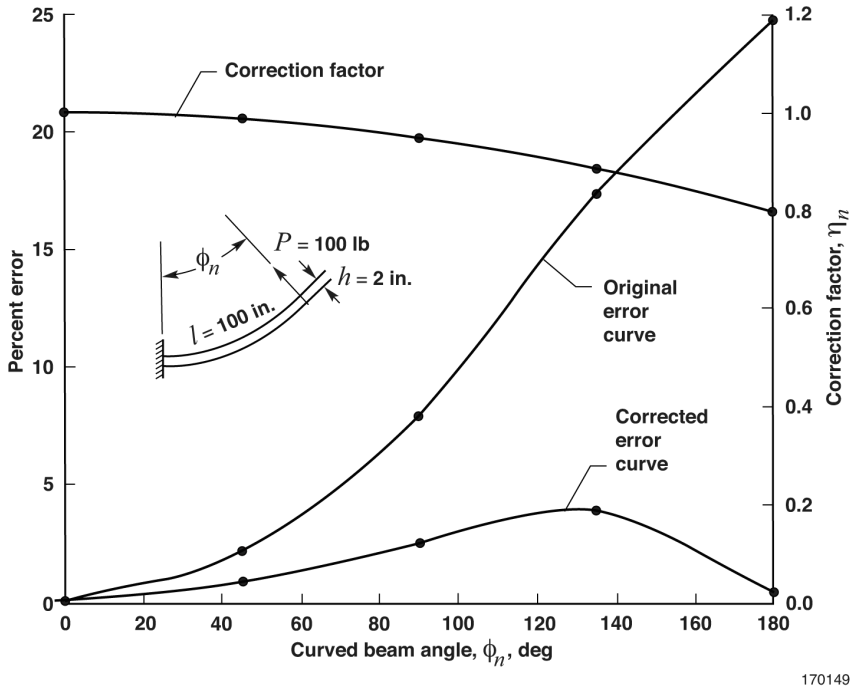

Figure 13. Comparison of original and corrected beam-tip prediction error curves for cantilever curved beams.

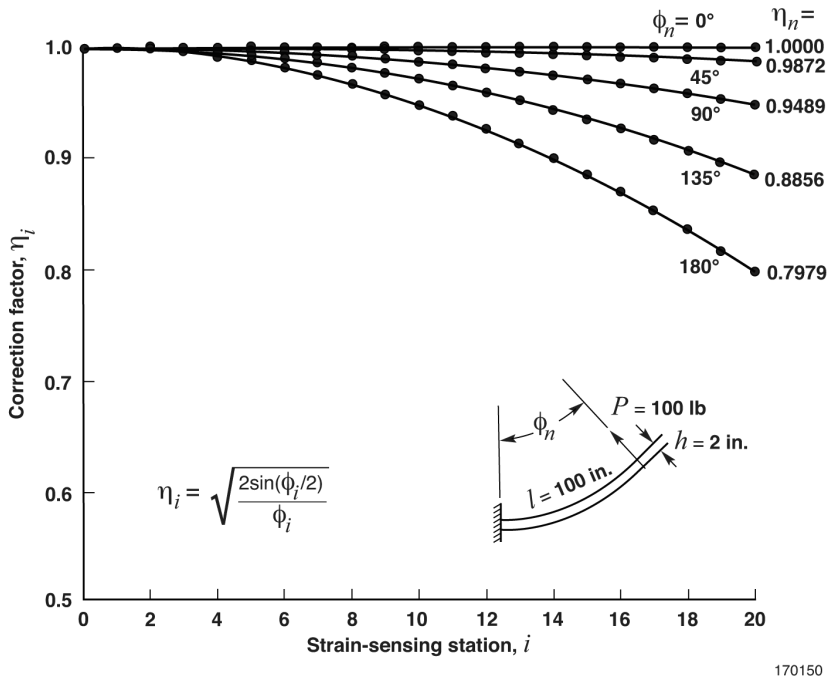

Figure 14. Variations of correction factors η_i along a span-wise direction for cantilever curved beams with different curved-beam angles $\phi_n (= 0° - 180°)$.

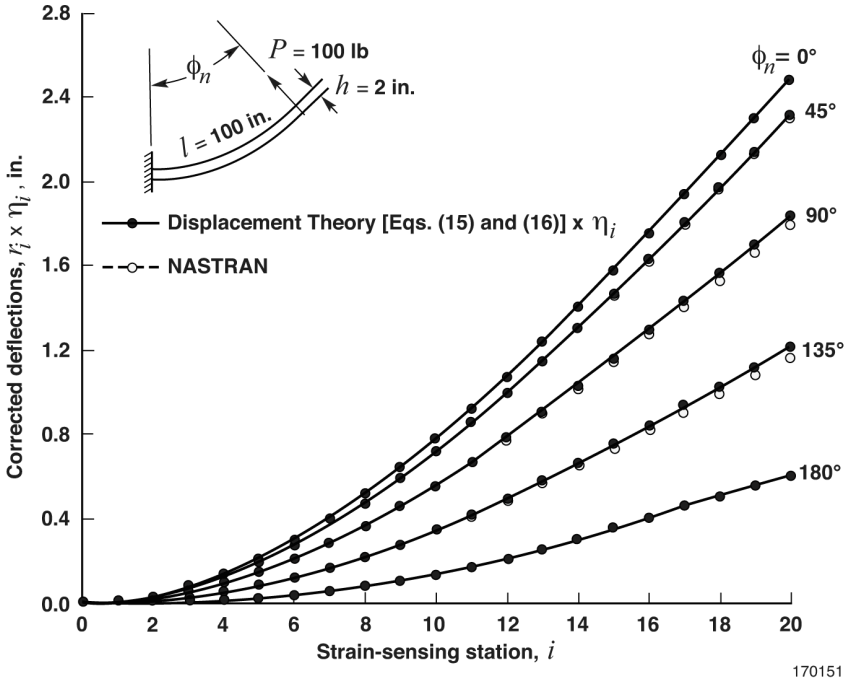

Figure 15. Corrected theoretical deflection curves compared with Nastran-generated deflection curves for different cantilever curved beams; $P = 100$ lb and $n = 20$.

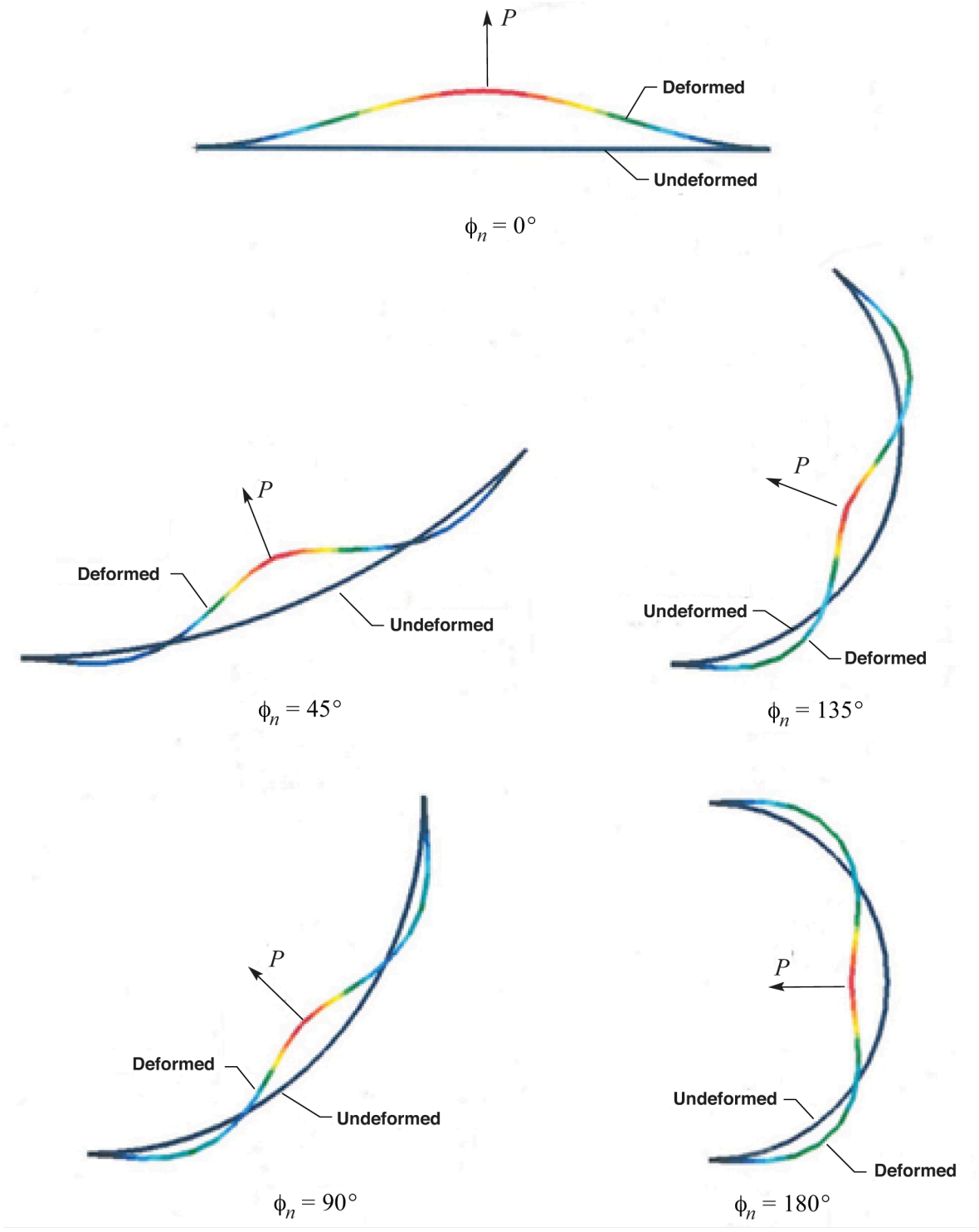

Figure 16. Nastran-generated undeformed and deformed shapes of two-end fixed curved beams with a different curved-beam angle ϕ_n subjected to a central load $P = 100$ lb, $l = 100$ in., and $h = w = 2$ in.

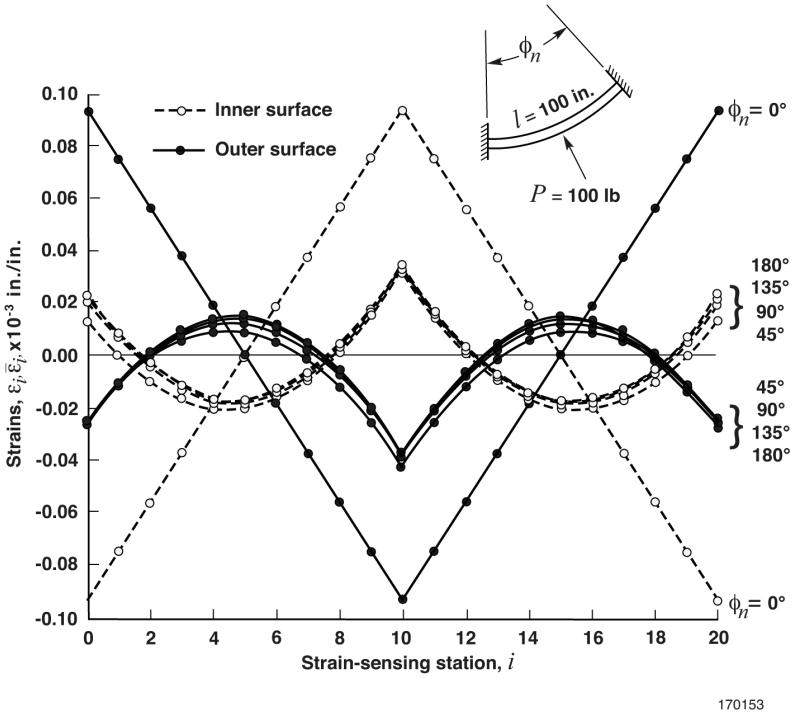

Figure 17. Nastran-generated surface strain curves for different two-end fixed curved beams; $P = 100$ lb at the curved-beam center and $n = 20$.

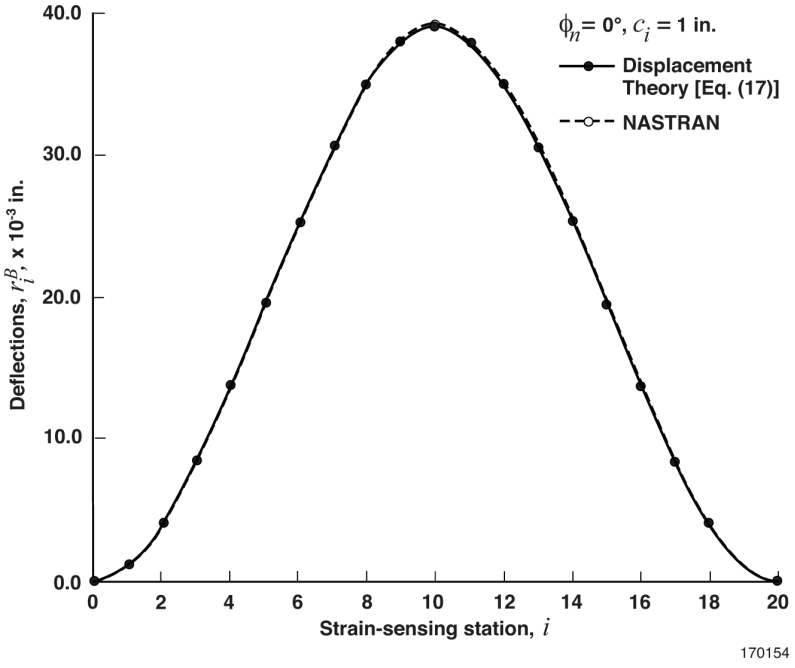

Figure 18a. $\phi_n = 0°$.

Figure 18. Theoretical deflection curves calculated from equation (17) compared with Nastran-generated deflection curves for different two-end fixed curved beams; $P = 100$ lb and $n = 20$.

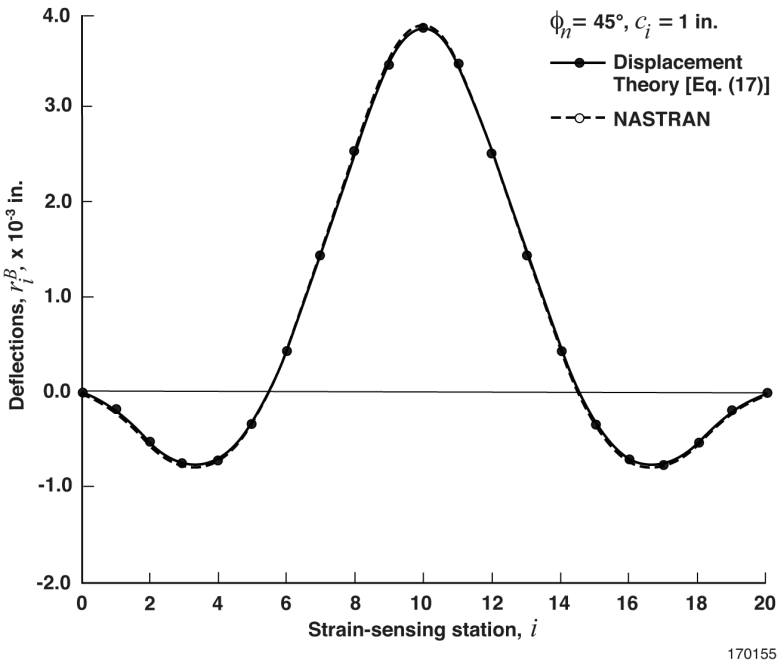

Figure 18b. $\phi_n = 45°$.

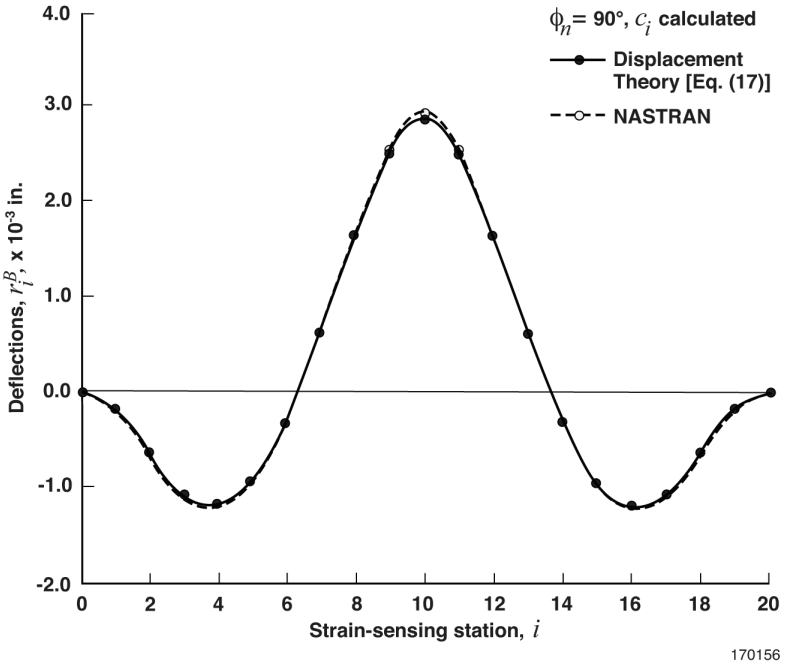

Figure 18c. $\phi_n = 90°$.

Figure 18. Continued.

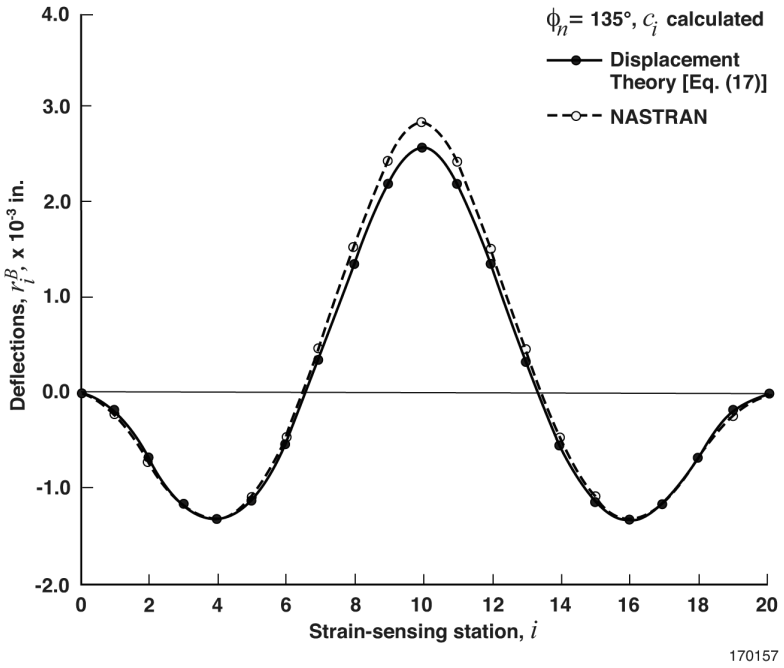

Figure 18d. $\phi_n = 135°$.

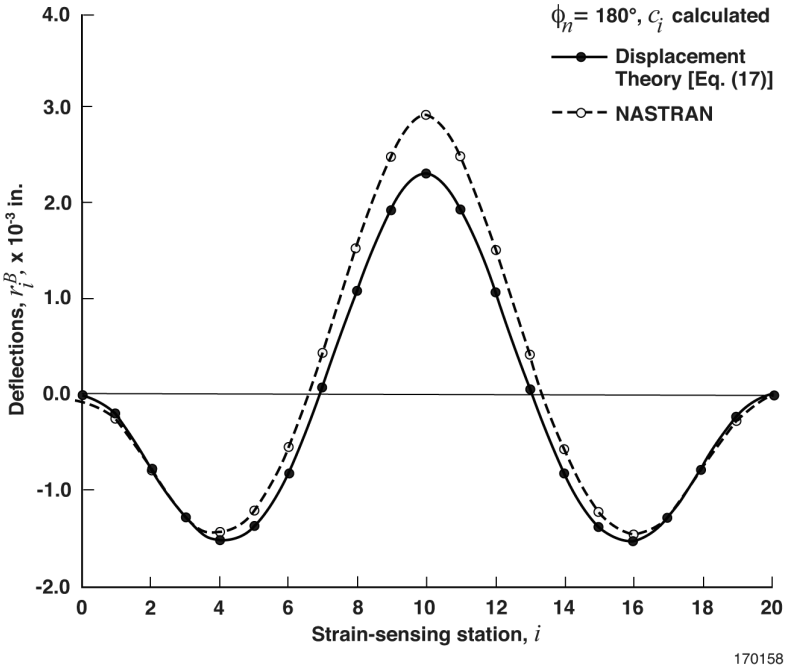

Figure 18e. $\phi_n = 180°$.

Figure 18. Concluded.

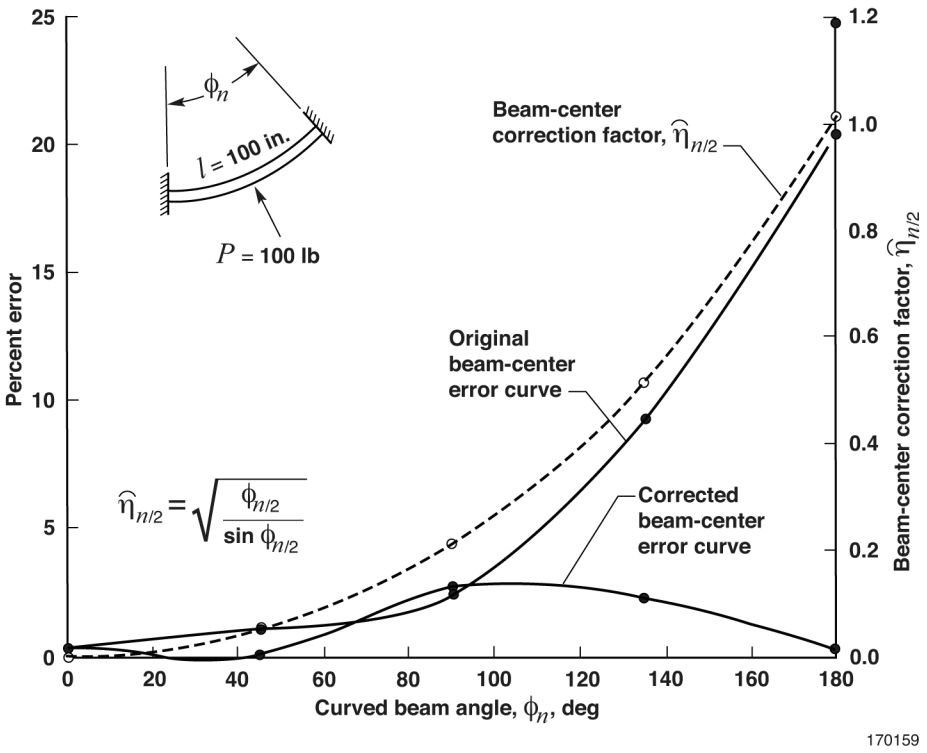

Figure 19. Comparison of original and corrected beam-center prediction error curves for two-end fixed curved beams.

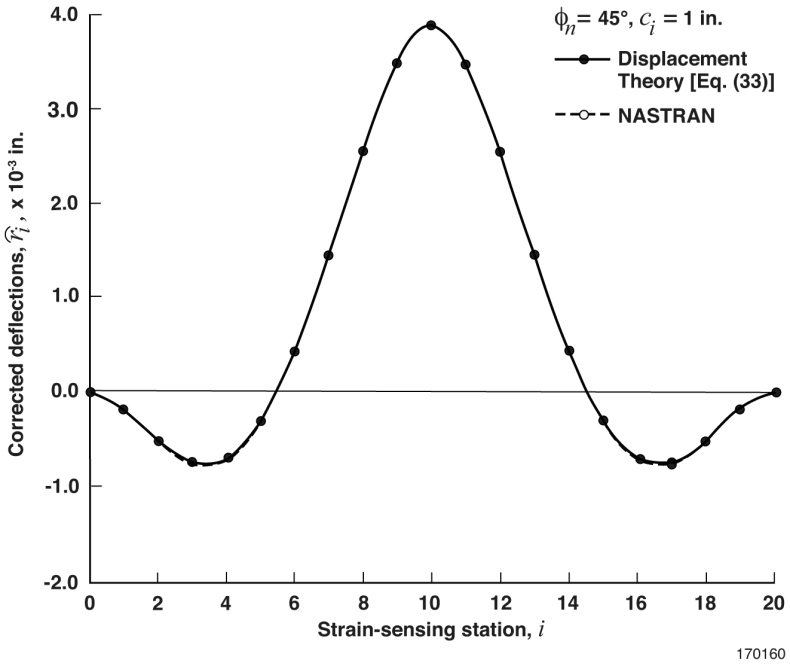

Figure 20a. $\phi_n = 45°$.

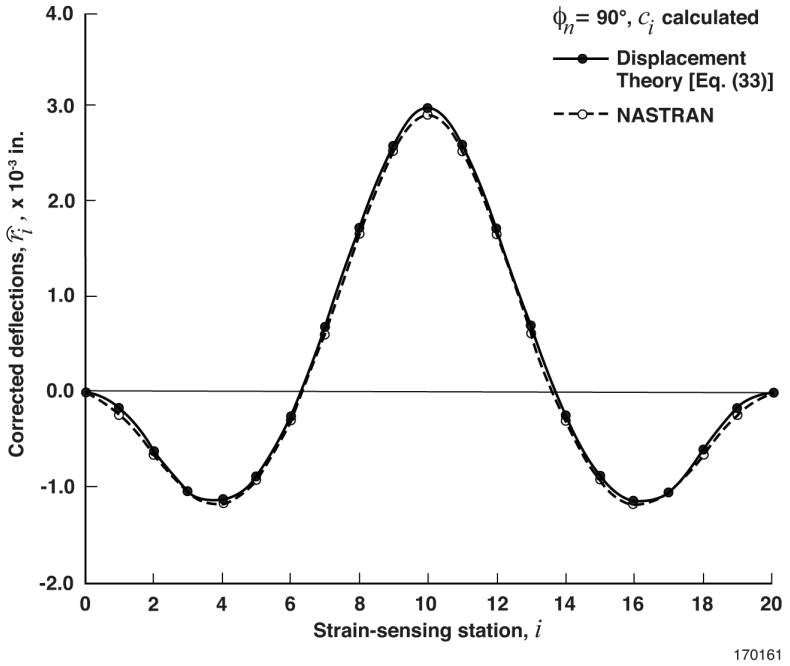

Figure 20b. $\phi_n = 90°$.

Figure 20. Corrected theoretical deflection curves calculated from equation (33) compared with Nastran-generated deflection curves for different two-end fixed curved beams; $P = 100$ lb and $n = 20$.

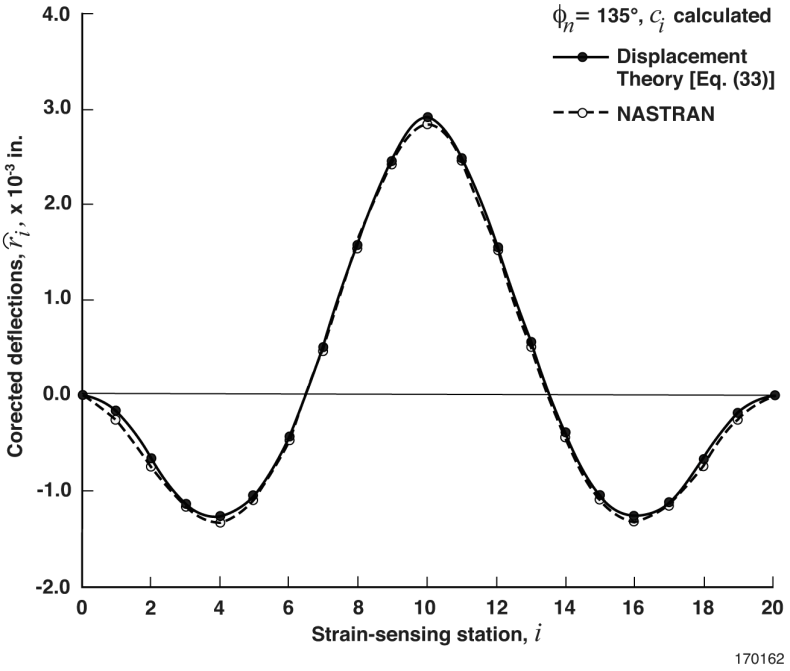

Figure 20c. $\phi_n = 135°$.

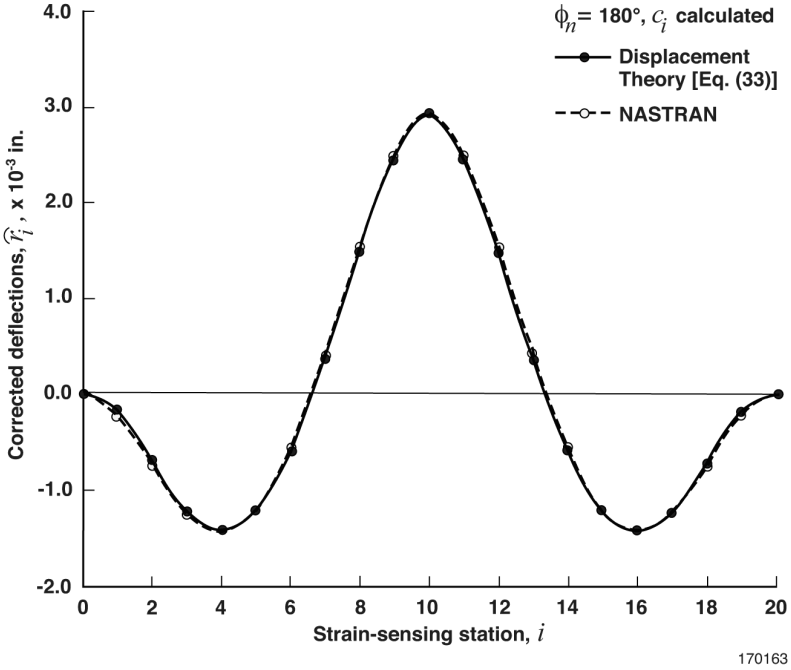

Figure 20d. $\phi_n = 180°$.

Figure 20. Concluded.

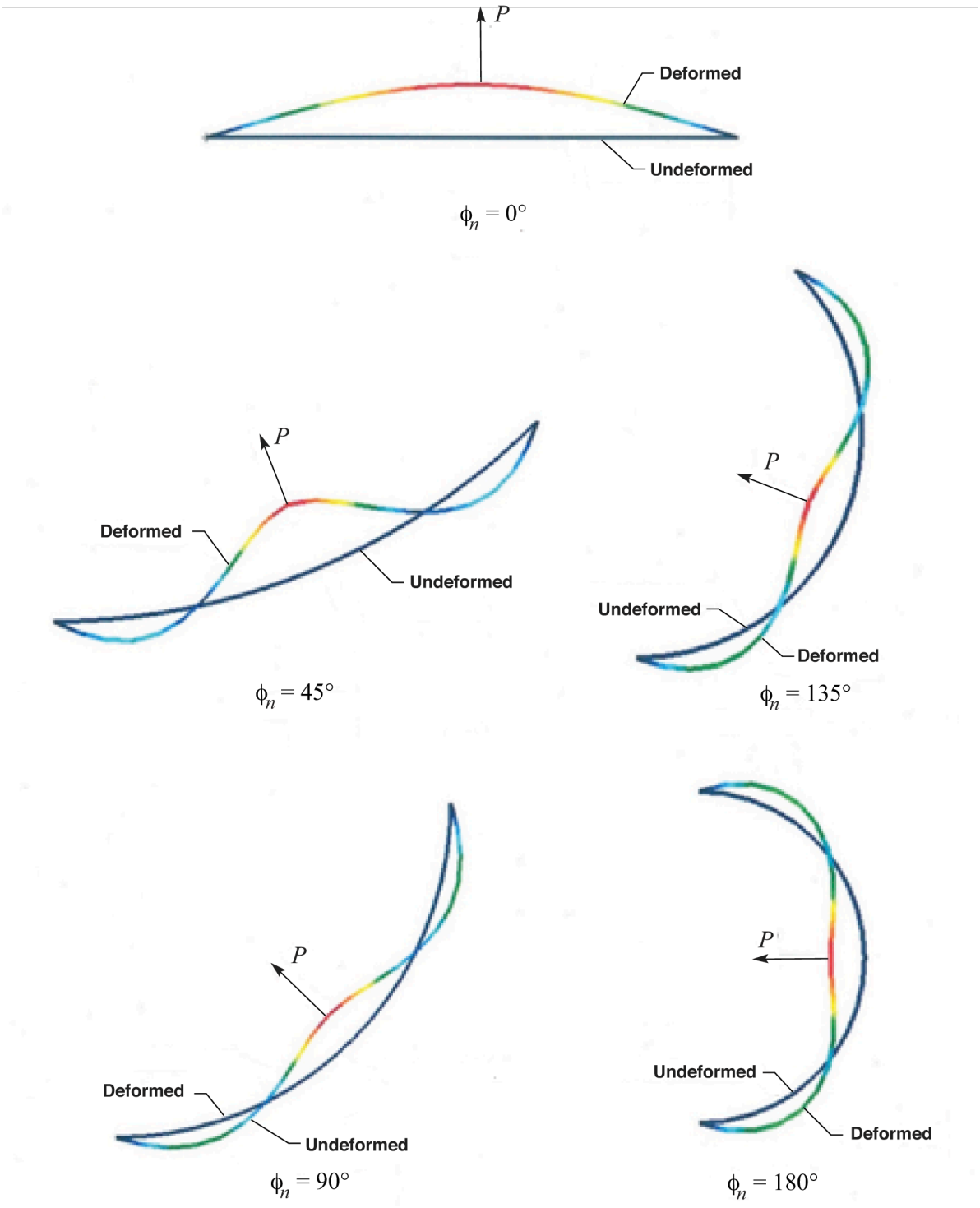

Figure 21. Nastran-generated undeformed and deformed shapes of two-end simply supported curved beams with different curved-beam angles ϕ_n subjected to a central load of $P = 100$ lb, $l = 100$ in., and $h = w = 2$ in.

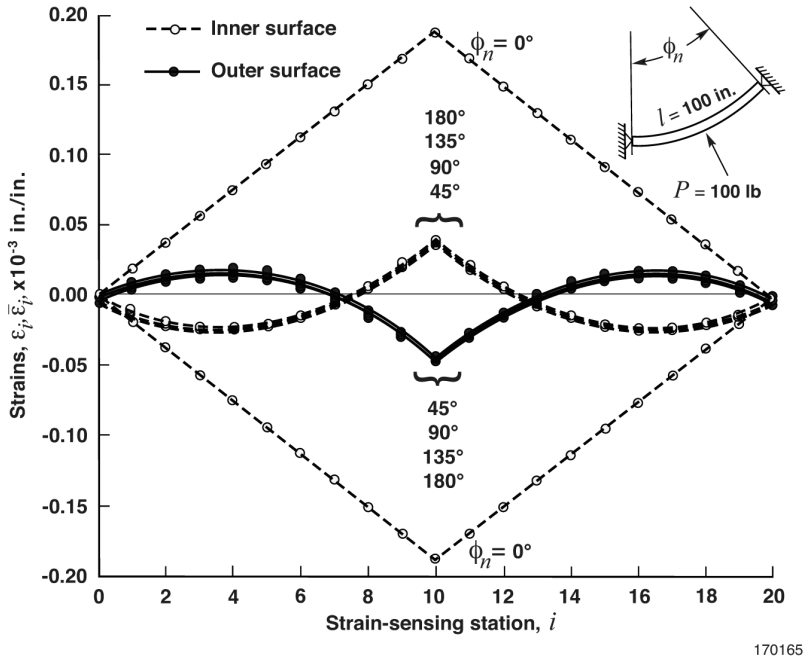

Figure 22. Nastran-generated surface strain curves for different two-end simply supported curved beams; $P = 100$ lb at a curved-beam center and $n = 20$.

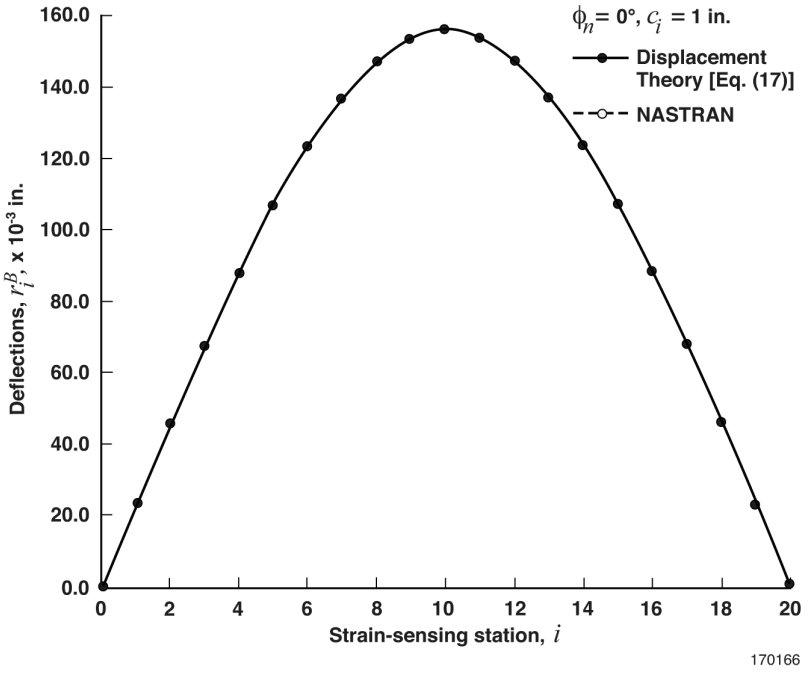

Figure 23a. $\phi_n = 0°$.

Figure 23. Theoretical deflection curves calculated from equation (17) compared with Nastran-generated deflection curves for different two-end simply supported curved beams; $P = 100$ lb and $n = 20$.

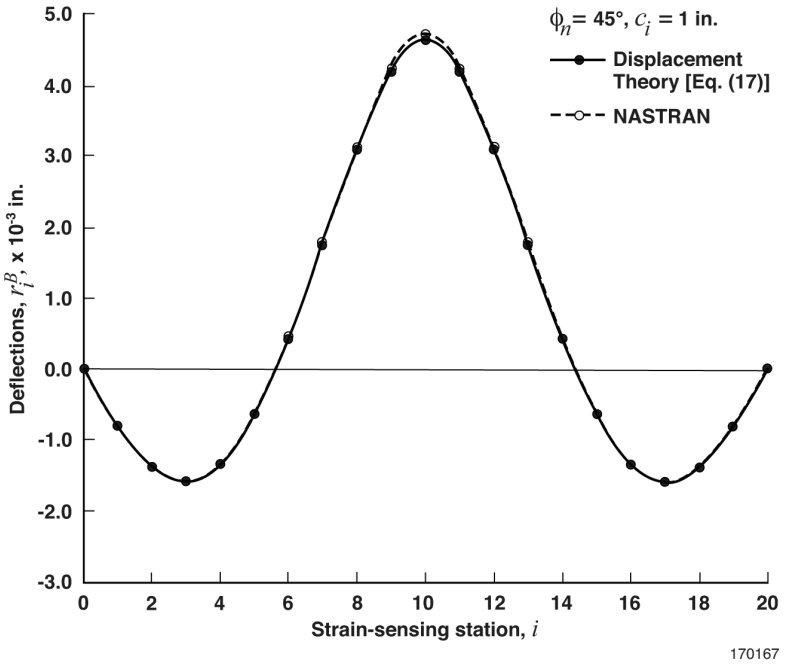

Figure 23b. $\phi_n = 45°$.

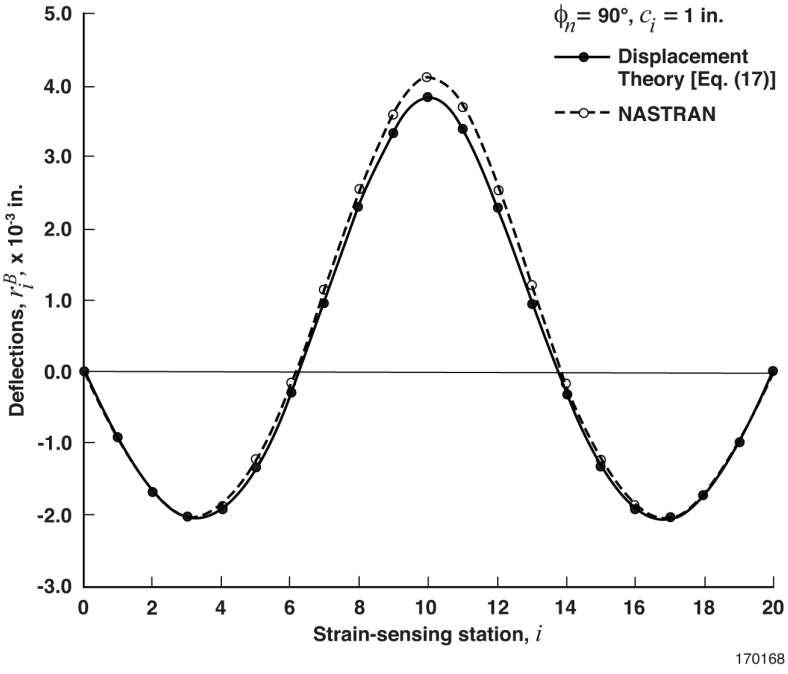

Figure 23c. $\phi_n = 90°$.

Figure 23. Continued.

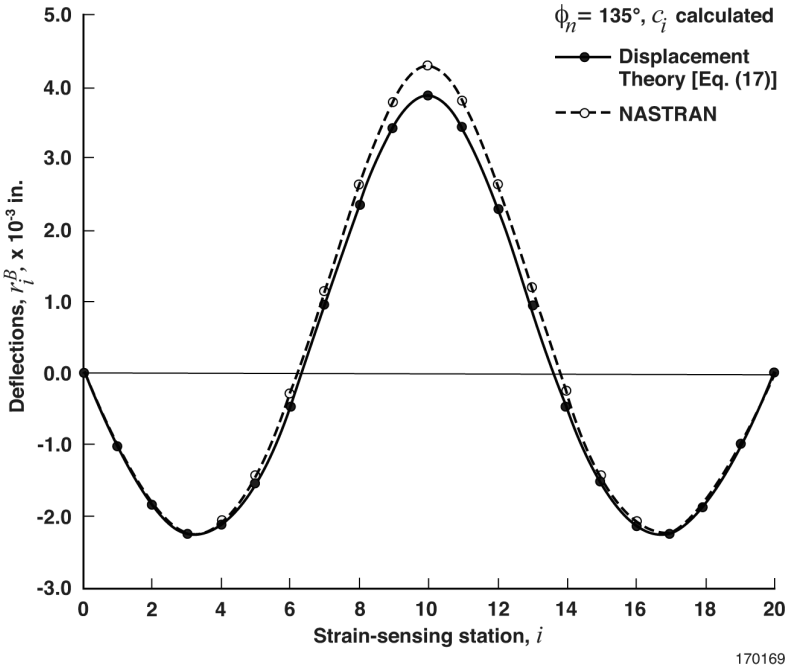

Figure 23d. $\phi_n = 135°$.

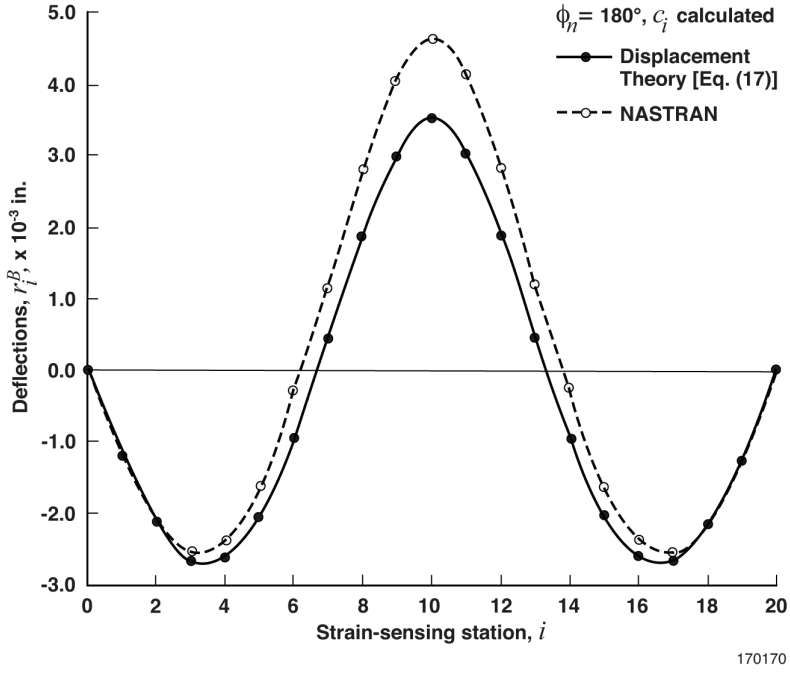

Figure 23e. $\phi_n = 180°$.

Figure 23. Concluded.

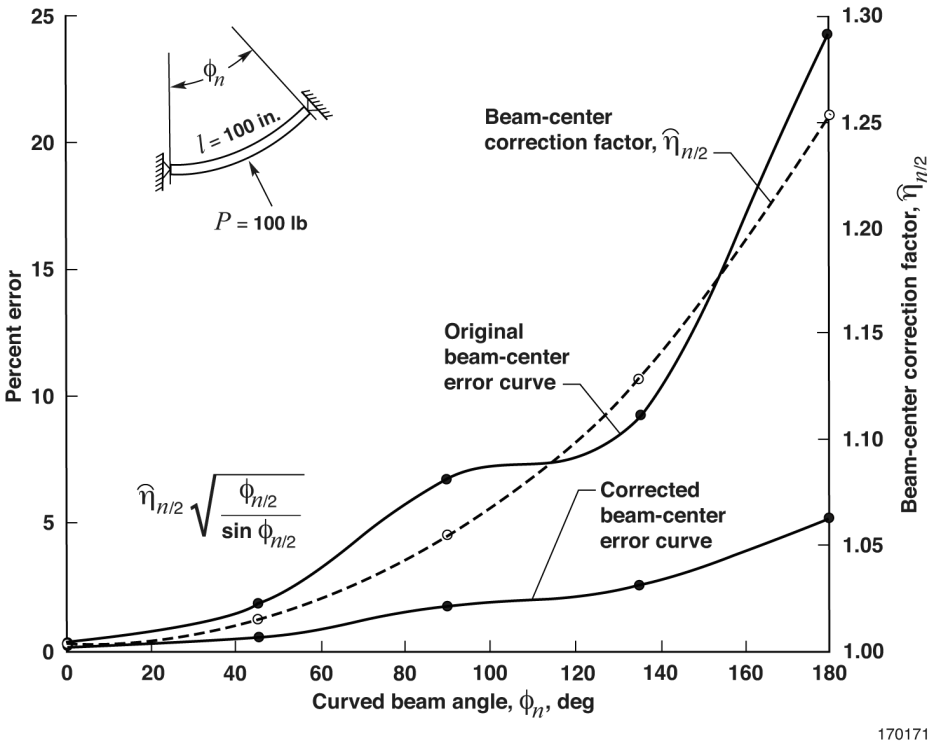

Figure 24. Comparison of original and corrected beam-center prediction error curves for two-end simply supported curved beams.

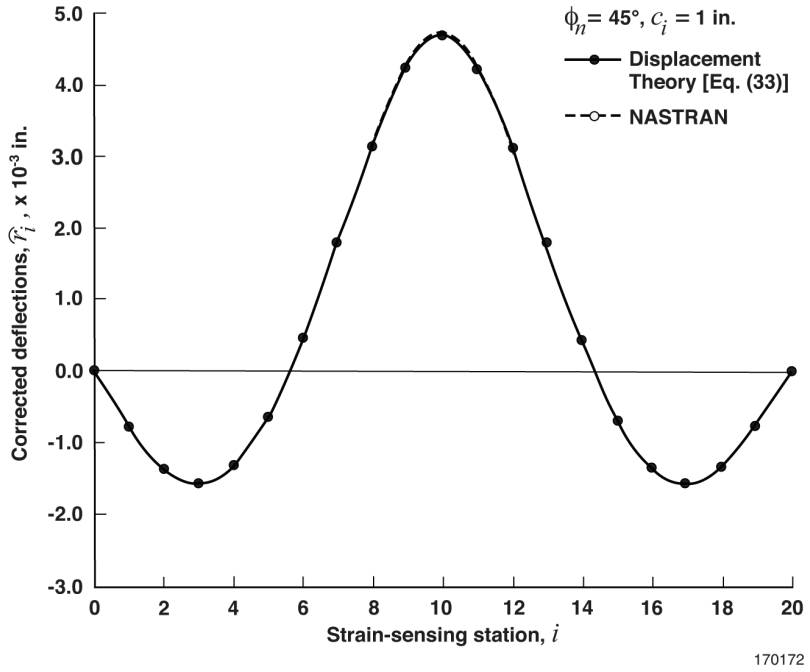

Figure 25a. $\phi_n = 45°$.

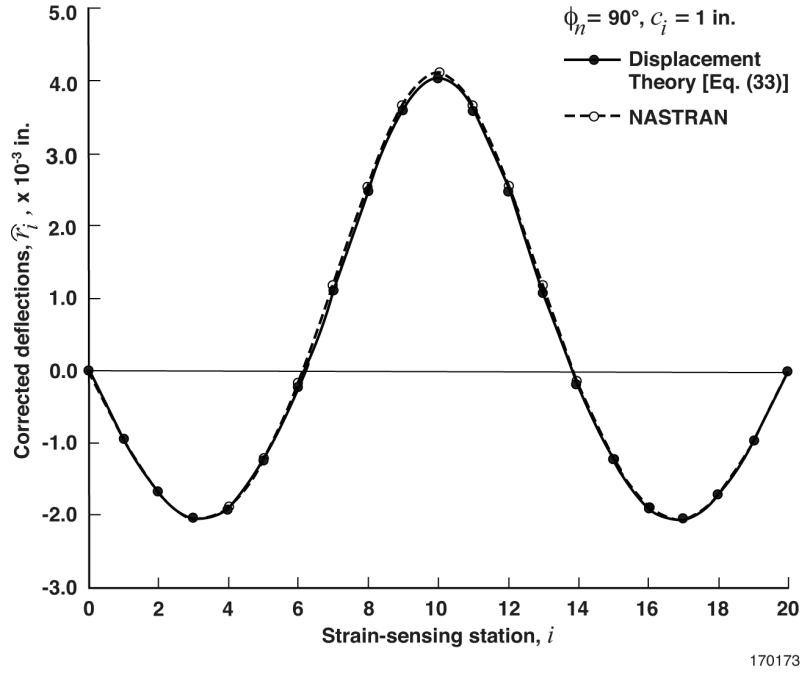

Figure 25b. $\phi_n = 90°$.

Figure 25. Corrected theoretical deflection curves calculated from equation (33) compared with Nastran-generated deflection curves for different two-end simply supported curved beams; $P = 100$ lb and $n = 20$.

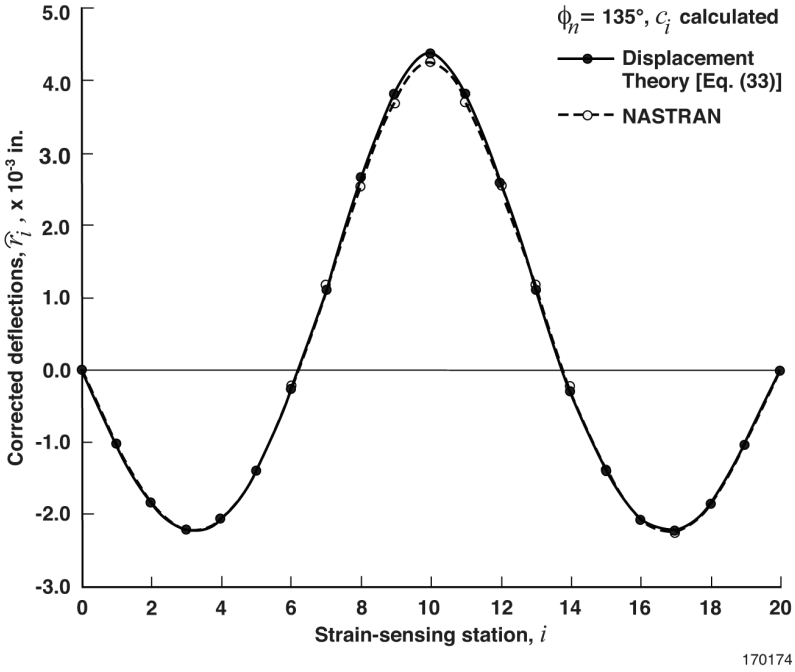

Figure 25c. $\phi_n = 135°$.

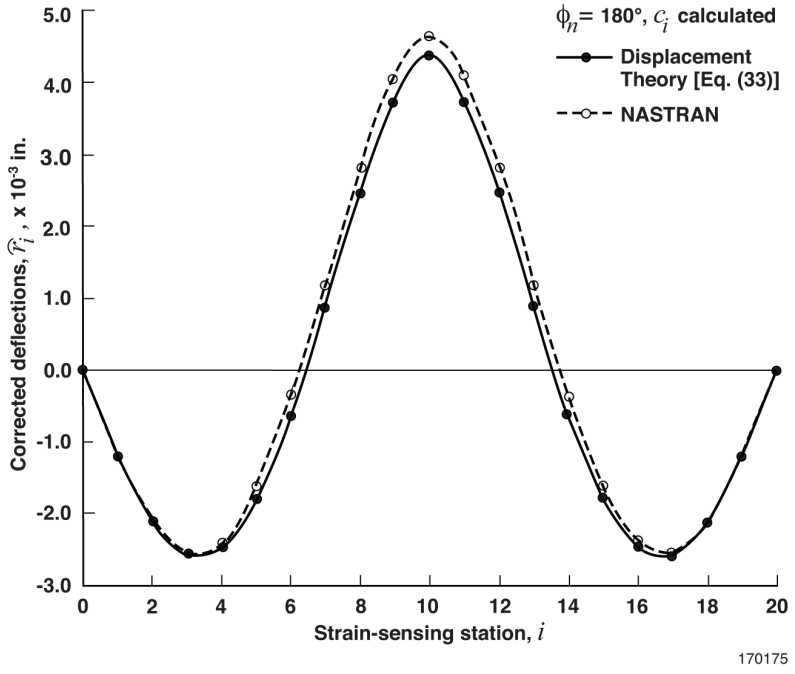

Figure 25d. $\phi_n = 180°$.

Figure 25. Concluded.

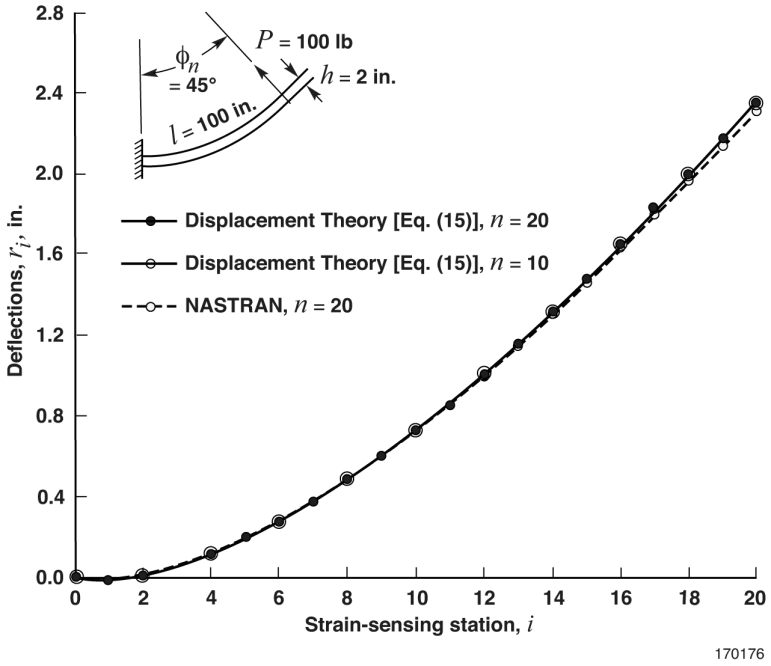

Figure 26a. Predicted deflections, eq. (15).

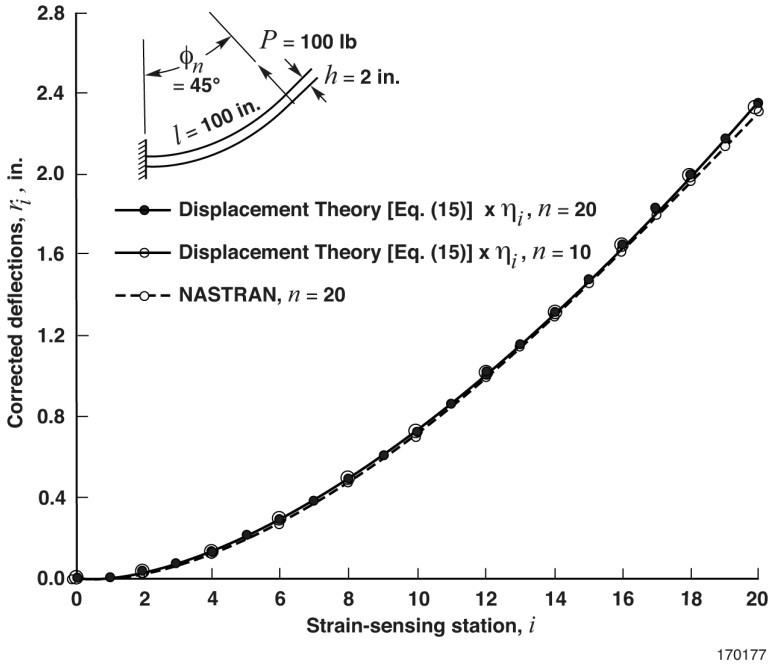

Figure 26b. Corrected deflections, eq. (15)$\times\eta_i$.

Figure 26. Comparisons of theoretical deflection curves $(n=20,\ n=10)$ and the Nastran deflection curve $(n=20)$ for the cantilever curved beam $(\phi_n=45°)$ under a beam-tip radial load of $P=100$ lb.

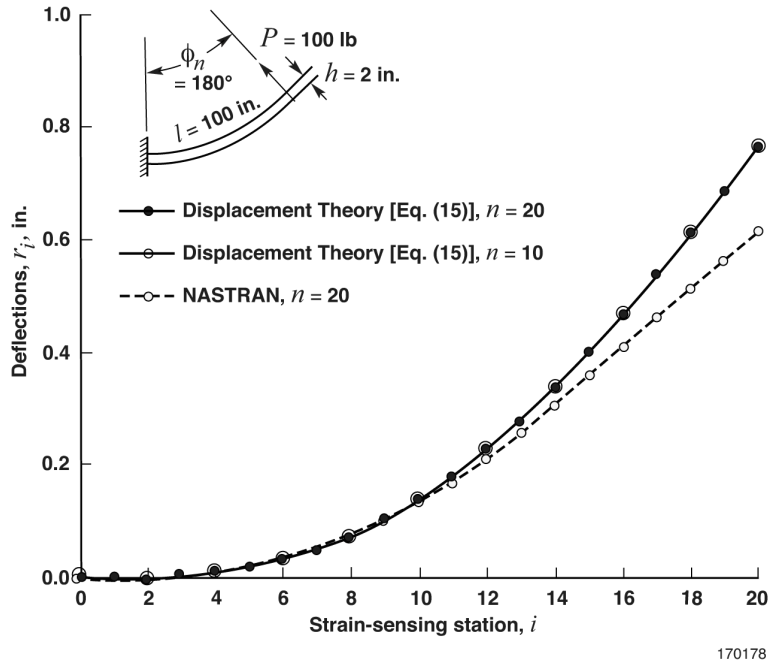

Figure 27a. Predicted deflections, eq. (15).

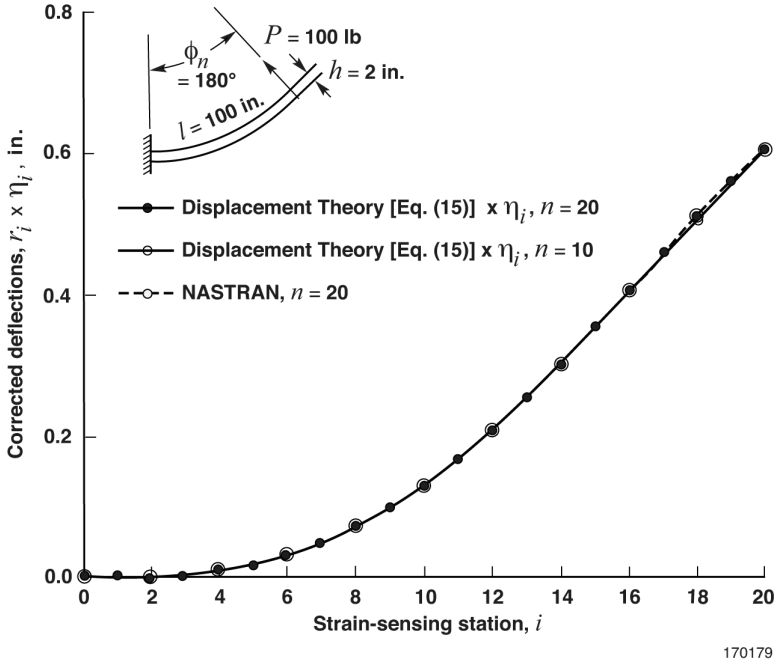

Figure 27b. Corrected deflections, eq. (15)$\times\eta_i$.

Figure 27. Comparisons of theoretical deflection curves $(n = 20,\ n = 10)$ and the Nastran deflection curve $(n = 20)$ for the cantilever curved beam $(\phi_n = 180°)$ under a beam-tip radial load of $P = 100$ lb.

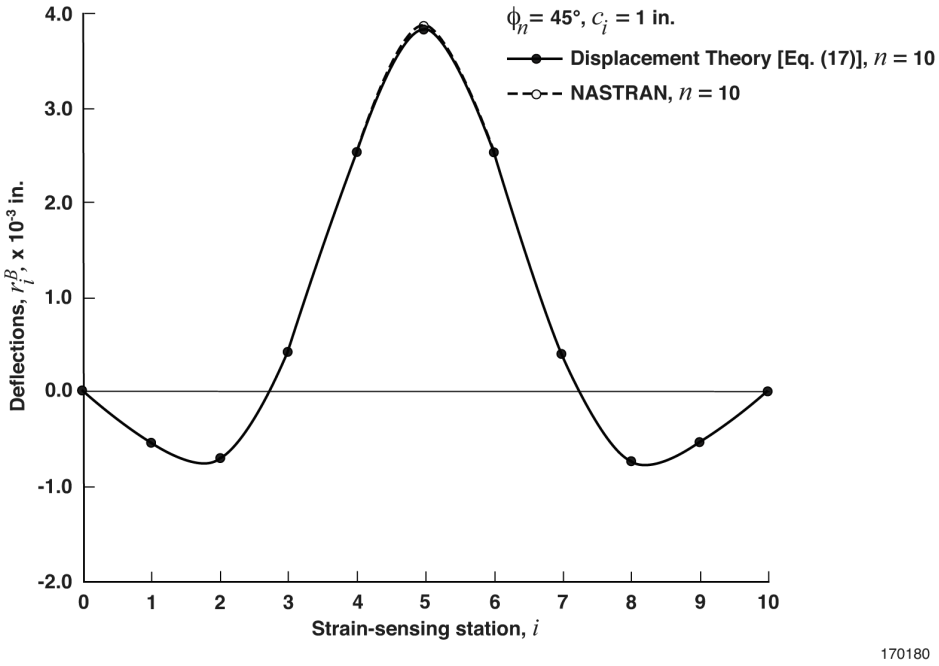

Figure 28a. Original, eq. (17).

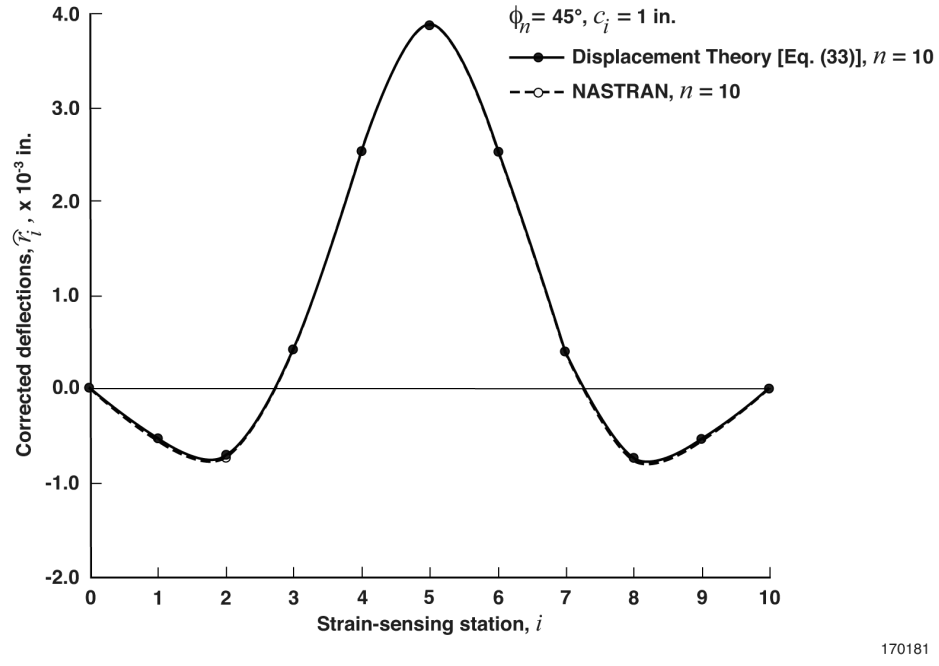

Figure 28b. Corrected, eq. (33).

Figure 28. Theoretical deflection curves calculated from equations (17) and (33) compared with Nastran-generated deflection curves based on a domain density $n = 10$ for the two-end fixed curved beam $(\phi_n = 45°)$ under a central load of $P = 100$ lb.

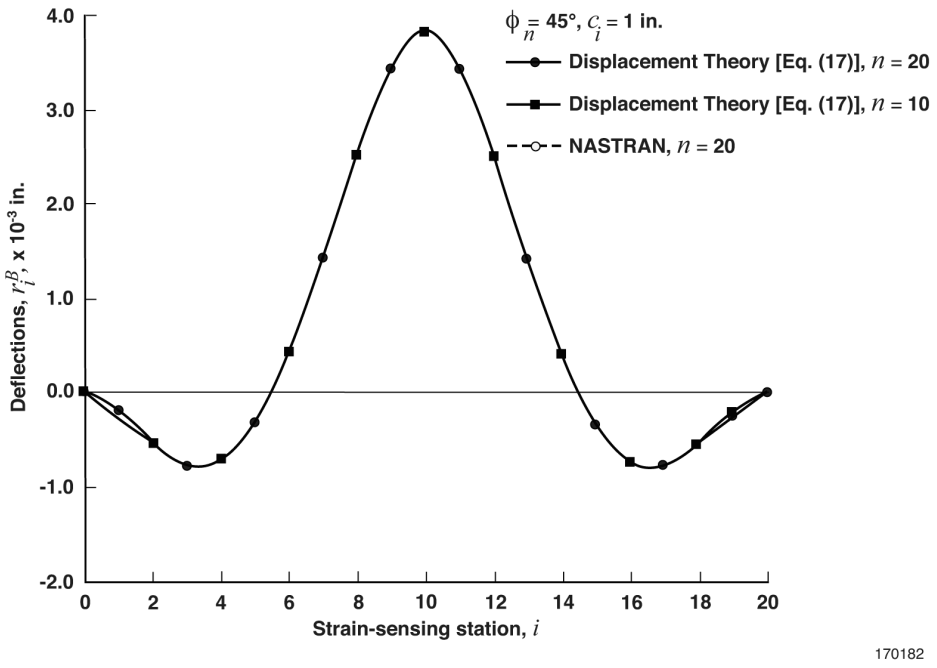

Figure 29a. Original, eq. (17).

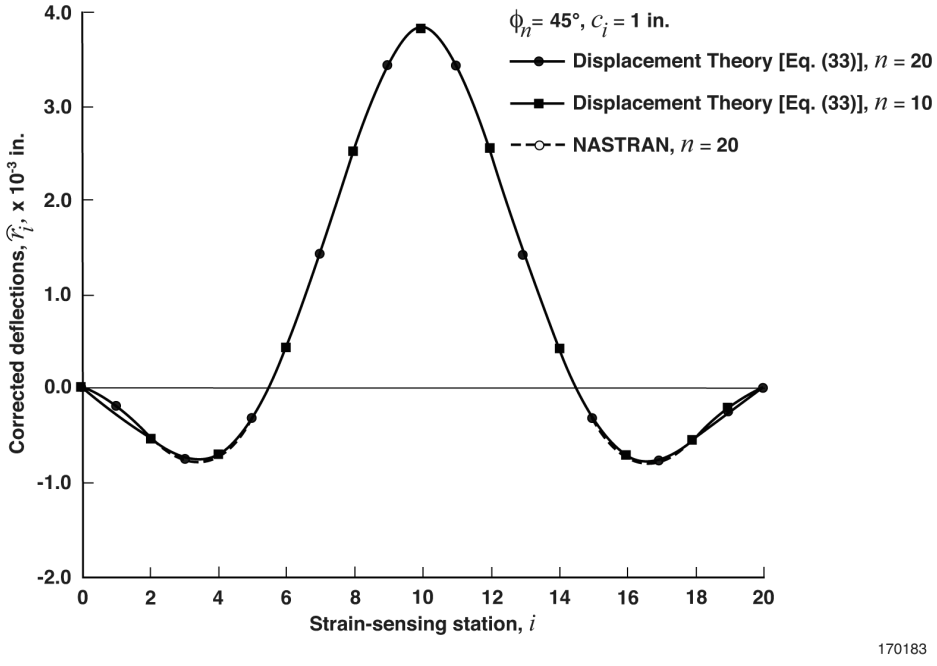

Figure 29b. Corrected, eq. (33).

Figure 29. Theoretical deflection curves calculated from equations (17) and (33) based on the domain densities $(n = 20,\ n = 10)$ compared with the Nastran-generated deflection curve $(n = 20)$ for the two-end fixed curved beam $(\phi_n = 45°)$ under a central load of $P = 100$ lb.

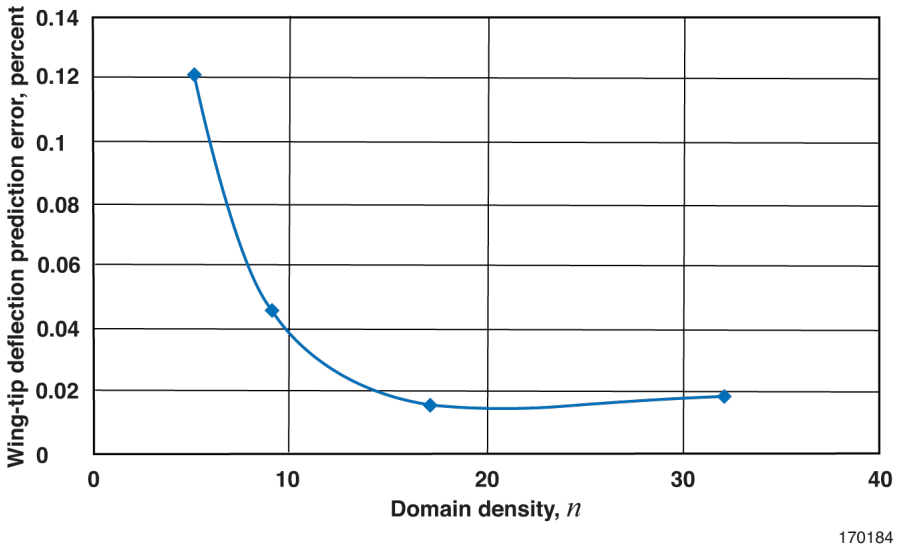

Figure 30. Plot of the wing-tip deflection prediction error as a function of the domain density n (figure 13 of ref. 11).

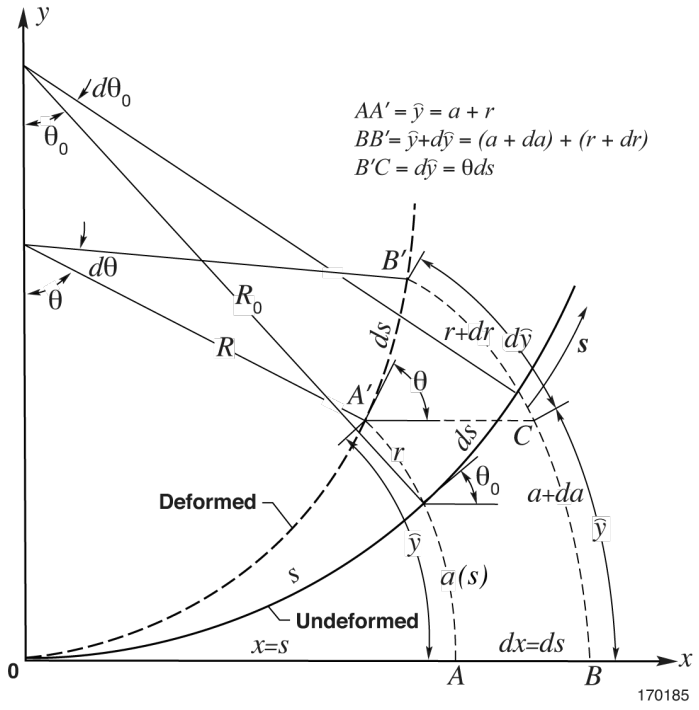

Figure 31. Small segment ds of undeformed and deformed embedded curved beam for geometrically relating the curved deflection increment $d\hat{y}$ to slope angle θ through $d\hat{y} = \theta ds$.

Appendix A
Derivations of Slope Angle and Deflection Equations in Recursive Forms for Embedded Curved Beams

Appendix A presents mathematical details of piecewise integrations of the slope equation (12) and the deflection equation (14) for the embedded curved beams based on piecewise linear strain representations. Keep in mind that within a small domain $s_{i-1} \le s \le s_i \ (i = 1,2,3,...,n)$ between the two adjacent strain-sensing stations $\{s_{i-1}, s_i\}$, the variation of the depth factor $c(s)$ is extremely small. If $\{c_{i-1}, c_i\}$ are respectively the depth factors at the strain-sensing stations $\{s_{i-1}, s_i\}$, then $c(s)$ can be approximated with the averaged depth factor $c(s) \approx c \equiv (c_{i-1} + c_i)/2$. Therefore, to simplify mathematics, the factor $(1 + c/R_0)(1/c)$ can be moved outside the integral signs as shown in the following section.

Slope-Angle Equation

The slope equation (12) for the embedded curved beam within the small domain $s_{i-1} \le s \le s_i$ between the two adjacent strain-sensing stations $\{s_{i-1}, s_i\}$ is duplicated as equation (A1):

$$\alpha(s) = \underbrace{\left(1 + \frac{c}{R_0}\right)\frac{1}{c}\int_{s_{i-1}}^{s} \varepsilon(s)\,ds}_{\text{Slope angle inclement due to } \varepsilon(s)} + \underbrace{\alpha_{i-1}}_{\substack{\text{Slope angle} \\ \text{at } s_{i-1}}} \quad ; \quad (s_{i-1} \le s \le s_i) \tag{A1}$$

Based on the linear representation of surface strains $\varepsilon(s)$ within the domain $(s_{i-1} \le s \le s_i)$ given by equation (A2):

$$\varepsilon(s) = \varepsilon_{i-1} - (\varepsilon_{i-1} - \varepsilon_i)\frac{s - s_{i-1}}{\Delta l} \quad ; \quad (s_{i-1} \le s \le s_i) \tag{A2}$$

equation (A1) can be integrated to yield equation (A3) (ref. 14):

$$\begin{aligned} \alpha(s) &= \left(1 + \frac{c}{R_0}\right)\frac{1}{c}\int_{s_{i-1}}^{s}\left[\varepsilon_{i-1} - (\varepsilon_{i-1} - \varepsilon_i)\frac{s - s_{i-1}}{\Delta l}\right]ds + \alpha_{i-1} \\ &= \frac{1}{c}\left(1 + \frac{c}{R_0}\right)\left[\varepsilon_{i-1}(s - s_{i-1}) - (\varepsilon_{i-1} - \varepsilon_i)\frac{(s - s_{i-1})^2}{2\Delta l}\right] + \alpha_{i-1} \end{aligned} \tag{A3}$$

At the strain-sensing station s_i, one can write $(s_i - s_{i-1}) \equiv \Delta l$, and equation (A3) yields the slope angle $\alpha_i [\equiv \alpha(s_i)]$ at the strain-sensing station s_i as equation (A4):

$$\alpha_i = \left(1 + \frac{c}{R_0}\right)\frac{1}{c}\left[\varepsilon_{i-1}(\Delta l) - (\varepsilon_{i-1} - \varepsilon_i)\frac{(\Delta l)^2}{2\Delta l}\right] + \alpha_{i-1} \quad ; \quad (i = 1,2,3,...,n) \tag{A4}$$

After grouping terms, equation (A4) takes on the final recursive form of slope-angle equation for the embedded curved beam as equation (A5);

$$\alpha_i = \left(1+\frac{c}{R_0}\right)\frac{\Delta l}{2c}\left(\varepsilon_{i-1}+\varepsilon_i\right)+\alpha_{i-1} \quad ; \quad (i=1,2,3,...,n) \tag{A5}$$

Equation (A5) is identical to equation (15a) in the text.

Deflection Equations

The deflection equation (14) for the embedded curved beam within the domain $s_{i-1} \le s \le s_i$ between the two adjacent strain-sensing stations $\{s_{i-1}, s_i\}$ is duplicated below as equation (A-6):

$$r(s) = \underbrace{\left(1+\frac{c}{R_0}\right)\frac{1}{c}\int_{s_{i-1}}^{s}\int_{s_{i-1}}^{s}\varepsilon(s)\,ds\,ds}_{\text{Deflection increment due to } \varepsilon(s)} + \underbrace{r_{i-1}}_{\substack{\text{Deflection}\\ \text{at } s_{i-1}}} + \underbrace{(s-s_{i-1})\alpha_{i-1}}_{\substack{\text{Deflection}\\ \text{due to } \alpha_{i-1}}} \quad ; \quad (s_{i-1} \le s \le s_i) \tag{A6}$$

Substituting equation (A2) into equation (A6), and carrying out the integrations, one obtains equation (A7) (ref. 14):

$$\begin{aligned} r(s) &= \left(1+\frac{c}{R_0}\right)\frac{1}{c}\int_{s_{i-1}}^{s}\int_{s_{i-1}}^{s}\left[\varepsilon_{i-1}-(\varepsilon_{i-1}-\varepsilon_i)\frac{s-s_{i-1}}{\Delta l}\right]ds\,ds + r_{i-1} + (s-s_{i-1})\alpha_{i-1} \\ &= \left(1+\frac{c}{R_0}\right)\frac{1}{c}\int_{s_{i-1}}^{s}\left[\varepsilon_{i-1}(s-s_{i-1})-(\varepsilon_{i-1}-\varepsilon_i)\frac{(s-s_{i-1})^2}{2\Delta l}\right]ds + r_{i-1} + (s-s_{i-1})\alpha_{i-1} \\ &= \left(1+\frac{c}{R_0}\right)\frac{1}{c}\left[\varepsilon_{i-1}\frac{(s-s_{i-1})^2}{2}-(\varepsilon_{i-1}-\varepsilon_i)\frac{(s-s_{i-1})^3}{6\Delta l}\right] + r_{i-1} + (s-s_{i-1})\alpha_{i-1} \\ &\qquad\qquad (s_{i-1} \le s \le s_i) \end{aligned} \tag{A7}$$

At the strain-sensing station s_i, one can write $(s_i - s_{i-1}) \equiv \Delta l$, and equation (A7) yields the curvilinear deflection $r_i[\equiv r(s_i)]$ at the strain-sensing station s_i as equation (A8):

$$r_i = \left(1+\frac{c}{R_0}\right)\frac{1}{c}\left[\varepsilon_{i-1}\frac{(\Delta l)^2}{2}-(\varepsilon_{i-1}-\varepsilon_i)\frac{(\Delta l)^3}{6\Delta l}\right] + r_{i-1} + (\Delta l)\alpha_{i-1} \quad ; \quad (i=1,2,3,...,n) \tag{A8}$$

After grouping terms, equation (A8) takes on the final form of a deflection equation for the embedded curved beam as equation (A9):

$$r_i = \left(1+\frac{c}{R_0}\right)\frac{(\Delta l)^2}{6c}\left(2\varepsilon_{i-1}+\varepsilon_i\right) + r_{i-1} + (\Delta l)\alpha_{i-1} \quad ; \quad (i=1,2,3,...,n) \tag{A9}$$

Equation (A9) is the recursive form of the deflection equation (15b) in the text.

Appendix B
Derivations of the Deflection Equation in Summation Form for Embedded Curved Beams

Appendix B presents the mathematical steps for obtaining the final summation form of the deflection equation given by equation (15c). The slope-angle equation (A5) and the deflection equation (A9) in recursive forms for embedded curved beams are duplicated below respectively as equations (B1) and (B2):

$$\alpha_i = \left(1+\frac{c}{R_0}\right)\frac{\Delta l}{2c}\left(\varepsilon_{i-1}+\varepsilon_i\right)+\alpha_{i-1} \quad ; \quad (i=1,2,3,...,n) \tag{B1}$$

$$r_i = \left(1+\frac{c}{R_0}\right)\frac{(\Delta l)^2}{6c}\left(2\varepsilon_{i-1}+\varepsilon_i\right)+r_{i-1}+(\Delta l)\alpha_{i-1} \quad ; \quad (i=1,2,3,...,n) \tag{B2}$$

Equations (B1) and (B2) can now be combined into a single deflection equation in summation form as follows. Writing out equation (B2) for different indices *i*, and making use of the indicial relationships expressed in equations (B1) and (B2), one obtains equations (B3)–(B5):

For $i = 1$:

$$r_1 = \left(1+\frac{c}{R_0}\right)\frac{(\Delta l)^2}{6c}\left(2\varepsilon_0+\varepsilon_1\right)+r_0+(\Delta l)\alpha_0 \tag{B3}$$

For $i = 2$:

$$\begin{aligned} r_2 &= \left(1+\frac{c}{R_0}\right)\frac{(\Delta l)^2}{6c}\left(2\varepsilon_1+\varepsilon_2\right)+r_1+(\Delta l)\alpha_1 \\ &= \left(1+\frac{c}{R_0}\right)\frac{(\Delta l)^2}{6c}\left(2\varepsilon_1+\varepsilon_2\right)+\underbrace{\left(1+\frac{c}{R_0}\right)\frac{(\Delta l)^2}{6c}\left(2\varepsilon_0+\varepsilon_1\right)+(\Delta l)\alpha_0+r_0}_{r_1} \\ &\quad +\underbrace{\left(1+\frac{c}{R_0}\right)\frac{(\Delta l)^2}{2c}\left(\varepsilon_0+\varepsilon_1\right)+(\Delta l)\alpha_0}_{(\Delta l)\alpha_1} \\ &= \left(1+\frac{c}{R_0}\right)\frac{(\Delta l)^2}{6c}\left(2\varepsilon_1+\varepsilon_2\right)+\left(1+\frac{c}{R_0}\right)\frac{(\Delta l)^2}{6c}\left(2\varepsilon_0+\varepsilon_1\right)+\left(1+\frac{c}{R_0}\right)\frac{(\Delta l)^2}{2c}\left(\varepsilon_0+\varepsilon_1\right) \\ &\quad +r_0+2(\Delta l)\alpha_0 \end{aligned} \tag{B4}$$

For i =3

$$\begin{aligned}
\hat{y}_3 &= \left(1+\frac{c}{R_0}\right)\frac{(\Delta l)^2}{6c}\left(2\varepsilon_2+\varepsilon_3\right)+r_2+(\Delta l)\alpha_2 \\
&= \left(1+\frac{c}{R_0}\right)\frac{(\Delta l)^2}{6c}\left(2\varepsilon_2+\varepsilon_3\right) \\
&\quad + \underbrace{\left(1+\frac{c}{R_0}\right)\frac{(\Delta l)^2}{6c}\left(2\varepsilon_1+\varepsilon_2\right)+\left(1+\frac{c}{R_0}\right)\frac{(\Delta l)^2}{6c}\left(2\varepsilon_0+\varepsilon_1\right)+\left(1+\frac{c}{R_0}\right)\frac{(\Delta l)^2}{2c}\left(\varepsilon_0+\varepsilon_1\right)+r_0+2(\Delta l)\alpha_0}_{r_2} \\
&\quad + \underbrace{\left(1+\frac{c}{R_0}\right)\frac{(\Delta l)^2}{2c}\left(\varepsilon_1+\varepsilon_2\right)+\left(1+\frac{c}{R_0}\right)\frac{(\Delta l)^2}{2c}\left(\varepsilon_0+\varepsilon_1\right)+(\Delta l)\alpha_0}_{(\Delta l)\alpha_2}
\end{aligned} \tag{B5}$$

$$\begin{aligned}
&= \left(1+\frac{c}{R_0}\right)\frac{(\Delta l)^2}{6c}\left(2\varepsilon_2+\varepsilon_3\right)+\left(1+\frac{c}{R_0}\right)\frac{(\Delta l)^2}{6c}\left(2\varepsilon_1+\varepsilon_2\right)+\left(1+\frac{c}{R_0}\right)\frac{(\Delta l)^2}{6c}\left(2\varepsilon_0+\varepsilon_1\right) \\
&\quad +(3-2)\left(1+\frac{c}{R_0}\right)\frac{(\Delta l)^2}{2c}\left(\varepsilon_1+\varepsilon_2\right)+(3-1)\left(1+\frac{c}{R_0}\right)\frac{(\Delta l)^2}{2c}\left(\varepsilon_0+\varepsilon_1\right)+r_0+3(\Delta l)\alpha_0
\end{aligned}$$

Based on the indicial progression patterns in equations (B3)−(B5), one can write the deflection, $\hat{y}_i$, in a generalized form with two summations (with different summation limits) as equation (B6):

$$r_i = \underbrace{\left(1+\frac{c}{R_0}\right)\frac{(\Delta l)^2}{6c}\sum_{j=1}^{i}(2\varepsilon_{j-1}+\varepsilon_j)}_{\text{Contributions from deflection terms}} + \underbrace{\left(1+\frac{c}{R_0}\right)\frac{(\Delta l)^2}{2c}\sum_{j=1}^{i-1}(i-j)(\varepsilon_{j-1}+\varepsilon_j)}_{\text{Contributions from slope-angle terms}} + \underbrace{r_0+(i)(\Delta l)\alpha_0}_{=0 \text{ for cantilever beams}} \tag{B6}$$

$$(i=1,2,3,...,n)$$

Equation (B6) is identical to equation (15c) in the text. A set of three equations {(B1), (B2), and (B6)} are called Curvilinear Displacement Transfer Functions for the embedded curved beams.

Appendix C
Derivations of Improved Slope Angle and Deflection Equations in Recursive Forms for Embedded Curved Beams

Appendix C presents the details of integrations of the slope equation (12) and the deflection equation (14) for the embedded curved beams based on piecewise nonlinear strain representations to obtain slope-angle and deflection equations in recursive forms.

Slope-Angle Equation

The slope equation (12) for the embedded curved beam within the small domain $s_{i-1} \le s \le s_i$ between the two adjacent strain-sensing stations $\{s_{i-1}, s_i\}$ is duplicated as equation (C1):

$$\alpha(s) = \underbrace{\left(1+\frac{c}{R_0}\right)\frac{1}{c}\int_{s_{i-1}}^{s}\varepsilon(s)ds}_{\text{Slope angle increment due to } \varepsilon(s)} + \underbrace{\alpha_{i-1}}_{\substack{\text{Slope angle} \\ \text{at } s_{i-1}}} \quad ; \quad (s_{i-1} \le s \le s_i) \tag{C1}$$

The nonlinear representation of strain $\varepsilon(s)$ in the domain $s_{i-1} \le s \le s_i$ between the two adjacent strain-sensing stations $\{s_{i-1}, s_i\}$ described by equation (9a), is duplicated below as equation (C2):

$$\varepsilon(s) = \varepsilon_{i-1} - \frac{3\varepsilon_{i-1} - 4\varepsilon_i + \varepsilon_{i+1}}{2\Delta l}(s - s_{i-1}) + \frac{\varepsilon_{i-1} - 2\varepsilon_i + \varepsilon_{i+1}}{2(\Delta l)^2}(s - s_{i-1})^2 \qquad (s_{i-1} \le s \le s_i) \tag{C2}$$

In view of equation (C2), equation (C1) can be integrated to yield equation (C3) (ref. 14):

$$\begin{aligned}\alpha(s) &= \left(1+\frac{c}{R_0}\right)\frac{1}{c}\int_{s_{i-1}}^{s}\left[\varepsilon_{i-1} - \frac{3\varepsilon_{i-1} - 4\varepsilon_i + \varepsilon_{i+1}}{2\Delta l}(s - s_{i-1}) + \frac{\varepsilon_{i-1} - 2\varepsilon_i + \varepsilon_{i+1}}{2(\Delta l)^2}(s - s_{i-1})^2\right]ds + \alpha_{i-1} \\ &= \left(1+\frac{c}{R_0}\right)\frac{1}{c}\left[\varepsilon_{i-1}(s - s_{i-1}) - \frac{3\varepsilon_{i-1} - 4\varepsilon_i + \varepsilon_{i+1}}{4\Delta l}(s - s_{i-1})^2 + \frac{\varepsilon_{i-1} - 2\varepsilon_i + \varepsilon_{i+1}}{6(\Delta l)^2}(s - s_{i-1})^3\right] + \alpha_{i-1} \\ &\qquad (s_{i-1} \le s \le s_i)\end{aligned} \tag{C3}$$

At the strain-sensing station s_i, one can write $(s_i - s_{i-1}) \equiv \Delta l$, and equation (C3) yields the slope angle $\alpha_i [\equiv \alpha(s_i)]$ at the strain-sensing station s_i as equation (C4):

$$\alpha_i = \left(1+\frac{c}{R_0}\right)\frac{\Delta l}{c}\left[\varepsilon_{i-1} - \frac{3\varepsilon_{i-1} - 4\varepsilon_i + \varepsilon_{i+1}}{4} + \frac{\varepsilon_{i-1} - 2\varepsilon_i + \varepsilon_{i+1}}{6}\right] + \alpha_{i-1} \quad ; \quad (i = 1,2,3,...,n) \tag{C4}$$

After grouping terms, equation (C4) takes on the final form shown as equation (C5):

$$\alpha_i = \left(1+\frac{c}{R_0}\right)\frac{\Delta l}{12c}(5\varepsilon_{i-1}+8\varepsilon_i-\varepsilon_{i+1})+\alpha_{i-1} \quad ; \quad (i=1,2,3,...,n) \tag{C5}$$

Equation (C5) is identical to equation (16a) in the text.

Deflection Equations

The curvilinear deflection $r(s)$ in a small domain $s_{i-1} \le s \le s_i$ between the two adjacent strain-sensing stations $\{s_{i-1}, s_i\}$ for the embedded curved beams, can be obtained by carrying out the integration of the deflection equation (14), which is duplicated below as equation (C6)]:

$$r(s) = \underbrace{\left(1+\frac{c}{R_0}\right)\frac{1}{c}\int_{s_{i-1}}^{s}\int_{s_{i-1}}^{s}\varepsilon(s)ds\,ds}_{\text{Deflection increment due to } \varepsilon(s)} + \underbrace{r_{i-1}}_{\substack{\text{Deflection}\\ \text{at } s_{i-1}}} + \underbrace{(s-s_{i-1})\alpha_{i-1}}_{\substack{\text{Deflection}\\ \text{due to } \alpha_{i-1}}} \quad ; \quad (s_{i-1} \le s \le s_i) \tag{C6}$$

Substituting equation (C3) into equation (C6), and carrying out integrations (ref. 14), one obtains the curvilinear deflection $r(s)$ at any point within the domain $s_{i-1} \le s \le s_i$ as equation (C7):

$$\begin{aligned} r(s) &= \left(1+\frac{c}{R_0}\right)\frac{1}{c}\int_{s_{i-1}}^{s}\left[\varepsilon_{i-1}(s-s_{i-1}) - \frac{3\varepsilon_{i-1}-4\varepsilon_i+\varepsilon_{i+1}}{4\Delta l}(s-s_{i-1})^2 + \frac{\varepsilon_{i-1}-2\varepsilon_i+\varepsilon_{i+1}}{6(\Delta l)^2}(s-s_{i-1})^3\right]ds \\ &\quad + r_{i-1} + (s-s_{i-1})\alpha_{i-1} \\ &= \left(1+\frac{1}{R_0}\right)\frac{1}{c}\left[\frac{\varepsilon_{i-1}}{2}(s-s_{i-1})^2 - \frac{3\varepsilon_{i-1}-4\varepsilon_i+e_{i+1}}{12\Delta l}(s-s_{i-1})^3 + \frac{\varepsilon_{i-1}-2\varepsilon_i+\varepsilon_{i+1}}{24(\Delta l)^2}(s-s_{i-1})^4\right] \\ &\quad + r_{i-1} + (s-s_{i-1})\alpha_{i-1} \end{aligned} \tag{C7}$$

$$(s_{i-1} \le s \le s_i)$$

At the strain-sensing station s_i, one can write $(s_i - s_{i-1}) \equiv \Delta l$, and equation (C7) gives the deflection, $r_i[\equiv r(s_i)]$, at the strain-sensing station s_i as equation (C8):

$$r_i = \left(1+\frac{c}{R_0}\right)\frac{(\Delta l)^2}{c}\left[\frac{\varepsilon_{i-1}}{2} - \frac{3\varepsilon_{i-1}-4\varepsilon_i+\varepsilon_{i+1}}{12} + \frac{\varepsilon_{i-1}-2\varepsilon_i+\varepsilon_{i+1}}{24}\right] + r_{i-1} + (\Delta l)\alpha_{i-1} \tag{C8}$$

$$(i=1,2,3,...,n)$$

After grouping terms, equation (C8) takes on the final form as equation (C9):

$$r_i = \left(1+\frac{c}{R_0}\right)\frac{(\Delta l)^2}{24c}(7\varepsilon_{i-1}+6\varepsilon_i-\varepsilon_{i+1}) + r_{i-1} + (\Delta l)\alpha_{i-1} \quad ; \quad (i=1,2,3,...,n) \tag{C9}$$

Equation (C9) is identical to equation (16b) in the text.

Appendix D
Derivations of the Improved Deflection Equation in Summation Form for Embedded Curved Beams

Appendix D derives the final deflection equation in dual summation form for the embedded curved beams using nonlinear strain representations. Equations (C5) and (C9) are duplicated below respectively as equations (D1) and (D2).

$$\alpha_i = \left(1+\frac{c}{R_0}\right)\frac{\Delta l}{12c}(5\varepsilon_{i-1}+8\varepsilon_i-\varepsilon_{i+1})+\alpha_{i-1} \quad ; \quad (i=1,2,3,...,n) \tag{D1}$$

$$r_i = \left(1+\frac{c}{R_0}\right)\frac{(\Delta l)^2}{24c}(7\varepsilon_{i-1}+6\varepsilon_i-\varepsilon_{i+1})+r_{i-1}+(\Delta l)\alpha_{i-1} \quad ; \quad (i=1,2,3,...,n) \tag{D2}$$

Equations (D1) and (D2) can be combined into a single deflection equation with summation form as follows. Writing out equation (D2) for different indices *i,* and making use of the indicial relationships expressed in equations (D1) and (D2), one obtains equations (D3), (D5), (D7) respectively for indices i = 1, 2, 3:

For $i=1$:

$$r_1 = \left(1+\frac{c}{R_0}\right)\frac{(\Delta l)^2}{24c}(7\varepsilon_0+6\varepsilon_1-\varepsilon_2)+r_0+(\Delta l)\alpha_0 \tag{D3}$$

For $i=2$:

$$\begin{aligned} r_2 &= \left(1+\frac{c}{R_0}\right)\frac{(\Delta l)^2}{24c}(7\varepsilon_1+6\varepsilon_2-\varepsilon_3)+r_1+(\Delta l)\alpha_1 \\ &= \left(1+\frac{c}{R_0}\right)\frac{(\Delta l)^2}{24c}(7\varepsilon_1+6\varepsilon_2-\varepsilon_3)+\underbrace{\left(1+\frac{c}{R_0}\right)\frac{(\Delta l)^2}{24c}(7\varepsilon_0+6\varepsilon_1-\varepsilon_2)+r_0+(\Delta l)\alpha_0}_{r_1} \\ &\quad +\underbrace{\left(1+\frac{c}{R_0}\right)\frac{(\Delta l)^2}{12c}(5\varepsilon_0+8\varepsilon_1-\varepsilon_2)+(\Delta l)\alpha_0}_{(\Delta l)\alpha_1} \end{aligned} \tag{D4}$$

After grouping terms, equation (D4) becomes equation (D5):

$$\begin{aligned} r_2 &= \left(1+\frac{c}{R_0}\right)\frac{(\Delta l)^2}{24c}(7\varepsilon_1+6\varepsilon_2-\varepsilon_3)+\left(1+\frac{c}{R_0}\right)\frac{(\Delta l)^2}{24c}(7\varepsilon_0+6\varepsilon_1-\varepsilon_2) \\ &\quad +(2-1)\left(1+\frac{c}{R_0}\right)\frac{(\Delta l)^2}{12c}(5\varepsilon_0+8\varepsilon_1-\varepsilon_2)+r_0+2(\Delta l)\alpha_0 \end{aligned} \tag{D5}$$

For $i = 3$:

$$
\begin{aligned}
r_3 &= \left(1+\frac{c}{R_0}\right)\frac{(\Delta l)^2}{24c}(7\varepsilon_2+6\varepsilon_3-\varepsilon_4)+r_2+(\Delta l)\alpha_2 \\
&= \left(1+\frac{c}{R_0}\right)\frac{(\Delta l)^2}{24c}(7\varepsilon_2+6\varepsilon_3-\varepsilon_4) \\
&+ \underbrace{\left\{\begin{array}{l}\left(1+\frac{c}{R_0}\right)\frac{(\Delta l)^2}{24c}(7\varepsilon_1+6\varepsilon_2-\varepsilon_3)+\left(1+\frac{c}{R_0}\right)\frac{(\Delta l)^2}{24c}(7\varepsilon_0+6\varepsilon_1-\varepsilon_2) \\ +(2-1)\left(1+\frac{c}{R_0}\right)\frac{(\Delta l)^2}{12c}(5\varepsilon_0+8\varepsilon_1-\varepsilon_2)+r_0+2(\Delta l)\alpha_0\end{array}\right\}}_{r_2} \\
&\underbrace{+\left(1+\frac{c}{R_0}\right)\frac{(\Delta l)^2}{12c}(5\varepsilon_1+8\varepsilon_2-\varepsilon_3)+\left(1+\frac{c}{R_0}\right)\frac{(\Delta l)^2}{12c}(5\varepsilon_0+8\varepsilon_1-\varepsilon_2)+(\Delta l)\alpha_0}_{(\Delta l)\alpha_2}
\end{aligned}
\tag{D6}
$$

After grouping terms, equation (D6) becomes equation (D7):

$$
\begin{aligned}
r_3 &= \left(1+\frac{c}{R_0}\right)\frac{(\Delta l)^2}{24c}(7\varepsilon_2+6\varepsilon_3-\varepsilon_4)+\left(1+\frac{c}{R_0}\right)\frac{(\Delta l)^2}{24c}(7\varepsilon_1+6\varepsilon_2-\varepsilon_3) \\
&+\left(1+\frac{c}{R_0}\right)\frac{(\Delta l)^2}{24c}(7\varepsilon_0+6\varepsilon_1-\varepsilon_2) \\
&+(3-2)\left(1+\frac{c}{R_0}\right)\frac{(\Delta l)^2}{12c}(5\varepsilon_1+8\varepsilon_2-\varepsilon_3)+(3-1)\left(1+\frac{c}{R_0}\right)\frac{(\Delta l)^2}{12c}(5\varepsilon_0+8\varepsilon_1-\varepsilon_2) \\
&+r_0+3(\Delta l)\alpha_0
\end{aligned}
\tag{D7}
$$

Observing the indicial behavior, equation (D7) can be generalized for index *i*, the curved deflection, r_i, can be expressed in a generalized form with two summations (with different summation limits) as equation (D8):

$$
\begin{aligned}
r_i &= \underbrace{\left(1+\frac{c}{R_0}\right)\frac{(\Delta l)^2}{24c}\sum_{j=1}^{i}(7\varepsilon_{j-1}+6\varepsilon_j-\varepsilon_{j+1})+r_0}_{\text{Contributions from deflection terms}} \\
&+\underbrace{\left(1+\frac{c}{R_0}\right)\frac{(\Delta l)^2}{12c}\sum_{j=1}^{i-1}(i-j)(5\varepsilon_{j-1}+8\varepsilon_j-\varepsilon_{j+1})+(i)(\Delta l)\alpha_0}_{\text{Contributions from slope terms}} \\
&\qquad (i=1,2,3,...,n)
\end{aligned}
\tag{D8}
$$

Equation (D8) can be rewritten in the following form as equation (D9):

$$r_i = \underbrace{\left(1+\frac{c}{R_0}\right)\frac{(\Delta l)^2}{24c}\sum_{j=1}^{i}(7\varepsilon_{j-1}+6\varepsilon_j-\varepsilon_{j+1})}_{\text{Contributions from deflection terms}} + \underbrace{\left(1+\frac{c}{R_0}\right)\frac{(\Delta l)^2}{12c}\sum_{j=1}^{i-1}(i-j)(5\varepsilon_{j-1}+8\varepsilon_j-\varepsilon_{j+1})}_{\text{Contributions from slope-angle terms}} + \underbrace{r_0+(i)(\Delta l)\alpha_0}_{=0 \text{ for cantilever beams}} \qquad (D9)$$

$$(i=1,2,3,...,n)$$

Equation (D9) is identical to the deflection equation (16c) in the text. A set of three equations {(D1), (D2), and (D9)} are called the Improved Curvilinear Displacement Transfer Functions for the embedded curved beams.

Appendix E
Nastran and Theoretical Data for Cantilever Curved Beams

Table E1. Nastran-generated surface strain and deflection data, and theoretical deflection data for the cantilever straight beam under a tip load of $P = 100$ lb and curved-beam angle $\phi_n = 0°$, $n = 20$.

i	$\bar{\varepsilon}_i$, $\times 10^{-4}$ in/in (inner)	ε_i, $\times 10^{-4}$ in/in (outer)	u_i, in. (Nastran)	v_i, in. (Nastran)	d_i, $\equiv \sqrt{u_i^2 + v_i^2}$	$r_i^{(N)}$, in. (Nastran) [eq. (29)]	c_i, in. (Given)	r_i, in. (Disp. Theory) [eq. (15)]	r_i, in. (Disp. Theory) [eq. (16)]
0	-7.50019	7.50019	0.00000	0.00000	0.00000	0.00000	1.00000	0.00000	0.00000
1	-7.12518	7.12518	0.00000	0.00925	0.00925	0.00925	1.00000	0.00922	0.00922
2	-6.75017	6.75017	0.00000	0.03632	0.03632	0.03632	1.00000	0.03626	0.03627
3	-6.37516	6.37516	0.00000	0.08026	0.08026	0.08026	1.00000	0.08018	0.08019
4	-6.00015	6.00015	0.00000	0.14013	0.14013	0.14013	1.00000	0.14005	0.14005
5	-5.62514	5.62514	0.00000	0.21501	0.21501	0.21501	1.00000	0.21492	0.21493
6	-5.25013	5.25013	0.00000	0.30395	0.30395	0.30395	1.00000	0.30386	0.30387
7	-4.87512	4.87512	0.00000	0.40602	0.40602	0.40612	1.00000	0.40593	0.40594
8	-4.50011	4.50011	0.00000	0.52027	0.52027	0.52027	1.00000	0.52020	0.52021
9	-4.12510	4.12510	0.00000	0.64578	0.64578	0.64578	1.00000	0.64572	0.64573
10	-3.75009	3.75009	0.00000	0.78159	0.78159	0.78160	1.00000	0.78156	0.78157
11	-3.37508	3.37508	0.00000	0.92679	0.92679	0.92680	1.00000	0.92678	0.92680
12	-3.00008	3.00008	0.00000	1.08042	1.08042	1.08042	1.00000	1.08045	1.08046
13	-2.62507	2.62507	0.00000	1.24155	1.24155	1.24156	1.00000	1.24162	1.24163
14	-2.25006	2.25006	0.00000	1.40924	1.40924	1.41026	1.00000	1.40936	1.40938
15	-1.87505	1.87505	0.00000	1.58256	1.58256	1.58258	1.00000	1.58273	1.58275
16	-1.50004	1.50004	0.00000	1.76056	1.76056	1.76057	1.00000	1.76080	1.76082
17	-1.12503	1.12503	0.00000	1.94232	1.94232	1.94239	1.00000	1.94262	1.94264
18	-0.75002	0.75002	0.00000	2.12689	2.12689	2.12711	1.00000	2.12726	2.12728
19	-0.37501	0.37501	0.00000	2.31333	2.31333	2.31337	1.00000	2.31378	2.31380
20	0.00000	0.00000	0.00000	2.50071	2.50071	2.50077	1.00000	2.50125	2.50127

Table E2a. Nastran-generated surface strain and deflection data, and theoretical deflection data for the cantilever curved beam under a tip load of $P = 100$ lb and curved-beam angle $\phi_n = 45°$, $n = 20$.

i	$\bar{\varepsilon}_i$,$\times 10^{-4}$ in/in (inner)	ε_i ,$\times 10^{-4}$ in/in (outer)	u_i, in. (Nastran)	v_i, in. (Nastran)	d_i, $\equiv \sqrt{u_i^2 + v_i^2}$	$r_i^{(N)}$, in. (Nastran) [eq. (29)]	c_i, in. (Given)	r_i, in. (Disp. Theory) [eq. (15)]	r_i, in. (Disp. Theory) [eq. (16)]
0	-6.76988	6.73522	0.00000	0.00000	0.00000	0.00000	1.00222	0.00000	0.00000
1	-6.49922	6.46528	-0.00017	0.00835	0.00835	0.00835	1.00231	0.00836	0.00836
2	-6.21814	6.18568	-0.00163	0.03286	0.03290	0.03290	1.00242	0.03298	0.03298
3	-5.92752	5.89657	-0.00556	0.07271	0.07292	0.07292	1.00254	0.07315	0.07316
4	-5.62775	5.59837	-0.01308	0.12702	0.12769	0.12769	1.00267	0.12815	0.12817
5	-5.31931	5.29153	-0.02519	0.19480	0.19642	0.19642	1.00283	0.19722	0.19724
6	-5.00269	4.97656	-0.04279	0.27500	0.27831	0.27831	1.00200	0.27958	0.27962
7	-4.67834	4.65392	-0.06667	0.36652	0.37253	0.37254	1.00322	0.37445	0.37450
8	-4.34673	4.32404	-0.09753	0.46819	0.47824	0.47824	1.00346	0.48100	0.48106
9	-4.00846	3.98753	-0.13589	0.57881	0.59455	0.59455	1.00250	0.59841	0.59848
10	-3.66402	3.64489	-0.18221	0.69713	0.72055	0.72056	1.00274	0.72583	0.72592
11	-3.31389	3.29659	-0.23680	0.82192	0.85535	0.85536	1.00151	0.86240	0.86251
12	-2.95867	2.94322	-0.29986	0.95190	0.99801	0.99802	1.00339	1.00726	1.00739
13	-2.59894	2.58536	-0.37141	1.08581	1.14758	1.14759	1.00193	1.15952	1.15966
14	-2.23515	2.22349	-0.45146	1.22239	1.30309	1.30311	1.00448	1.31827	1.31843
15	-1.86790	1.85815	-0.53984	1.36042	1.46362	1.46364	1.00268	1.48260	1.48279
16	-1.49778	1.48996	-0.63622	1.49869	1.62814	1.62817	1.00334	1.65160	1.65181
17	-1.12536	1.11949	-0.74020	1.63605	1.79570	1.79574	1.00444	1.82434	1.82457
18	-0.75120	0.74728	-0.85127	1.77139	1.96532	1.96536	1.00000	1.99990	2.00015
19	-0.37589	0.37393	-0.96881	1.90367	2.13601	2.13606	1.01333	2.17733	2.17760
20	-0.00049	0.00049	-1.09211	2.03190	2.30680	2.30685	1.00000	2.35569	2.35598

Additional table for $\phi_n = 45°$ and $n = 10$

Table E2b. Nastran-generated surface strain and deflection data, and theoretical deflection data for the cantilever curved beam under a tip load of $P = 100$ lb and curved-beam angle $\phi_n = 45°$, $n = 10$.

i	$\bar{\varepsilon}_i$,$\times 10^{-4}$ in/in (inner)	ε_i ,$\times 10^{-4}$ in/in (outer)	u_i, in. (Nastran)	v_i, in. (Nastran)	d_i, $\equiv \sqrt{u_i^2 + v_i^2}$	$r_i^{(N)}$, in. (Nastran) [eq. (29)]	c_i, in. (Given)	r_i, in. (Disp. Theory) [eq. (15)]	r_i, in. (Disp. Theory) [eq. (16)]
0	-6.76952	6.73558	0.00000	0.00000	0.00000	0.00000	1.00222	0.00000	0.00000
1	-6.21813	6.18568	-0.00131	0.03285	0.03288	0.03288	1.00242	0.03297	0.03298
2	-5.62774	5.59837	-0.01247	0.12699	0.12760	0.12760	1.00267	0.12810	0.12816
3	-5.00267	4.97657	-0.04190	0.27494	0.27811	0.27812	1.00200	0.27949	0.27963
4	-4.34672	4.32404	-0.09639	0.46808	0.47790	0.47790	1.00346	0.48087	0.48111
5	-3.66401	3.64489	-0.18083	0.69696	0.72004	0.72004	1.00274	0.72564	0.72600
6	-2.95872	2.94328	-0.29824	0.95164	0.99728	0.99729	1.00339	1.00695	1.00744
7	-2.23515	2.22349	-0.44968	1.22204	1.30215	1.30217	1.00448	1.31775	1.31839
8	-1.49777	1.48995	-0.63426	1.49823	1.62695	1.62698	1.00334	1.65082	1.65161
9	-0.75121	0.74729	-0.84913	1.77081	1.96387	1.96391	1.00000	1.99885	1.99981
10	-0.00098	-0.00098	-1.08982	2.03118	2.30508	2.30514	1.00000	2.35442	2.35554

Table E3. Nastran-generated surface strain and deflection data, and theoretical deflection data for the cantilever curved beam under a tip load of $P = 100$ lb and curved-beam angle $\phi_n = 90°$, $n = 20$.

i	$\bar{\varepsilon}_i$, $\times 10^{-4}$ in/in (inner)	ε_i , $\times 10^{-4}$ in/in (outer)	u_i, in. (Nastran)	v_i, in. (Nastran)	d_i, $\equiv \sqrt{u_i^2 + v_i^2}$	$r_i^{(N)}$, in. (Nastran) [eq. (29)]	c_i, in. (Given)	r_i, in. (Disp. Theory) [eq. (15)]	r_i, in. (Disp. Theory) [eq. (16)]
0	-4.79975	4.74979	0.00000	0.00000	0.00000	0.00000	1.00524	0.00000	0.00000
1	-4.78495	4.73514	-0.00025	0.00596	0.00597	0.00597	1.00420	0.00600	0.00600
2	-4.74066	4.69131	-0.00236	0.02368	0.02380	0.02380	1.00530	0.02396	0.02398
3	-4.66713	4.61855	-0.00815	0.05272	0.05335	0.05335	1.00538	0.05377	0.05380
4	-4.56483	4.51731	-0.01934	0.09238	0.09438	0.09438	1.00441	0.09523	0.09528
5	-4.43439	4.38823	-0.03754	0.14168	0.14657	0.14657	1.00454	0.14811	0.14819
6	-4.27661	4.23209	-0.06417	0.19940	0.20947	0.20947	1.00588	0.21206	0.21218
7	-4.09245	4.04986	-0.10042	0.26412	0.28257	0.28257	1.00491	0.28670	0.28685
8	-3.88308	3.84266	-0.14729	0.33425	0.36526	0.36526	1.00518	0.37155	0.37175
9	-3.64975	3.61176	-0.20549	0.40805	0.45687	0.45687	1.00551	0.46610	0.46635
10	-3.39393	3.35860	-0.27546	0.48373	0.55666	0.55667	1.00444	0.56976	0.57006
11	-3.11718	3.08473	-0.35733	0.55940	0.66379	0.66379	1.00645	0.68189	0.68225
12	-2.82122	2.79185	-0.45096	0.63321	0.77738	0.77739	1.00535	0.80180	0.80222
13	-2.50786	2.48175	-0.55593	0.70333	0.89651	0.89652	1.00601	0.92874	0.92923
14	-2.17903	2.15635	-0.67151	0.76805	1.02021	1.02022	1.00461	1.06195	1.06250
15	-1.83677	1.81765	-0.79673	0.82577	1.14746	1.14748	1.00546	1.20060	1.20122
16	-1.48319	1.46776	-0.93036	0.87507	1.27723	1.27725	1.00339	1.34385	1.34454
17	-1.12047	1.10880	-1.07100	0.91473	1.40846	1.40848	1.00448	1.49081	1.49158
18	-0.75083	0.74302	-1.21705	0.94377	1.54010	1.54012	1.00671	1.64057	1.64141
19	-0.37657	0.37265	-1.36677	0.96149	1.67108	1.67111	1.01333	1.79220	1.79312
20	-0.00098	0.00098	-1.51836	0.96745	1.80038	1.80041	1.00000	1.94475	1.94575

Table E4. Nastran-generated surface strain and deflection data, and theoretical deflection data for the cantilever curved beam under a tip load of $P = 100$ lb and curved-beam angle $\phi_n = 135°$, $n = 20$.

i	$\bar{\varepsilon}_i$,$\times 10^{-4}$ in/in (inner)	ε_i ,$\times 10^{-4}$ in/in (outer)	u_i, in. (Nastran)	v_i, in. (Nastran)	d_i, $\equiv \sqrt{u_i^2 + v_i^2}$	$r_i^{(N)}$, in. (Nastran) [eq. (29)]	c_i, in. (Given)	r_i, in. (Disp. Theory) [eq. (15)]	r_i, in. (Disp. Theory) [eq. (16)]
0	-2.26954	2.23216	0.00000	0.00000	0.00000	0.00000	1.00889	0.00000	0.00000
1	-2.51940	2.48021	-0.00018	0.00289	0.00290	0.00290	1.00800	0.00294	0.00294
2	-2.73539	2.69283	-0.00179	0.01187	0.01200	0.01200	1.00921	0.01215	0.01216
3	-2.91345	2.86812	-0.00642	0.02707	0.02782	0.02782	1.00692	0.02818	0.02821
4	-3.05112	3.00365	-0.01568	0.04822	0.05071	0.05071	1.00826	0.05147	0.05154
5	-3.14649	3.09754	-0.03119	0.07465	0.08090	0.08090	1.00800	0.08237	0.08247
6	-3.19825	3.14849	-0.05438	0.10528	0.11849	0.11850	1.00787	0.12112	0.12127
7	-3.20566	3.15579	-0.08651	0.13866	0.16343	0.16343	1.00785	0.16785	0.16806
8	-3.16864	3.11934	-0.12846	0.17308	0.21554	0.21554	1.00795	0.22259	0.22286
9	-3.08768	3.03964	-0.18076	0.20654	0.27447	0.27447	1.00816	0.28523	0.28557
10	-2.96393	2.91781	-0.24351	0.23697	0.33978	0.33978	1.00680	0.35557	0.35600
11	-2.79908	2.75553	-0.31632	0.26220	0.41086	0.41086	1.00719	0.43332	0.43384
12	-2.59543	2.55505	-0.39836	0.28019	0.48703	0.48703	1.00775	0.51806	0.51868
13	-2.35580	2.31915	-0.48833	0.28904	0.56746	0.56746	1.00855	0.60929	0.61001
14	-2.08351	2.05109	-0.58454	0.28714	0.65126	0.65126	1.00726	0.70639	0.70723
15	-1.78233	1.75460	-0.68496	0.27325	0.73745	0.73746	1.00850	0.80869	0.80964
16	-1.45645	1.43379	-0.78733	0.24653	0.82502	0.82503	1.01038	0.91542	0.91650
17	-1.11037	1.09310	-0.88919	0.20665	0.91289	0.91289	1.00909	1.02577	1.02697
18	-0.74891	0.73726	-0.98809	0.15379	0.99999	0.99999	1.00671	1.13887	1.14021
19	-0.37706	0.37120	-1.08161	0.08861	1.08523	1.08524	1.01333	1.25385	1.25531
20	-0.00147	0.00147	-1.16751	0.01227	1.16757	1.16759	1.00000	1.36976	1.37136

Table E5a. Nastran-generated surface strain and deflection data, and theoretical deflection data for the cantilever curved beam under a tip load of $P = 100$ lb and curved-beam angle $\phi_n = 180°$, $n = 20$.

i	$\bar{\varepsilon}_i$, $\times 10^{-4}$ in/in (inner)	ε_i, $\times 10^{-4}$ in/in (outer)	u_i, in. (Nastran)	v_i, in. (Nastran)	d_i, $\equiv \sqrt{u_i^2 + v_i^2}$	$r_i^{(N)}$, in. (Nastran) [eq. (29)]	c_i, in. (Given)	r_i, in. (Disp. Theory) [eq. (15)]	r_i, in. (Disp. Theory) [eq. (16)]
0	-0.00196	0.00196	0.00000	0.00000	0.00000	0.00000	1.00000	0.00000	0.00000
1	-0.37737	0.36957	-0.00001	0.00012	0.00012	0.00012	1.01333	0.00016	0.00016
2	-0.74545	0.73004	-0.00026	0.00114	0.00117	0.00117	1.01351	0.00126	0.00126
3	-1.09517	1.07254	-0.00137	0.00381	0.00405	0.00405	1.01383	0.00420	0.00422
4	-1.41792	1.38862	-0.00429	0.00856	0.00957	0.00957	1.01068	0.00987	0.00990
5	-1.70577	1.67052	-0.01019	0.01546	0.01852	0.01852	1.01183	0.01906	0.01911
6	-1.95161	1.91128	-0.02028	0.02407	0.03147	0.03147	1.01036	0.03249	0.03258
7	-2.14939	2.10497	-0.03570	0.03350	0.04896	0.04896	1.01177	0.05078	0.05090
8	-2.29424	2.24684	-0.05729	0.04243	0.07129	0.07129	1.00881	0.07440	0.07458
9	-2.38261	2.33338	-0.08550	0.04919	0.09864	0.09864	1.01062	0.10375	0.10400
10	-2.41231	2.36246	-0.12026	0.05191	0.13099	0.13099	1.01048	0.13902	0.13935
11	-2.38261	2.33338	-0.16094	0.04870	0.16815	0.16815	1.01062	0.18029	0.18071
12	-2.29424	2.24683	-0.20632	0.03779	0.20975	0.20975	1.00881	0.22749	0.22801
13	-2.14937	2.10496	-0.25466	0.01776	0.25528	0.25528	1.01177	0.28040	0.28104
14	-1.95159	1.91126	-0.30377	-0.01235	0.30402	0.30402	1.01036	0.33866	0.33942
15	-1.70575	1.67051	-0.35122	-0.05289	0.35518	0.35518	1.01183	0.40177	0.40266
16	-1.41791	1.38861	-0.39448	-0.10355	0.40784	0.40785	1.01068	0.46912	0.47016
17	-1.09515	1.07252	-0.43110	-0.16332	0.46100	0.46100	1.01383	0.54000	0.54118
18	-0.74543	0.73003	-0.45895	-0.23058	0.51362	0.51362	1.01351	0.61359	0.61493
19	-0.37735	0.36955	-0.47637	-0.30314	0.56464	0.56465	1.01333	0.68904	0.69053
20	-0.00196	0.00196	-0.48229	-0.37847	0.61306	0.61306	1.00000	0.76542	0.76708

Additional Table for $\phi_n = 180°$ and $n = 10$

Table E5b. Nastran-generated surface strain and deflection data, and theoretical deflection data for the cantilever curved beam under a tip load of $P = 100$ lb and curved-beam angle $\phi_n = 180°$; $n = 10$.

i	$\bar{\varepsilon}_i$, $\times 10^{-4}$ in/in (inner)	ε_i, $\times 10^{-4}$ in/in (outer)	u_i, in. (Nastran)	v_i, in. (Nastran)	d_i, in. $\equiv \sqrt{u_i^2 + v_i^2}$	$r_i^{(N)}$, in. (Nastran) [eq. (29)]	c_i, in. (Calculated) [eq. (21)]	r_i, in. (Disp. Theory) [eq. (15)]	r_i, in. (Disp. Theory) [eq. (16)]
0	-0.00391	-0.00391	0.00000	0.00000	0.00000	0.00000	1.00000	0.00000	0.00000
1	-0.74538	0.73011	-0.00018	0.00114	0.00115	0.00115	1.01351	0.00125	0.00128
2	-1.41778	1.38876	-0.00399	0.00858	0.00946	0.00946	1.01068	0.00983	0.00998
3	-1.95142	1.91146	-0.01960	0.02417	0.03112	0.03112	1.01036	0.03236	0.03276
4	-2.29402	2.24706	-0.05607	0.04273	0.07050	0.07050	1.00881	0.07409	0.07492
5	-2.41208	2.36269	-0.11839	0.05258	0.12954	0.12954	1.01048	0.13842	0.13988
6	-2.29402	2.24705	-0.20373	0.03903	0.20743	0.20744	1.00881	0.22649	0.22876
7	-1.95140	1.91145	-0.30046	-0.01028	0.30064	0.30064	1.01036	0.33717	0.34043
8	-1.41777	1.38874	-0.39056	-0.10040	0.40326	0.40326	1.01068	0.46705	0.47143
9	-0.74536	0.73010	-0.45463	-0.22616	0.50778	0.50778	1.01351	0.61087	0.61646
10	-0.00391	-0.00391	-0.47783	-0.37268	0.60598	0.60598	1.00000	0.76203	0.76890

Appendix F
Nastran and Theoretical Data for Two-End Fixed Curved Beams

Table F1. Nastran-generated surface strain and deflection data, and theoretical deflection data for the two-end fixed straight beam under a central load of $P = 100$ lb and curved-beam angle $\phi_n = 0°$, $n = 20$.

i	$\overline{\varepsilon}_i$, $\times 10^{-4}$ in/in (inner)	ε_i, $\times 10^{-4}$ in/in (outer)	u_i, $\times 10^{-3}$, in. (Nastran)	v_i, $\times 10^{-3}$, in. (Nastran)	$r_i^{(N)}$, $\times 10^{-3}$ in. (Nastran)	c_i, in. (Given)	r_i^B $\times 10^{-3}$ in. (Disp. Theory) [eq.(17)]
0	-0.93752	0.93752	0.00000	0.00000	0.00000	1.00000	0.00000
1	-0.75002	0.75002	0.00000	1.11003	1.11003	1.00000	1.09378
2	-0.56251	0.56251	0.00000	4.09510	4.09510	1.00000	4.06260
3	-0.37501	0.37501	0.00000	8.48646	8.48646	1.00000	8.43770
4	-0.18750	0.18750	0.00000	13.81534	13.81534	1.00000	13.75032
5	0.00000	0.00000	0.00000	19.61299	19.61299	1.00000	19.53169
6	0.18750	-0.18750	0.00000	25.41063	25.41063	1.00000	25.31307
7	0.37501	-0.37501	0.00000	30.73952	30.73952	1.00000	30.62569
8	0.56251	-0.56251	0.00000	35.13087	35.13087	1.00000	35.00079
9	0.75002	-0.75002	0.00000	38.11595	38.11595	1.00000	37.96961
10*	0.93752	-0.93752	0.00000	39.22598	39.22598	1.00000	39.06338
11	0.75002	-0.75002	0.00000	38.11595	38.11595	1.00000	37.96961
12	0.56251	-0.56251	0.00000	35.13087	35.13087	1.00000	35.00079
13	0.37501	-0.37501	0.00000	30.73952	30.73952	1.00000	30.62569
14	0.18750	-0.18750	0.00000	25.41063	25.41063	1.00000	25.31307
15	0.00000	0.00000	0.00000	19.61299	19.61299	1.00000	19.53169
16	-0.18750	0.18750	0.00000	13.81534	13.81534	1.00000	13.75032
17	-0.37501	0.37501	0.00000	8.48646	8.48646	1.00000	8.43770
18	-0.56251	0.56251	0.00000	4.09510	4.09510	1.00000	4.06260
19	-0.75002	0.75002	0.00000	1.11003	1.11003	1.00000	1.09378
20	-0.93752	0.93752	0.00000	0.00000	0.00000	1.00000	0.00000

*Beam center

Table F2a. Nastran-generated surface strain and deflection data, and theoretical deflection data for the two-end fixed curved beam under a central load of $P = 100$ lb and curved-beam angle $\phi_n = 45°$, $n = 20$.

i	$\overline{\varepsilon}_i$, $\times 10^{-4}$ in/in (inner)	ε_i, $\times 10^{-4}$ in/in (outer)	$r_i^{(N)}$, $\times 10^{-3}$ in. (Nastran-radial)	$\delta\phi_i$ $\times 10^{-3}$ rad (Nastran-tangential)	c_i, in. (Given)	r_i^B, $\times 10^{-3}$ in. (Disp. Theory) [eq. (17)]	$\hat{r}_i$, $\times 10^{-3}$ in. (Corrected) [eq. (33)]
0	0.13191	-0.24638	0.00000	0.00000	1.00000	0.00000	0.00000
1	-0.00292	-0.11185	-0.19143	-0.03238	1.00000	-0.18173	-0.18123
2	-0.10391	-0.01139	-0.52888	-0.07530	1.00000	-0.51496	-0.51296
3	-0.17098	0.05533	-0.75985	-0.12949	1.00000	-0.74583	-0.74134
4	-0.20388	0.08806	-0.71687	-0.18744	1.00000	-0.70590	-0.69792
5	-0.20257	0.08675	-0.31799	-0.23673	1.00000	-0.31252	-0.30004
6	-0.16714	0.05151	0.43292	-0.26342	1.00000	0.43107	0.44905
7	-0.09755	-0.01772	1.44622	-0.25540	1.00000	1.43581	1.46027
8	0.00626	-0.12099	2.54676	-0.20575	1.00000	2.52679	2.55874
9	0.14383	-0.25784	3.47441	-0.11611	1.00000	3.44331	3.48375
10*	0.31479	-0.42840	3.88487	0.00000	1.00000	3.83972	3.88964
11	0.14385	-0.25785	3.47441	0.11611	1.00000	3.44325	3.48375
12	0.00629	-0.12102	2.54676	0.20575	1.00000	2.52663	2.55874
13	-0.09753	-0.01774	1.44622	0.25540	1.00000	1.43549	1.46027
14	-0.16720	0.05156	0.43292	0.26342	1.00000	0.43056	0.44905
15	-0.20263	0.08681	-0.31799	0.23673	1.00000	-0.31310	-0.30004
16	-0.20389	0.08806	-0.71687	0.18744	1.00000	-0.70644	-0.69792
17	-0.17101	0.05536	-0.75985	0.12949	1.00000	-0.74627	-0.74134
18	-0.10395	-0.01135	-0.52888	0.07530	1.00000	-0.51524	-0.51296
19	-0.00284	-0.11193	-0.19143	0.03238	1.00000	-0.18180	-0.18123
20	0.13197	-0.24643	0.00000	0.00000	1.00000	0.00000	0.00000

*Beam center

Table F2b. Nastran-generated surface strain and deflection data, and theoretical deflection data for the two-end fixed curved beam under a central load of $P = 100$ lb and curved-beam angle $\phi_n = 45°$, $n = 10$.

i	$\overline{\varepsilon}_i$, $\times 10^{-4}$ in/in (inner)	ε_i, $\times 10^{-4}$ in/in (outer)	$r_i^{(N)}$, $\times 10^{-3}$ in. (Nastran-radial)	$\delta\phi_i$ $\times 10^{-3}$ rad (Nastran-tangential)	c_i, in. (Given)	r_i^B, $\times 10^{-3}$ in. (Disp. Theory) [eq. (17)]	$\hat{r}_i$, $\times 10^{-3}$ in. (Corrected) [eq. (33)]
0	0.12339	-0.23820	0.00000	0.00000	1.00000	0.00000	0.00000
1	-0.11237	-0.00288	0.52890	-0.07821	1.00000	-0.51540	-0.51341
2	-0.21237	0.09660	0.71755	-0.18506	1.00000	-0.70716	-0.69918
3	-0.17558	0.06001	-0.43035	-0.25429	1.00000	0.42889	0.44685
4	-0.00225	-0.11242	-2.54169	-0.19520	1.00000	2.52338	2.55530
5*	0.30607	-0.42011	-3.87851	0.00000	1.00000	3.83572	3.88559
6	-0.00225	-0.11242	-2.54169	0.19520	1.00000	2.52338	2.55530
7	-0.17558	0.06001	-0.43035	0.25429	1.00000	0.42889	0.44685
8	-0.21237	0.09660	0.71755	0.18506	1.00000	-0.70716	-0.69918
9	-0.11237	-0.00288	0.52890	0.07821	1.00000	-0.51540	-0.51341
10	0.12339	-0.23820	0.00000	0.00000	1.00000	0.00000	0.00000

*Beam center

Table F3. Nastran-generated surface strain and deflection data, and theoretical deflection data for the two-end fixed curved beam under a central load of $P = 100$ lb; and curved-beam angle $\phi_n = 90°$, $n = 20$.

i	$\bar{\varepsilon}_i$, $\times 10^{-4}$ in/in (inner)	ε_i , $\times 10^{-4}$ in/in (outer)	$r_i^{(N)}$, $\times 10^{-3}$ in. (Nastran-radial)	$\delta\phi_i$ $\times 10^{-3}$ rad (Nastran-tangential)	c_i, in. (Given)	r_i^B, $\times 10^{-3}$ in. (Disp. Theory) [eq. (17)]	$\hat{r}_i$, $\times 10^{-3}$ in. (Corrected) [eq. (33)]
0	0.19795	-0.25582	0.00000	0.00000	1.12753	0.00000	0.00000
1	0.05178	-0.11033	-0.23461	-0.02369	1.36118	-0.16063	-0.15909
2	-0.06014	0.00043	-0.68037	-0.07445	0.01420	-0.61881	-0.61264
3	-0.13669	0.07619	-1.05673	-0.15776	0.71580	-1.05557	-1.04169
4	-0.17740	0.11648	-1.17139	-0.26052	0.79271	-1.16661	-1.14193
5	-0.18204	0.12106	-0.92258	-0.35806	0.79881	-0.91715	-0.87860
6	-0.15055	0.08990	-0.30035	-0.42134	0.74777	-0.29651	-0.24100
7	-0.08314	0.02319	0.61333	-0.42415	0.43619	0.63242	0.70798
8	0.01977	-0.07865	1.64550	-0.35028	1.59825	1.64473	1.74342
9	0.15757	-0.21501	2.53436	-0.20063	1.15417	2.48607	2.61097
10*	0.32889	-0.38552	2.93245	0.00000	1.07927	2.86044	3.01464
11	0.15757	-0.21501	2.53436	0.20063	1.15417	2.48609	2.61097
12	0.01978	-0.07865	1.64550	0.35028	1.59809	1.64475	1.74342
13	-0.08314	0.02319	0.61333	0.42415	0.43619	0.63244	0.70798
14	-0.15055	0.08990	-0.30035	0.42134	0.74777	-0.29649	-0.24100
15	-0.18204	0.12106	-0.92258	0.35806	0.79881	-0.91714	-0.87860
16	-0.17741	0.11648	-1.17139	0.26052	0.79268	-1.16659	-1.14193
17	-0.13669	0.07618	-1.05673	0.15776	0.71574	-1.05555	-1.04169
18	-0.06013	0.00043	-0.68037	0.07445	0.01420	-0.61880	-0.61264
19	0.05178	-0.11033	-0.23461	0.02369	1.36118	-0.16063	-0.15909
20	0.19794	-0.25581	0.00000	0.00000	1.12754	0.00000	0.00000

*Beam center

Table F4. Nastran-generated surface strain and deflection data, and theoretical deflection data for the two-end fixed curved beam under a central load of $P = 100$ lb and curved-beam angle $\phi_n = 135°$, $n = 20$.

i	$\bar{\varepsilon}_i$, $\times 10^{-4}$ in/in (inner)	ε_i, $\times 10^{-4}$ in/in (outer)	$r_i^{(N)}$, $\times 10^{-3}$ in. (Nastran-radial)	$\delta\phi_i$ $\times 10^{-3}$ ra (Nastran-tangential)	c_i, in. (Given)	r_i^B, $\times 10^{-3}$ in. (Disp. Theory) [eq. (17)]	$\hat{r}_i$, $\times 10^{-3}$ in. (Corrected) [eq. (33)]
0	0.22350	-0.26105	0.00000	0.00000	1.07750	0.00000	0.00000
1	0.07214	-0.11074	-0.25180	-0.02425	1.21107	-0.18381	-0.18046
2	-0.04549	0.00506	-0.73812	-0.09255	0.20020	-0.67797	-0.66460
3	-0.12710	0.08540	-1.16178	-0.21491	0.80377	-1.15231	-1.12223
4	-0.17155	0.12916	-1.31537	-0.37155	0.85903	-1.32568	-1.27221
5	-0.17822	0.13573	-1.08703	-0.52389	0.86466	-1.12905	-1.04549
6	-0.14704	0.10503	-0.46340	-0.62593	0.83334	-0.54632	-0.42601
7	-0.07842	0.03748	0.46984	-0.63597	0.64676	0.35130	0.51507
8	0.02667	-0.06598	1.53034	-0.52809	1.42429	1.35573	1.56963
9	0.16679	-0.20392	2.44388	-0.30332	1.10016	2.20704	2.47776
10*	0.33925	-0.37515	2.85180	0.00000	1.05025	2.58618	2.92040
11	0.16679	-0.20391	2.44388	0.30332	1.10014	2.20702	2.47776
12	0.02667	-0.06597	1.53034	0.52809	1.42422	1.35568	1.56963
13	-0.07843	0.03749	0.46984	0.63597	0.64683	0.35125	0.51507
14	-0.14704	0.10503	-0.46340	0.62593	0.83334	-0.54635	-0.42601
15	-0.17823	0.13573	-1.08703	0.52389	0.86463	-1.12905	-1.04549
16	-0.17154	0.12915	-1.31537	0.37155	0.85902	-1.32566	-1.27221
17	-0.12709	0.08540	-1.16178	0.21491	0.80380	-1.15229	-1.12223
18	-0.04549	0.00506	-0.73812	0.09255	0.20020	-0.67795	-0.66460
19	0.07214	-0.11074	-0.25180	0.02425	1.21107	-0.18380	-0.18046
20	0.22350	-0.26105	0.00000	0.00000	1.07750	0.00000	0.00000

*Beam center

Table F5. Nastran-generated surface strain and deflection data, and theoretical deflection data for the two-end fixed curved beam under a central load of $P = 100$ lb and curved-beam angle $\phi_n = 180°$, $n = 20$.

i	$\bar{\varepsilon}_i$, $\times 10^{-4}$ in/in (inner)	ε_i, $\times 10^{-4}$ in/in (outer)	$r_i^{(N)}$, $\times 10^{-3}$ in. (Nastran-radial)	$\delta\phi_i$ $\times 10^{-3}$ rad (Nastran-tangential)	c_i, in. (calculated) [eq. (21)]	r_i^B, $\times 10^{-3}$ in. (Disp. Theory) [eq. (17)]	$\hat{r}_i$, $\times 10^{-3}$ in. (Corrected) [eq. (33)]
0	0.24470	-0.27142	0.00000	0.00000	1.05177	0.00000	0.00000
1	0.08793	-0.11611	-0.26919	-0.02788	1.13811	-0.21024	-0.20429
2	-0.03616	0.00541	-0.79530	-0.11908	0.26028	-0.75686	-0.73305
3	-0.12360	0.09105	-1.26083	-0.28888	0.84836	-1.28969	-1.23612
4	-0.17226	0.13870	-1.43970	-0.50975	0.89208	-1.52132	-1.42610
5	-0.18093	0.14720	-1.20807	-0.72662	0.89721	-1.36840	-1.21961
6	-0.14940	0.11631	-0.55037	-0.87343	0.87547	-0.80966	-0.59540
7	-0.07844	0.04682	0.43981	-0.89028	0.74757	0.07975	0.37139
8	0.03020	-0.05957	1.56393	-0.74027	1.32717	1.09384	1.47475
9	0.17384	-0.20024	2.52770	-0.42529	1.07057	1.96275	2.44483
10*	0.34796	-0.37271	2.95484	0.00000	1.03434	2.34952	2.94469
11	0.17384	-0.20024	2.52770	0.42529	1.07057	1.96276	2.44483
12	0.03020	-0.05957	1.56393	0.74027	1.32717	1.09386	1.47475
13	-0.07844	0.04682	0.43981	0.89028	0.74757	0.07979	0.37139
14	-0.14940	0.11631	-0.55037	0.87343	0.87547	-0.80960	-0.59540
15	-0.18093	0.14719	-1.20807	0.72662	0.89717	-1.36834	-1.21961
16	-0.17226	0.13870	-1.43970	0.50975	0.89208	-1.52126	-1.42610
17	-0.12360	0.09105	-1.26083	0.28888	0.84836	-1.28963	-1.23612
18	-0.03615	0.00541	-0.79530	0.11908	0.26035	-0.75681	-0.73305
19	0.08794	-0.11612	-0.26919	0.02788	1.13810	-0.21021	-0.20429
20	0.24470	-0.27141	0.00000	0.00000	1.05175	0.00000	0.00000

*Beam center

Appendix G
Nastran and Theoretical Data for Two-End Simply Supported Curved Beams

Table G1. Nastran-generated surface strain and deflection data, and theoretically predicted deflection data for the two-end simply supported straight beam under a central load of $P = 100$ lb and curved-beam angle $\phi_n = 0°$, $n = 20$.

i	$\bar{\varepsilon}_i$, $\times 10^{-4}$ in/in (inner)	ε_i, $\times 10^{-4}$ in/in (outer)	u_i, $\times 10^{-3}$ in. (Nastran)	v_i, $\times 10^{-3}$ in. (Nastran)	$r_i^{(N)}$, $\times 10^{-3}$ in. (Nastran)	c_i, in. (Given)	$r_i^B \times 10^{-3}$ in. (Disp. Theory) [eq. (17)]
0	0.00000	0.00000	0.00000	0.00000	0.00000	1.00000	0.00000
1	-0.18750	0.18750	0.00000	23.37621	23.37621	1.00000	23.35994
2	-0.37501	0.37501	0.00000	46.28365	46.28365	1.00000	46.25112
3	-0.56251	0.56251	0.00000	68.25358	68.25358	1.00000	68.20478
4	-0.75002	0.75002	0.00000	88.81722	88.81722	1.00000	88.75217
5	-0.93752	0.93752	0.00000	107.50580	107.50580	1.00000	107.42450
6	-1.12503	1.12503	0.00000	123.85060	123.85060	1.00000	123.75304
7	-1.31253	1.31253	0.00000	137.38280	137.38280	1.00000	137.26900
8	-1.50004	1.50004	0.00000	147.63370	147.63370	1.00000	147.50363
9	-1.68754	1.68754	0.00000	154.13450	154.13450	1.00000	153.98817
10*	-1.87505	1.87505	0.00000	156.41640	156.41640	1.00000	156.25385
11	-1.68754	1.68754	0.00000	154.13450	154.13450	1.00000	153.98817
12	-1.50004	1.50004	0.00000	147.63370	147.63370	1.00000	147.50363
13	-1.31253	1.31253	0.00000	137.38280	137.38280	1.00000	137.26900
14	-1.12503	1.12503	0.00000	123.85060	123.85060	1.00000	123.75304
15	-0.93752	0.93752	0.00000	107.50580	107.50580	1.00000	107.42450
16	-0.75002	0.75002	0.00000	88.81722	88.81722	1.00000	88.75217
17	-0.56251	0.56251	0.00000	68.25358	68.25358	1.00000	68.20478
18	-0.37501	0.37501	0.00000	46.28365	46.28365	1.00000	46.25112
19	-0.18750	0.18750	0.00000	23.37621	23.37621	1.00000	23.35994
20	0.00000	0.00000	0.00000	0.00000	0.00000	1.00000	0.00000

*Beam center

Table G2. Nastran-generated surface strain and deflection data, and theoretically predicted deflection data for the two-end simply supported curved beam under a central load of $P = 100$ lb and curved-beam angle $\phi_n = 45^\circ$, $n = 20$.

i	$\bar{\varepsilon}_i$, $\times 10^{-4}$ in/in (inner)	ε_i, $\times 10^{-4}$ in/in (outer)	$r_i^{(N)}$, $\times 10^{-3}$ in. (Nastran-radial)	$\delta\phi_i$ $\times 10^{-3}$ rad (Nastran-tangential)	c_i, in. (Given)	r_i^B, $\times 10^{-3}$ in. (Disp. Theory) [eq. (17)]	$\hat{r}_i$, $\times 10^{-3}$ in. (Corrected) [eq. (33)]
0	-0.04969	-0.04969	0.00000	0.00000	1.00000	0.00000	0.00000
1	0.04059	-0.14018	-0.79492	-0.04046	1.00000	-0.79405	-0.79344
2	0.10149	-0.20139	-1.37143	-0.10795	1.00000	-1.37267	-1.37026
3	0.13303	-0.23310	-1.57607	-0.19084	1.00000	-1.58208	-1.57666
4	0.13518	-0.23526	-1.32951	-0.27293	1.00000	-1.34261	-1.33297
5	0.10792	-0.20786	-0.62676	-0.33636	1.00000	-0.64884	-0.63377
6	0.05131	-0.15094	0.46283	-0.36454	1.00000	0.43040	0.45210
7	-0.03458	-0.06461	1.79573	-0.34505	1.00000	1.75212	1.78165
8	-0.14961	0.05102	3.15472	-0.27257	1.00000	3.09939	3.13797
9	-0.29360	0.19577	4.24952	-0.15174	1.00000	4.18172	4.23053
10*	-0.46657	0.36916	4.71772	0.00000	1.00000	4.63543	4.69569
11	-0.29360	0.19577	4.24952	0.15174	1.00000	4.18172	4.23053
12	-0.14961	0.05102	3.15472	0.27257	1.00000	3.09939	3.13797
13	-0.03458	-0.06461	1.79573	0.34505	1.00000	1.75212	1.78165
14	0.05131	-0.15094	0.46283	0.36454	1.00000	0.43040	0.45210
15	0.10792	-0.20786	-0.62676	0.33636	1.00000	-0.64884	-0.63377
16	0.13518	-0.23526	-1.32951	0.27293	1.00000	-1.34261	-1.33297
17	0.13303	-0.23310	-1.57607	0.19084	1.00000	-1.58208	-1.57666
18	0.10149	-0.20139	-1.37143	0.10795	1.00000	-1.37267	-1.37026
19	0.04059	-0.14018	-0.79492	0.04046	1.00000	-0.79405	-0.79344
20	-0.04969	-0.04969	0.00000	0.00000	1.00000	0.00000	0.00000

*Beam center

Table G3. Nastran-generated surface strain and deflection data, and theoretically predicted deflection data for the two-end simply supported curved beam under a central load of $P = 100$ lb and curved-beam angle $\phi_n = 90°$, $n = 20$.

i	$\bar{\varepsilon}_i$, $\times 10^{-4}$ in/in (inner)	ε_i, $\times 10^{-4}$ in/in (outer)	$r_i^{(N)}$, $\times 10^{-3}$ in. (Nastran-radial)	$\delta\phi_i$ $\times 10^{-3}$ rad (Nastran-tangential)	c_i, in. (Given)	r_i^B, $\times 10^{-3}$ in. (Disp. Theory) [eq. (17)]	$\hat{r}_i$, $\times 10^{-3}$ in. (Corrected) [eq. (33)]
0	-0.02520	-0.02520	0.00000	0.00000	1.00000	0.00000	0.00000
1	0.06862	-0.11943	-0.95549	-0.05015	1.00000	-0.96397	-0.96189
2	0.13237	-0.18385	-1.67920	-0.16648	1.00000	-1.70185	-1.69355
3	0.16594	-0.21778	-2.00679	-0.32424	1.00000	-2.05109	-2.03241
4	0.16914	-0.22100	-1.85202	-0.48884	1.00000	-1.92607	-1.89286
5	0.14193	-0.19351	-1.20783	-0.62202	1.00000	-1.31865	-1.26676
6	0.08449	-0.13547	-0.14643	-0.68808	1.00000	-0.29820	-0.22348
7	-0.00282	-0.04724	1.18157	-0.66006	1.00000	0.98881	1.09052
8	-0.11948	0.07065	2.54901	-0.52587	1.00000	2.31973	2.45257
9	-0.26476	0.21745	3.65485	-0.29416	1.00000	3.39708	3.56521
10*	-0.43825	0.39179	4.12791	0.00000	1.00000	3.85040	4.05796
11	-0.26476	0.21745	3.65485	0.29416	1.00000	3.39708	3.56521
12	-0.11948	0.07065	2.54901	0.52587	1.00000	2.31973	2.45257
13	-0.00282	-0.04724	1.18157	0.66006	1.00000	0.98881	1.09052
14	0.08449	-0.13547	-0.14643	0.68808	1.00000	-0.29820	-0.22348
15	0.14193	-0.19351	-1.20783	0.62202	1.00000	-1.31865	-1.26676
16	0.16914	-0.22100	-1.85202	0.48884	1.00000	-1.92607	-1.89286
17	0.16594	-0.21778	-2.00679	0.32424	1.00000	-2.05109	-2.03241
18	0.13237	-0.18385	-1.67920	0.16648	1.00000	-1.70185	-1.69355
19	0.06862	-0.11943	-0.95549	0.05015	1.00000	-0.96397	-0.96189
20	-0.02520	-0.02520	0.00000	0.00000	1.00000	0.00000	0.00000

*Beam center

Table G4. Nastran-generated surface strain and deflection data, and theoretically predicted deflection data for two-end simply supported curved beam under central load of $P = 100$ lb; curved-beam angle $\phi_n = 135°$, $n = 20$.

i	$\overline{\varepsilon}_i$, $\times 10^{-4}$ in/in (inner)	ε_i, $\times 10^{-4}$ in/in (outer)	$r_i^{(N)}$, $\times 10^{-3}$ in. (Nastran-radial)	$\delta\phi_i$ $\times 10^{-3}$ rad (Nastran-tangential)	c_i, in. (Given)	r_i^B, $\times 10^{-3}$ in. (Disp. Theory) [eq. (17)]	$\hat{r}_i$, $\times 10^{-3}$ in. (Corrected) [eq. (33)]
0	-0.01707	-0.01707	0.00000	0.00000	1.00000	0.00000	0.00000
1	0.08091	-0.11571	-1.05522	-0.07078	0.82301	-1.03304	-1.02805
2	0.14793	-0.18379	-1.85984	-0.25156	0.89190	-1.84494	-1.82495
3	0.18350	-0.21992	-2.23458	-0.50210	0.90972	-2.24362	-2.19865
4	0.18711	-0.22359	-2.08506	-0.76599	0.91118	-2.14003	-2.06008
5	0.15873	-0.19476	-1.40427	-0.98088	0.89807	-1.52502	-1.40010
6	0.09875	-0.13383	-0.27283	-1.08871	0.84917	-0.47006	-0.29018
7	0.00799	-0.04164	1.14310	-1.04602	0.32198	0.90653	1.15137
8	-0.11228	0.08054	2.59624	-0.83371	1.16461	2.31096	2.63075
9	-0.26040	0.23100	3.76477	-0.46626	1.05983	3.40541	3.81016
10*	-0.43505	0.40692	4.26094	0.00000	1.03341	3.86657	4.36625
11	-0.26040	0.23100	3.76477	0.46626	1.05983	3.40541	3.81016
12	-0.11228	0.08054	2.59624	0.83371	1.16461	2.31096	2.63075
13	0.00799	-0.04164	1.14310	1.04602	0.32198	0.90653	1.15137
14	0.09875	-0.13383	-0.27283	1.08871	0.84917	-0.47006	-0.29018
15	0.15873	-0.19476	-1.40427	0.98088	0.89807	-1.52502	-1.40010
16	0.18711	-0.22359	-2.08506	0.76599	0.91118	-2.14003	-2.06008
17	0.18350	-0.21992	-2.23458	0.50210	0.90972	-2.24362	-2.19865
18	0.14793	-0.18379	-1.85984	0.25156	0.89190	-1.84494	-1.82495
19	0.08091	-0.11571	-1.05522	0.07078	0.82301	-1.03304	-1.02805
20	-0.01707	-0.01707	0.00000	0.00000	1.00000	0.00000	0.00000

*Beam center

Table G5. Nastran-generated surface strain and deflection data, and theoretically predicted deflection data for the two-end simply supported curved beam under a central load of $P = 100$ lb and curved-beam angle $\phi_n = 180°$, $n = 20$.

i	$\bar{\varepsilon}_i$, $\times 10^{-4}$ in/in (inner)	ε_i, $\times 10^{-4}$ in/in (outer)	$r_i^{(N)}$, $\times 10^{-3}$ in. (Nastran-radial)	$\delta\phi_i$ $\times 10^{-3}$ rad (Nastran-tangential)	c_i, in. (Given)	r_i^B, $\times 10^{-3}$ in. (Disp. Theory) [eq. (17)]	$\hat{r}_i$, $\times 10^{-3}$ in. (Corrected) [eq. (33)]
0	-0.01309	-0.01309	0.00000	0.00000	1.00000	0.00000	0.00000
1	0.09104	-0.11815	-1.18721	-0.09999	0.87041	-1.18811	-1.17921
2	0.16291	-0.19153	-2.09448	-0.36529	0.91925	-2.13357	-2.09795
3	0.20137	-0.23081	-2.51935	-0.73573	0.93188	-2.63523	-2.55510
4	0.20549	-0.23501	-2.35497	-1.12677	0.93299	-2.59509	-2.45264
5	0.17515	-0.20403	-1.59508	-1.44501	0.92384	-2.00257	-1.78000
6	0.11110	-0.13863	-0.33442	-1.60397	0.88976	-0.93530	-0.61479
7	0.01493	-0.04043	1.23546	-1.53974	0.53938	0.46114	0.89739
8	-0.11101	0.08816	2.83489	-1.22549	1.11473	1.89966	2.46946
9	-0.26360	0.24398	4.10888	-0.68436	1.03865	3.03686	3.75801
10*	-0.44008	0.42219	4.64366	0.00000	1.02075	3.51465	4.40496
11	-0.26360	0.24398	4.10888	0.68436	1.03865	3.03686	3.75801
12	-0.11101	0.08816	2.83489	1.22549	1.11473	1.89966	2.46946
13	0.01493	-0.04043	1.23546	1.53974	0.53938	0.46114	0.89739
14	0.11110	-0.13863	-0.33442	1.60397	0.88976	-0.93530	-0.61479
15	0.17515	-0.20403	-1.59508	1.44501	0.92384	-2.00257	-1.78000
16	0.20549	-0.23501	-2.35497	1.12677	0.93299	-2.59509	-2.45264
17	0.20137	-0.23081	-2.51935	0.73573	0.93188	-2.63523	-2.55510
18	0.16291	-0.19153	-2.09448	0.36529	0.91925	-2.13357	-2.09795
19	0.09104	-0.11815	-1.18721	0.09999	0.87041	-1.18811	-1.17921
20	-0.01309	-0.01309	0.00000	0.00000	1.00000	0.00000	0.00000

*Beam center

Appendix H
Alternative Theta-Formulation

The Curvilinear Displacement Transfer Functions can also be formulated alternatively based on the deformed slope angle $\theta(s)$ measured from the *x*-axis (fig. 1). Equation (5) is duplicated below as equation (H1):

$$\frac{1}{R(s)} - \frac{1}{R_0} = \left[1 + \frac{c(s)}{R_0}\right]\frac{\varepsilon(s)}{c(s)} \tag{H1}$$

In view of figure 3, one can write equation (H2):

$$\frac{1}{R(s)} = \frac{d\theta(s)}{ds} \tag{H2}$$

In view of equation (H2), equation (H1) can be rewritten as equation (H3):

$$\frac{d\theta(s)}{ds} = \left[1 + \frac{c(s)}{R_0}\right]\frac{\varepsilon(s)}{c(s)} + \frac{1}{R_0} \tag{H3}$$

For the in-extensional beams $(s = x)$, $d\theta/ds$ in equation (H3) can be considered as $d\theta/dx$. The θ-formulation based on equation (H3) will then give slope angles and deflections in reference to the horizontal *x*-axis. The total deflections will then contain the initial displacements for forming the undeformed curved beam and also the strain-induced deflections.

Slope-Angle Equation in Recursive Form

The slope-angle equation can be obtained by piecewise integration of equation (H3) within each small domain $s_{i-1} \le s \le s_i$, assuming $c(s) \approx c = (c_{i-1} + c_i)/2 \ (i = 1,2,3,...,n)$ [eq. (10)], shown as equation (H4):

$$\int_{s_{i-1}}^{s} \frac{d\theta(s)}{ds} ds = \left(1 + \frac{c}{R_0}\right)\frac{1}{c}\int_{s_{i-1}}^{s} \varepsilon(s) ds + \frac{1}{R_0}\int_{s_{i-1}}^{s} ds \quad ; \quad (s_{i-1} \le s \le s_i) \tag{H4}$$

Using piecewise linear representation of strain distribution given by equation (H5):

$$\varepsilon(s) = \varepsilon_{i-1} - (\varepsilon_{i-1} - \varepsilon_i)\frac{s - s_{i-1}}{\Delta l} \quad ; \quad (s_{i-1} \le s \le s_i) \tag{H5}$$

equation (H4) can be piecewise integrated (process similar to Appendix A) within each small domain $s_{i-1} \le s \le s_i$ to yield equation (H6):

$$\theta(s)=\left(1+\frac{c}{R_0}\right)\frac{1}{c}\int_{s_{i-1}}^{s}\left[\varepsilon_{i-1}-(\varepsilon_{i-1}-\varepsilon_i)\frac{s-s_{i-1}}{\Delta l}\right]ds+\theta_{i-1}+\frac{s-s_{i-1}}{R_0}$$
$$=\frac{1}{c}\left(1+\frac{c}{R_0}\right)\left[\varepsilon_{i-1}(s-s_{i-1})-(\varepsilon_{i-1}-\varepsilon_i)\frac{(s-s_{i-1})^2}{2\Delta l}\right]+\theta_{i-1}+\frac{s-s_{i-1}}{R_0} \qquad (H6)$$
$$(s_{i-1}\le s\le s_i)$$

At the strain-sensing station s_i, one can write $(s_i-s_{i-1})\equiv\Delta l$, and equation (H6) yields the slope angle $\theta_i[\equiv\theta(s_i)]$ at the strain-sensing station s_i as equation (H7):

$$\theta_i=\underbrace{\left(1+\frac{c}{R_0}\right)\frac{\Delta l}{2c}(\varepsilon_{i-1}+\varepsilon_i)}_{\text{Strain-induced slope-angle increment}}+\underbrace{\theta_{i-1}}_{\substack{\text{Slope angle}\\ \text{at } s_{i-1}}}+\underbrace{\frac{\Delta l}{R_0}}_{\substack{\text{Initial slope}\\ \text{angle increment}}} \quad ; \quad (i=1,2,3,...,n) \qquad (H7)$$

Equation (H7) is the slope-angle equation in recursive form in reference to the *x*-axis.

Deflection Equation in Recursive Form

The curved deflection $\hat{y}(s)$ (measured from the *x*-axis) can be obtained by piecewise integration of slope equation (H6) within each small domain $(s_{i-1}\le s\le s_i)$ as equation (H8):

$$\hat{y}(s)-\hat{y}_{i-1}\equiv\int_{s_{i-1}}^{s}\theta(s)ds$$
$$=\frac{1}{c}\left(1+\frac{c}{R_0}\right)\int_{s_{i-1}}^{s}\left[\varepsilon_{i-1}(s-s_{i-1})-(\varepsilon_{i-1}-\varepsilon_i)\frac{(s-s_{i-1})^2}{2\Delta l}\right]ds+\int_{s_{i-1}}^{s}\theta_{i-1}\,ds+\int_{s_{i-1}}^{s}\frac{s-s_{i-1}}{R_0}ds \qquad (H8)$$
$$=\frac{1}{c}\left(1+\frac{c}{R_0}\right)\left[\varepsilon_{i-1}\frac{(s-s_{i-1})^2}{2}-(\varepsilon_{i-1}-\varepsilon_i)\frac{(s-s_{i-1})^3}{6\Delta l}\right]+\theta_{i-1}(s-s_{i-1})+\frac{(s-s_{i-1})^2}{2R_0}$$
$$(s_{i-1}\le s\le s_i)$$

At the strain-sensing station s_i, one can write $(s_i-s_{i-1})\equiv\Delta l$, and equation (H8) yields the curved deflection $\hat{y}_i[\equiv\hat{y}(s_i)]$ at the strain-sensing station s_i as equation (H9):

$$\hat{y}_i=\underbrace{\left(1+\frac{c}{R_0}\right)\frac{(\Delta l)^2}{6c}(2\varepsilon_{i-1}+\varepsilon_i)}_{\text{Strain-induced deflection increment}}+\underbrace{\hat{y}_{i-1}}_{\substack{\text{deflection}\\ \text{at } s_{i-1}}}+\underbrace{(\Delta l)\theta_{i-1}}_{\substack{\text{Deflection}\\ \text{due to } \theta_{i-1}}}+\underbrace{\frac{(\Delta l)^2}{2R_0}}_{\substack{\text{Initial}\\ \text{displacement}}} \quad ; \quad (i=1,2,3,...,n) \qquad (H9)$$

Equation (H9) is the curved deflection equation in recursive form in reference to the *x*-axis.

Deflection Equation in Summation Form

Combining equations (H6) and (H9) for different indices yields equations (H10)–(H13):

For $i = 1$:

$$\hat{y}_1 = \left(1 + \frac{c}{R_0}\right)\frac{(\Delta l)^2}{6c}\left(2\varepsilon_0 + \varepsilon_1\right) + \hat{y}_0 + (\Delta l)\theta_0 + \frac{(\Delta l)^2}{2R_0} \tag{H10}$$

For $i = 2$:

$$\begin{aligned}
\hat{y}_2 &= \left(1 + \frac{c}{R_0}\right)\frac{(\Delta l)^2}{6c}\left(2\varepsilon_1 + \varepsilon_2\right) + \hat{y}_1 + (\Delta l)\theta_1 + \frac{(\Delta l)^2}{2R_0} \\
&= \left(1 + \frac{c}{R_0}\right)\frac{(\Delta l)^2}{6c}\left(2\varepsilon_1 + \varepsilon_2\right) + \underbrace{\left(1 + \frac{c}{R_0}\right)\frac{(\Delta l)^2}{6c}\left(2\varepsilon_0 + \varepsilon_1\right) + \hat{y}_0 + (\Delta l)\theta_0 + \frac{(\Delta l)^2}{2R_0}}_{\hat{y}_1} \\
&\quad + \underbrace{\left(1 + \frac{c}{R_0}\right)\frac{(\Delta l)^2}{2c}\left(\varepsilon_0 + \varepsilon_1\right) + (\Delta l)\theta_0 + \frac{(\Delta l)^2}{R_0}}_{(\Delta l)\theta_1} + \frac{(\Delta l)^2}{2R_0} \\
&= \left(1 + \frac{c}{R_0}\right)\frac{(\Delta l)^2}{6c}\left(2\varepsilon_1 + \varepsilon_2\right) + \left(1 + \frac{c}{R_0}\right)\frac{(\Delta l)^2}{6c}\left(2\varepsilon_0 + \varepsilon_1\right) \\
&\quad + \left(1 + \frac{c}{R_0}\right)\frac{(\Delta l)^2}{2c}\left(\varepsilon_0 + \varepsilon_1\right) + \hat{y}_0 + 2(\Delta l)\theta_0 + \frac{(2\Delta l)^2}{2R_0}
\end{aligned} \tag{H11}$$

For $i = 3$:

$$
\begin{aligned}
\hat{y}_3 &= \left(1+\frac{c}{R_0}\right)\frac{(\Delta l)^2}{6c}\left(2\varepsilon_2+\varepsilon_3\right)+\hat{y}_2+(\Delta l)\theta_2+\frac{(\Delta l)^2}{2R_0} \\
&= \left(1+\frac{c}{R_0}\right)\frac{(\Delta l)^2}{6c}\left(2\varepsilon_2+\varepsilon_3\right) \\
&\quad \underbrace{+\left\{\begin{array}{l}\left(1+\frac{c}{R_0}\right)\frac{(\Delta l)^2}{6c}\left(2\varepsilon_1+\varepsilon_2\right)+\left(1+\frac{c}{R_0}\right)\frac{(\Delta l)^2}{6c}\left(2\varepsilon_0+\varepsilon_1\right) \\ \quad +\left(1+\frac{c}{R_0}\right)\frac{(\Delta l)^2}{2c}\left(\varepsilon_0+\varepsilon_1\right)+\frac{(2\Delta l)^2}{2R_0}+\hat{y}_0+2(\Delta l)\theta_0\end{array}\right\}}_{\hat{y}_2} \\
&\quad +\underbrace{\left(1+\frac{c}{R_0}\right)\frac{(\Delta l)^2}{2c}\left(\varepsilon_1+\varepsilon_2\right)+\left(1+\frac{c}{R_0}\right)\frac{(\Delta l)^2}{2c}\left(\varepsilon_0+\varepsilon_1\right)+(\Delta l)\theta_0+2\frac{(\Delta l)^2}{R_0}}_{(\Delta l)\theta_2}+\frac{(\Delta l)^2}{2R_0} \\
&= \left(1+\frac{c}{R_0}\right)\frac{(\Delta l)^2}{6c}\left(2\varepsilon_2+\varepsilon_3\right)+\left(1+\frac{c}{R_0}\right)\frac{(\Delta l)^2}{6c}\left(2\varepsilon_1+\varepsilon_2\right)+\left(1+\frac{c}{R_0}\right)\frac{(\Delta l)^2}{6c}\left(2\varepsilon_0+\varepsilon_1\right) \\
&\quad +\left(1+\frac{c}{R_0}\right)\frac{(\Delta l)^2}{2c}\left(\varepsilon_1+\varepsilon_2\right)+2\left(1+\frac{c}{R_0}\right)\frac{(\Delta l)^2}{2c}\left(\varepsilon_0+\varepsilon_1\right)+\hat{y}_0+3(\Delta l)\theta_0+\frac{(3\Delta l)^2}{2R_0}
\end{aligned}
\tag{H12}
$$

For $i = 4$:

$$
\begin{aligned}
\widehat{y}_4 &= \left(1+\frac{c}{R_0}\right)\frac{(\Delta l)^2}{6c}\left(2\varepsilon_3+\varepsilon_4\right)+\widehat{y}_3+(\Delta l)\theta_3+\frac{(\Delta l)^2}{2R_0} \\
&= \left(1+\frac{c}{R_0}\right)\frac{(\Delta l)^2}{6c}\left(2\varepsilon_3+\varepsilon_4\right) \\
&\quad + \underbrace{\left\{\begin{array}{l}\left(1+\frac{c}{R_0}\right)\frac{(\Delta l)^2}{6c}\left(2\varepsilon_2+\varepsilon_3\right)+\left(1+\frac{c}{R_0}\right)\frac{(\Delta l)^2}{6c}\left(2\varepsilon_1+\varepsilon_2\right)+\left(1+\frac{c}{R_0}\right)\frac{(\Delta l)^2}{6c}\left(2\varepsilon_0+\varepsilon_1\right) \\ +\left(1+\frac{c}{R_0}\right)\frac{(\Delta l)^2}{2c}\left(\varepsilon_1+\varepsilon_2\right)+2\left(1+\frac{c}{R_0}\right)\frac{(\Delta l)^2}{2c}\left(\varepsilon_0+\varepsilon_1\right)+\widehat{y}_0+3(\Delta l)\theta_0+\frac{(3\Delta l)^2}{2R_0}\end{array}\right\}}_{\widehat{y}_3} \\
&\quad + \underbrace{\left(1+\frac{c}{R_0}\right)\frac{(\Delta l)^2}{2c}\left(\varepsilon_2+\varepsilon_3\right)+\left(1+\frac{c}{R_0}\right)\frac{(\Delta l)^2}{2c}\left(\varepsilon_1+\varepsilon_2\right)+\left(1+\frac{c}{R_0}\right)\frac{(\Delta l)^2}{2c}\left(\varepsilon_0+\varepsilon_1\right)+(\Delta l)\theta_0+3\frac{(\Delta l)^2}{R_0}}_{(\Delta l)\theta_3} \\
&\quad + \frac{(\Delta l)^2}{2R_0} \\
&= \left(1+\frac{c}{R_0}\right)\frac{(\Delta l)^2}{6c}\left(2\varepsilon_3+\varepsilon_4\right)+\left(1+\frac{c}{R_0}\right)\frac{(\Delta l)^2}{6c}\left(2\varepsilon_2+\varepsilon_3\right)+\left(1+\frac{c}{R_0}\right)\frac{(\Delta l)^2}{6c}\left(2\varepsilon_1+\varepsilon_2\right) \\
&\quad +\left(1+\frac{c}{R_0}\right)\frac{(\Delta l)^2}{6c}\left(2\varepsilon_0+\varepsilon_1\right) \\
&\quad + \underbrace{1}_{4-3}\left(1+\frac{c}{R_0}\right)\frac{(\Delta l)^2}{2c}\left(\varepsilon_2+\varepsilon_3\right)+\underbrace{2}_{4-2}\left(1+\frac{c}{R_0}\right)\frac{(\Delta l)^2}{2c}\left(\varepsilon_1+\varepsilon_2\right)+\underbrace{3}_{4-1}\left(1+\frac{c}{R_0}\right)\frac{(\Delta l)^2}{2c}\left(\varepsilon_0+\varepsilon_1\right) \\
&\quad + \widehat{y}_0+4(\Delta l)\theta_0+\frac{(4\Delta l)^2}{2R_0}
\end{aligned}
\tag{H13}
$$

Based on the indicial progression patterns in equations (H10)–(H13), one can write the curved deflection $\widehat{y}_i$ in a generalized form of with two summations (with different summation limits) as equation (H14):

$$
\widehat{y}_i = \underbrace{\left(1+\frac{c}{R_0}\right)\frac{(\Delta l)^2}{6c}\sum_{j=1}^{i}\left(2\varepsilon_{j-1}+\varepsilon_j\right)}_{\text{Contributions from deflection terms}} + \underbrace{\left(1+\frac{c}{R_0}\right)\frac{(\Delta l)^2}{2c}\sum_{j=1}^{i-1}(i-j)\left(\varepsilon_{j-1}+\varepsilon_j\right)}_{\text{Contribution from slope terms}} + \underbrace{\widehat{y}_0+(i)(\Delta l)\theta_0}_{=0 \text{ for cantilever beam}} + \underbrace{\frac{(i\Delta l)^2}{2R_0}}_{\text{Due to Initial curvature}} \tag{H14}
$$

$$(i = 1,2,3,...,n)$$

Equation (H14) is the deflection equation in summation form in reference to the *x*-axis. Notice from equation (H14) that the summation of the deflection terms ends at *i*, but the summation of the slope terms ends at $i-1$, not *i*. The factor $(i-j)$ appearing in the second summation will cause the last term of summation to drop out when *j* reaches *i* $(j=i)$.

Initial Curved Displacements

In view of figure 3, the curved distant $a(s)$ traced by point A from *x*-axis to curved *s*-axis to form the undeformed curved beam can be calculated from equation (H15)

$$a(s)=\int_0^s \theta_0(s)\,ds=\int_0^s \frac{s}{R_0}\,ds=\frac{s^2}{2R_0} \tag{H15}$$

At point $s=s_i$, equation (H15) gives equation (H16):

$$a(s_i)=\frac{s_i^2}{2R_0}=\frac{(i\Delta l)^2}{2R_0} \quad ; \quad (i=1,2,3,...,n) \tag{H16}$$

Note that the initial curved displacement $(i\Delta l)^2/(2R_0)$ of the undeformed curved beam given by equation (H16) is exactly the same as the last term of equation (H14).

Similarity of Theta- and Alpha-Formulations

The last term $(i\Delta l)^2/(2R_0)$ appearing in equation (H14) is actually the initial curved displacement $a(s_i)$ of point s_i of the undeformed curved beam given by equation (H16). Therefore, if the term $(i\Delta l)^2/(2R_0)$ is moved to the left-hand side of equation (H14), one can obtain the strain-induced curved deflection in reference to the initial undeformed configuration expressed by equation (H17):

$$\underbrace{\widehat{y}_i-\frac{(i\Delta l)^2}{2R_0}}_{\substack{\text{Strain induced curved}\\ \text{deflection in relative to}\\ \text{undeformed } s\text{-axis}}} = \underbrace{\left(1+\frac{c}{R_0}\right)\frac{(\Delta l)^2}{6c}\sum_{j=1}^{i}\left(2\varepsilon_{j-1}+\varepsilon_j\right)}_{\text{Contributions from deflection terms}} + \underbrace{\left(1+\frac{c}{R_0}\right)\frac{(\Delta l)^2}{2c}\sum_{j=1}^{i-1}(i-j)\left(\varepsilon_{j-1}+\varepsilon_j\right)}_{\text{Contributions from slope terms}}$$
$$+ \underbrace{\widehat{y}_0+(i)(\Delta l)\theta_0}_{=0 \text{ for cantilever beams}} \tag{H17}$$
$$(i=1,2,3,...,n)$$

For the cantilever curved beams, the slope and deflection at the fixed end (*i* = 0) is zero [that is, $\widehat{y}_0+(i)(\Delta l)\theta_0=0$; $r_0+(i)(\Delta l)\alpha_0=0$], and therefore, the right-hand side of equation (H17) based on θ-formulation will be identical to the right-hand side of equation (15c) [or equation (B6) of Appendix B] based on α-formulation. Thus, both formulations give identical strain-induced curved deflections.

References

1. Ko, William L., W. L. Richards, and Van T. Tran, "Displacement Theories for In-Flight Deformed Shape Predictions of Aerospace Structures," NASA/TP-2007-214612, October 2007.

2. Ko, William L., and W. Lance Richards, *Method for Real-Time Structure Shape-Sensing*, U.S. Patent No. 7,520,176, issued April 21, 2009.

3. Ko, William L., and Van Tran Fleischer, "Further Development of Ko Displacement Theory for Deformed Shape Predictions of Non-Uniform Aerospace Structures," NASA/TP-2009-214643, September 2009.

4. Ko, William L., and Van Tran Fleischer, "Methods for In-Flight Wing Shape Predictions of Highly Flexible Unmanned Aerial Vehicles: Formulation of Ko Displacement Theory," NASA/TP-2010-214656, August 2010.

5. Ko, William L., and Van Tran Fleischer, "Extension of Ko Straight-Beam Displacement Theory to Deformed Shape Predictions of Slender Curved Structures," NASA/TP-2011-214567, April 2011.

6. Ko, William L., and Van Tran Fleischer, "First and Second Order Displacement Transfer Functions for Structure Shape Calculations Using Analytically Predicted Surface Strains," NASA/TP-2012-215976, March 2012.

7. Ko, William L., and Van Tran Fleischer, "Improved Displacement Transfer Functions for Structure Deformed Shape Predictions Using Discreetly Distributed Surface Strains," NASA/TP-2012-216060, November 2012.

8. Ko, William L., and Van Tran Fleischer, "Large-Deformation Displacement Transfer Functions for Shape Predictions of Highly Flexible Slender Aerospace Structures," NASA/TP-2013-216550, December, 2013.

9. Ko, William L., and Van Tran Fleischer, "Modified Displacement Transfer Functions for Deformed Shape Predictions of Slender Curved Structures with Varying Curvature," NASA/TM-2014-216660, May 2014.

10. Ko, William L., W. L. Richards, and Van Tran Fleischer, "Applications of Ko Displacement Theory to the Deformed Shape Predictions of the Doubly Tapered Ikhana Wing," NASA/TP-2009-214652, November 2009.

11. Lung, Shun-Fat, and William L. Ko, "Applications of Displacement Transfer Functions to Deformed Shape Predictions of the GIII Swept-Wing Structure," Presented at the 30th Congress of the International Council of the Aeronautical Sciences, Daejeon, Korea, September 25–30, 2016.

12. Jutte, Christine, William L. Ko, Craig Stephens, John Bakalyar, Lance Richards, and Allen Parker, "Deformed Shape Calculations of a Full-Scale Wing Using Fiber Optic Strain Data from a Ground Loads Test," NASA/TP-2011-215975, November 2011.

13. Richards, W. Lance, and William L. Ko, *Process for Using Surface Strain Measurements to Obtain Operational Loads for Complex Structures*, U.S. Patent No. 7,715,994, issued May 11, 2010.

14. Ko, William L., and Van Tran Fleischer, "Method for Estimating Operational Loads on Aerospace Structures Using Span-wisely Distributed Surface Strains," NASA TP/2013-216518, April 2013.

15. Hodgman, Charles D., *Standard Mathematical Tables*, 11th edition, Chemical Rubber Publishing Company, Cleveland Ohio, 1957.

16. Roark, Raymond J., *Formulas for Stress and Strain*, McGraw-Hill Book Company, Inc., New York, 1954.

17. Faupel, Joseph, H., *Engineering Design*, John Wiley and Sons, Inc., New York, 1964.

18. *MSC. Nastran 2005 Quick Reference Guide*, Volume 1, The MacNeal Schwendler Corporation, Newport Beach, California, 2005.